Magnetic resonance imaging and navigation of ferromagnetic thermoseeds to deliver thermal ablation therapy

Rebecca Rose Baker

A thesis in partial fulfilment of the requirements for the degree of
Doctor of Philosophy to University College London

May 2022

Centre for Advanced Biomedical Imaging
University College London

Declaration

I, Rebecca Rose Baker, confirm that the work presented in this thesis is my own. Where information has been derived from other sources, I confirm that this has been indicated in the thesis.

Abstract

Minimally invasive therapies aim to deliver effective treatment whilst reducing off-target burden, limiting side effects, and shortening patient recovery times. Remote navigation of untethered devices is one method that can be used to deliver targeted treatment to deep and otherwise inaccessible locations within the body. Minimally invasive image-guided ablation (MINIMA) is a novel thermal ablation therapy for the treatment of solid tumours, whereby an untethered ferromagnetic thermoseed is navigated through tissue to a target site within the body, using the magnetic field gradients generated by a magnetic resonance imaging (MRI) system. Once at the tumour, the thermoseed is heated remotely using an alternating magnetic field, to induce cell death in the surrounding cancer tissue. The thermoseed is then navigated through the tumour, heating at pre-defined locations until the entire volume has been ablated.

The aim of this PhD project is to develop MINIMA through a series of proof-of-concept studies and to assess the efficacy of the three key project components: imaging, navigation, and heating. First, an MR imaging sequence was implemented to track the thermoseeds during navigation and subsequently assessed for precision and accuracy. Secondly, movement of the thermoseeds through a viscous fluid was characterised, by measuring the effect of different navigation parameters. This was followed by navigation experiments performed in ex vivo tissue. To assess thermoseed heating, a series of in vitro experiments were conducted in air, water, and ex vivo liver tissue, before moving onto in vivo experiments in the rat brain and a murine subcutaneous tumour model. These final experiments allowed the extent of cell death induced by thermoseed heating to be determined, in both healthy and diseased tissue respectively.

Impact statement

The development of therapies for the treatment of cancer and other diseases is an ongoing challenge within engineering and science research. And in recent decades, the focus of researchers has shifted from traditional techniques, such as surgery, to minimally invasive and automated technologies. These novel treatment options bring promise of better outcomes for patients, by ensuring swifter recovery and minimising the chance of life-altering morbidities, as well as reducing costs for healthcare providers. MINIMA (minimally invasive image-guided ablation) is a novel thermal ablation therapy that may be used to treat cancer in a number of organs minimally invasively.

Typically a diagnostic tool, MRI scanners are essential in modern medicine for the detection of various diseases and, as a result, are readily available in clinical settings around the world. With small modifications to the existing hardware of an MRI scanner, this device may also be used for treatment purposes. The work presented in this thesis demonstrates the initial proof-of-concept for MINIMA, which is delivered using an MRI scanner. Should this therapy by translated into the clinic in the future, it could be made available through the pre-existing infrastructure of diagnostic MRI, thus making it readily accessible for many people. The developments explored in this thesis will also be valuable to researchers working in the fields of magnetic resonance navigation and magnetic hyperthermia.

Whilst completing my PhD, MINIMA has been presented through talks and exhibitions aimed at the public, as part of events such as Cheltenham Science Festival. These outreach opportunities are essential for disseminating research and engaging with the community, which help build and maintain confidence in both scientists and science in general and help inform researchers and policy makers on the most valuable and impactful areas of research.

Acknowledgements

There are many people who have provided encouragement throughout my PhD journey and without whom I almost certainly wouldn't have a thesis to submit.

First, I thank my supervisor, Mark Lythgoe. You have provided endless support throughout my time working on what some would call this rather 'wacky' project, as well as introducing me to the world of science communication and public engagement. Further thanks go to my secondary supervisor, Mark Emberton, for sharing your drive to translate novel, minimally invasive therapies into the clinic.

I would also like to extend my gratitude to all members of CABI; what a wonderful 4 years it has been as part of this large, eclectic, and joyous family! In particular, the magnetic targeting group, John, Chris, Matin and Yichao, thank you for all your help with the experiments that form this thesis. Special shout outs also go to Tammy, Daniel, and Tom; CABI would be lost without you!

The Medical Imaging CDT cohort 2017 – ~~2021~~ 2022 (#covid), you have been there every step of the way. We made it!

To all my friends who have supported me through school, my undergraduate degree and now a PhD, thank you! Especially Rosie, Ben, Naomi, and Henry, I don't know what I'd do without you guys to stroll with on a Sunday afternoon. Mum, Dad, Billy, and Harry, thank you for everything, all the opportunities you have given me and for always believing in me. Most of all, thank you Jack, my best friend and partner for life, words cannot express my gratitude towards you.

Publications

Baker, R. R., Payne, C., Yu, Y., Mohseni, M., Connell, J. J., Lin, F., Harrison, I. F., Southern, P., Rudrapatna, U. S., Stuckey, D. J., Kalber, T. L., Siow, B., Thorne, L., Punwani, S., Jones, D. K., Emberton, M., Pankhurst, Q. A. and Lythgoe, M. F. (2022) 'Image-guided Magnetic Thermoseed Navigation and Tumor Ablation Using an MRI System', *Advanced Science,* 9, pp. 2105333.

Yu, Y., Payne, C., Marina, N., Korsak, A., Southern, P., Garcia-Prieto, A., Christie, I. N., **Baker, R. R.**, Fisher, E. M. C., Wells, J. A., Kalber, T. L., Pankhurst, Q. A., Gourine, A. V. and Lythgoe, M. F. (2021) 'Remote and Selective Control of Astrocytes by Magnetomechanical Stimulation', *Advanced Science,* 9, pp. 2104194.

Mohseni, M., Connell, J. J., Payne, C., Patrick, P. S., **Baker, R.**, Yu, Y., Siow, B., Zaw-Thin, M., Kalber, T. L., Pankhurst, Q. A. and Lythgoe, M. F. (2020) 'Scalable magnet geometries enhance tumour targeting of magnetic nano-carriers', *Materials & Design,* 191, pp. 108610.

Conference proceedings and awards

October 2021	A novel thermoablative device to heat ferromagnetic thermoseeds as a minimally invasive cancer therapy **R. R. Baker**, Y, Yu, T. L. Kalber, C. Payne, D. J. Stuckey, P. Southern, Q. A. Pankhurst, M. Emberton, M. F. Lythgoe. UCL Institute of Healthcare Engineering Early-career researchers symposium, London, UK. Oral presentation. **Award: Best oral presentation**
October 2021	A novel thermoablative device to heat ferromagnetic thermoseeds as a minimally invasive cancer therapy **R. R. Baker**, Y, Yu, T. L. Kalber, C. Payne, D. J. Stuckey, P. Southern, Q. A. Pankhurst, M. Emberton, M. F. Lythgoe. International Congress of Hyperthermic Oncology, virtual meeting. Oral presentation.
September 2021	A novel thermoablative device to heat ferromagnetic thermoseeds as a minimally invasive cancer therapy **R. R. Baker**, Y, Yu, T. L. Kalber, C. Payne, D. J. Stuckey, P. Southern, Q. A. Pankhurst, M. Emberton, M. F. Lythgoe. BioMedEng21, Sheffield, UK. Oral presentation.
October 2019	Targeting magnetic seeds using an MRI system – a minimally invasive therapy for prostate cancer **R. R. Baker**, M. J. Mohseni, C. Payne, J. J. Connell, B. Siow, Q. A. Pankhurst, M. Emberton, M. F. Lythgoe. CRUK-AACR Conference on Engineering and Physical Sciences in Oncology, London, UK. Poster presentation.
February 2019	Imaging and targeting magnetic seeds using an MRI system **R. R. Baker**, M. Mohseni, C. Payne, J. J. Connell, B. Siow, Q. A. Pankhurst, M. Emberton, M. F. Lythgoe. UKMagSoc MRI and Magnetic Particles for MRI Diagnostics, Oxford, UK. Poster presentation.

Table of contents

List of figures

List of tables

Abbreviations and acronyms

2D	two dimensional
3D	three dimensional
acqBW	acquisition bandwidth
ADC	analogue to digital conversion
AMF	alternating magnetic field
ANOVA	analysis of variance
ATP	adenosine triphosphate
BLI	bioluminescence imaging
CABI	Centre for Advanced Biomedical Imaging
CCD	charge-coupled device
CT	computed tomography
DFN	dipole field navigation
DMEM	Dulbecco's modified eagle medium
excBW	excitation bandwidth
excOffset	excitation frequency offset
FCS	foetal calf serum
FFN	fringe field navigation
FID	free induction decay
FLASH	fast low-angle shot
FOV	field of view
FSE	fast spin echo
HIFU	high-intensity focused ultrasound
H&E	Haematoxylin and eosin
LHS	left-hand side
LITT	laser interstitial thermal therapy
MACH	magnetic alternating current hyperthermia
MAVRIC	multi-acquisition variable-resonance image combination
MINIMA	minimally invasive image-guided ablation
MNP	magnetic nanoparticle
MR	magnetic resonance
MRI	magnetic resonance imaging
MRN	magnetic resonance navigation

MRT	magnetic resonance targeting
MS-SET	magnetic-signature selective excitation
MSI	multi-spectral imaging
NMR	nuclear magnetic resonance
PBS	phosphate buffered saline
PE	phase encoding
PET	positron emission tomography
RARE	rapid acquisition with relaxation enhancement
RF	radiofrequency
RHS	right-hand side
RO	readout
ROI	region of interest
SD	standard deviation
SEMAC	slice encoding for metal artefact correction
SPION	superparamagnetic iron oxide nanoparticle
TD	thermal dose
TE	echo time
TR	repetition time
TTC	2,3,5-triphenyltetrazolium chloride
UCL	University College London
VAT	view-angle tilting
VTF	Video Tumour Fighter

1 Introduction

1.1 The MINIMA concept

Minimally invasive therapies aim to improve current healthcare practice by reducing the risk of complications, mitigating off-target effects, shortening patient recovery times and, consequently, minimising associated financial burden. Some recent examples include the Gamma-knife, for localised radiation therapy in the brain, and high-intensity focused ultrasound (HIFU), a non-invasive method of thermal ablation. However, these novel approaches tend to be specific to an organ or disease and, therefore, have had little opportunity to be applied more widely across conditions.

Increasingly, the navigation of untethered devices through the body has been investigated, allowing minimally invasive therapies to reach deeper targets for both treatment and diagnostic purposes. An established example is the PillCam, a camera contained within a swallowable capsule that is used to study the gastrointestinal tract (Iddan *et al.*, 2000). The PillCam is passively propelled through the body by peristalsis, alleviating the discomfort patients experience with traditional endoscopic procedures. Active methods of navigation have also been developed, including chemical, magnetic and ultrasound mediated propulsion (Soto *et al.*, 2020). Medical imaging is often employed to track and guide these devices, thus forming an essential component of minimally invasive focal therapies (Pane *et al.*, 2019).

One project developed in the late 1980s called ‘Video Tumour Fighter’ (VTF), used a rotatable electromagnet to navigate ferromagnetic cylindrical thermoseeds through the brain of a dog, before heating them to induce cell death (Grady *et al.*, 1990). While in vivo navigation and heating of the thermoseed was successful, VTF was not taken any further than preclinical experiments. A potential reason for this is the inferior imaging technology that was available at the time. Pre-acquired magnetic resonance (MR) images were registered with fluoroscopic images based on the position of fiducial markers attached to the skull; not only is this invasive, but the registration would likely have lacked the accuracy required to safely perform the procedure in the brain. Alternatively, this

work led to the formation of the company Stereotaxis, which develops external electromagnets to guide magnetically tipped catheters to treat atrial fibrillation (Lim *et al.*, 2017; Carpi and Pappone, 2009).

A magnetic resonance imaging (MRI) scanner, a diagnostic tool readily available in most hospitals, may provide the ideal platform on which to deliver a minimally invasive thermal ablation therapy. Alongside the inherent advantage of image-guidance, the magnetic field gradients generated by the MRI scanner can be used to exert a force on a ferromagnetic device, navigating it towards the diseased tissue of interest. This concept forms the basis of MINIMA (minimally invasive image-guided ablation). MR images will help determine the least invasive path, along which a ferromagnetic thermoseed will be navigated. Additionally, imaging may be used to constantly track the position of the thermoseed, giving real-time assurance of the thermoseed's location. Once at the target, an alternating magnetic field (AMF) may be applied, causing the thermoseed to heat and induce localised cell death. The thermoseed may then be navigated through the target tissue, heating at multiple locations until the whole volume has been ablated. Having navigated the thermoseed for removal, MRI could then be used to inform on the success of the procedure.

In the remainder of this chapter, I introduce the three essential components of MINIMA: navigation, imaging, and heating. Following this, chapters 2 and 3 provide an explanation of the physical phenomena that underpin the project, and finally, in chapters 4 – 7 I present a series of proof-of-concept studies that evaluate the potential of MINIMA as a minimally invasive cancer therapy.

1.2 Magnetic resonance actuation

1.2.1 Magnetic resonance navigation

Magnetic resonance navigation (MRN) has developed over the last 20 years as a technique to deliver targeted therapies, using the technology readily available in MRI scanners. By incorporating a ferromagnetic component into a miniaturised medical device, the imaging magnetic field gradients that are generated by an MRI scanner will exert a force on the device, causing it to move along the gradient axis. Furthermore, the imaging coils can generate gradients along three orthogonal axes, providing freedom to steer the device in any direction. MRN may

be used to target therapies to precise locations within the body and simultaneously increase therapeutic effect and reduce toxicity, by increasing and reducing delivery to targeted and healthy tissues respectively.

The ability to exert sufficient force to actuate a ferromagnetic sphere with an MRI scanner was first demonstrated by Sylvain Martel's group. With the intention of using MRN to navigate microdevices through the vasculature, experiments propelling 2 – 3 mm diameter steel spheres through tubular flow phantoms, mimicking the conditions of peripheral arteries, were conducted (Mathieu *et al.*, 2005; Mathieu, Beaudoin and Martel, 2006). By applying 18 mT m^{-1} magnetic field gradients in the opposite direction to water flow, spheres were successfully actuated, allowing their position within the tube to be maintained at equilibrium. These studies were shortly followed by the first in vivo MRN proof-of-concept (Martel *et al.*, 2007). Using a balloon catheter to stop blood flow and magnetic field gradients of no more than 40 mT m^{-1}, a 1.5 mm diameter steel sphere was successfully navigated through the carotid artery of a living swine, at speeds of 8 – 11 cm s^{-1}. These initial experiments provided confidence in MRN as a technique and demonstrated the possibility of elevating an MRI scanner from a diagnostic tool to a therapeutic platform.

However, for MRN to be clinically translatable, devices must be navigated much deeper into the vascular network, guided not just through arteries but also capillaries, thus imposing a limit on the size of the device. Since the magnitude of the magnetic actuation force decreases with the volume of the ferromagnetic object, navigation through capillaries requires gradient strengths at least an order of magnitude larger than those available within typical clinical MRI scanners (40 – 80 mT m^{-1}). Consequently, a specialist steering gradient coil was manufactured, which could be inserted into the bore of a clinical MRI scanner and deliver gradient strengths of up to 400 mT m^{-1} (Mathieu and Martel, 2007). Using this coil, microcarriers loaded with iron-cobalt nanoparticles and a chemotherapy drug (Pouponneau, Leroux and Martel, 2009) were directly injected into the hepatic artery of a rabbit and subsequently navigated to the left or right liver lobe for targeted chemoembolisation (Pouponneau *et al.*, 2011). The delivered drug dose increased by 15 – 40 % in the targeted lobe and decreased by 20 – 30 % in the

untargeted lobe, when compared with no steering, thus demonstrating the potential of MRN-mediated drug delivery to minimise off-target effects.

1.2.2 Magnetic resonance targeting

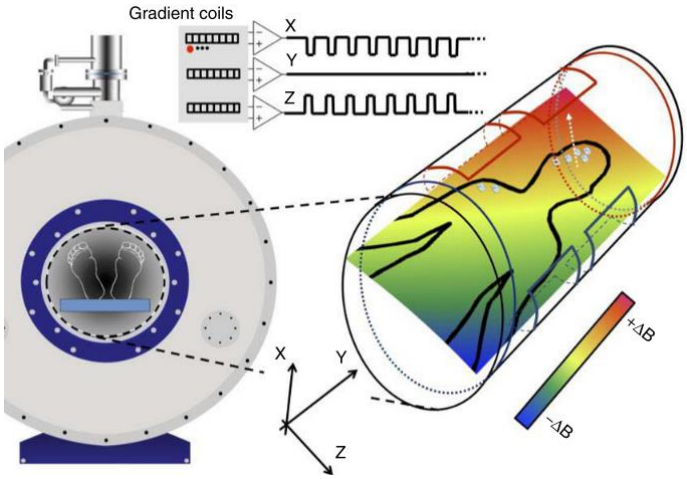

Figure 1.1 Magnetic resonance targeting. The patient is positioned within the centre of an MRI scanner, where linear magnetic field gradients can be used to induce a force on ferromagnetic particles and devices. Superparamagnetic iron oxide nanoparticle-labelled cells or drugs are injected systemically and circulate through the patient's vascular network. By consistently applying a magnetic field gradient in the direction of the physiological target, in this case the right hemisphere of the brain, the cells/drug will preferentially accumulate in the diseased tissue/organ, thus increasing therapeutic effect and minimising unwanted side effects. Schematic reproduced from Muthana *et al.* (2015).

Ferromagnetic agents of a much smaller size, such as superparamagnetic iron oxide nanoparticles (SPIONs), can also be used to deliver therapeutic agents within the body. Termed magnetic resonance targeting (MRT), this technique differs from MRN, as the SPIONs are administered systemically and, rather than being navigated along a determined path, a magnetic field gradient is consistently applied in the direction of the physiological target (Figure 1.1), thus leading to increased SPION accumulation in the diseased tissue. This has been demonstrated in a simple bifurcation model with SPION-labelled stem cells and a gradient strength of 500 mT m^{-1} (Riegler *et al.*, 2010), as well as in vivo (Muthana et al., 2015). Using MRT, Muthana et al. observed a reduction in primary tumour growth in a murine prostate cancer model following MRT-mediated delivery of macrophages loaded with oncolytic viruses, when compared with control groups. Although these studies demonstrate that MRT can increase doses delivered to diseased organs, the systemic delivery still carries a risk of exposing healthy tissues to potentially toxic agents.

1.2.3 Thermoseed tracking with MRI

A key advantage of MRN is the imaging modality, user interface and system control provided by the MRI scanner, enabling the navigation of untethered devices to be performed autonomously. Early examples of ferromagnetic device navigation and tracking without the need for human interaction integrated a real-time feedback loop into the software platform used to control a typical MRI scanner. Waypoints identified at three distinct locations on a pre-acquired angiography formed the intended path of a 1.5 mm steel sphere through the artery of a swine (Figure 1.2) (Chanu and Martel, 2007). The control sequence would identify the current position of the sphere from an MR-based tracking sequence, determine the direction and distance to travel to the next way point, and calculate and apply the appropriate gradient amplitude, direction, and timing. Once the sphere reached a defined circle of precision around the waypoint (10 mm diameter), the software would move onto the next waypoint on the planned trajectory. The control sequence was rapid and could be implemented at a frequency of 24 Hz.

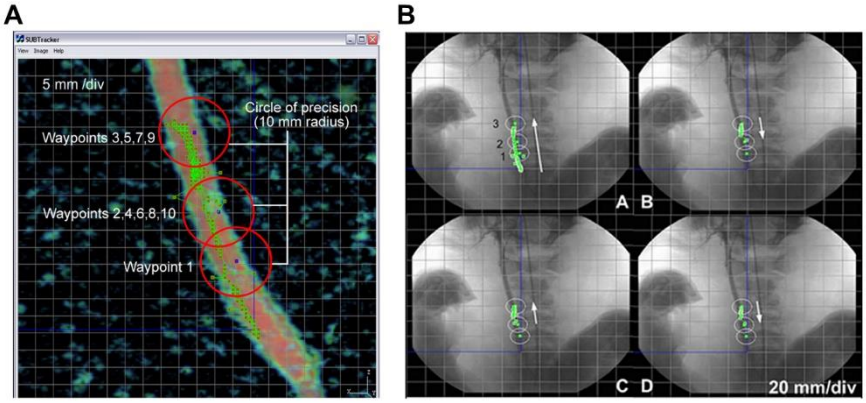

Figure 1.2 Automated tracking of a chrome steel sphere. The intended path of the sphere was defined using three waypoints and passed from waypoint 1 to 3, before moving backwards and forwards between waypoints 2 and 3. The sphere was considered to have reached the waypoint once within a surrounding circle of precision (10 mm radius). **A** The software in which the path is defined and sphere movement is tracked (Chanu and Martel, 2007). **B** Sphere trajectory superimposed over an x-ray angiography. The green dots show actual displacement of the sphere. Arrows indicate the direction of movement. (Martel *et al.*, 2007)

Although the flow within the swine's artery was controlled using a balloon catheter, later in vitro studies demonstrated the ability to use this automated navigation platform under quiescent (Chanu *et al.*, 2008) and pulsatile flow

(Tamaz *et al.*, 2008). More recent advances have focused on optimum path planning for more complex pathways. A 750 µm steel sphere was navigated through a 2D maze, along trajectories optimised for different intentions, such as the thermoseed sticking to the centreline of the vessels or improving gradient coil power efficiency (Folio and Ferreira, 2017). Taken together, these examples demonstrate the advantages that pre-existing MRI hardware and software provide in the development of fully automated MRN procedures.

1.2.4 Dipole field navigation

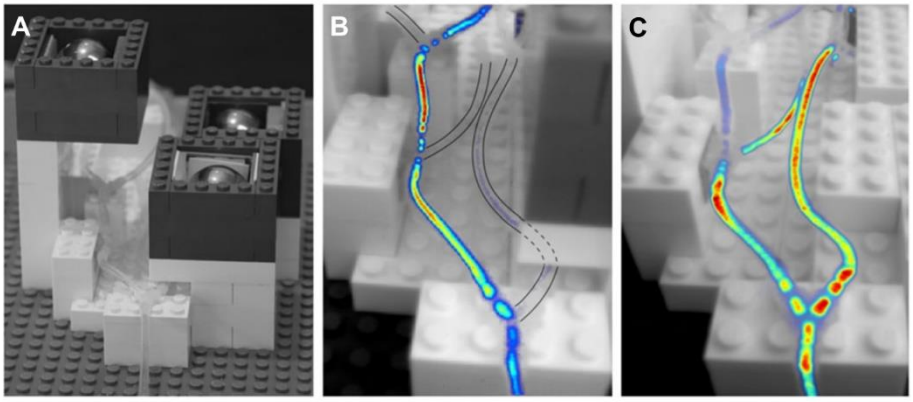

Figure 1.3 Dipole field navigation (DFN). A In vitro experimental setup for DFN proof-of-concept consisted of three ferromagnetic cores positioned around a three-bifurcation, vessel-mimicking network, through which ferromagnetic nanoparticles were injected under a continuous flow. The paths followed by the ferromagnetic nanoparticles were monitored with a camera, and the nanoparticle motion density was presented as a heatmap. **B** With the ferromagnetic cores in position, most of the detected motion was along the intended path, with few nanoparticles travelling down the wrong branches. **C** The control experiment, performed without the ferromagnetic cores, emphasises the effect the cores have on the paths followed by the ferromagnetic nanoparticles. Figure adapted from Latulippe and Martel (2015).

Meanwhile, alternative MR actuation techniques, such as dipole field navigation (DFN) and fringe field navigation (FFN), have been developed to overcome some of the limitations of MRN. DFN involves the positioning of ferromagnetic cores around the patient, within the bore of the MRI scanner. These cores distort the homogenous magnetic field and, with carefully planned positioning, can create a magnetic path that guides the ferromagnetically-labelled therapeutic agents to the intended target (Figure 1.3) (Latulippe and Martel, 2015). Although this technique can generate gradients of up to 400 mT m^{-1} (Latulippe and Martel, 2018), modelling the path taken by the therapeutic agent can be challenging,

especially when accounting for variation in anatomy between patients. In addition, the magnetic field distortions created by the ferromagnetic cores inhibits any real-time MRI-based tracking, thus necessitating complex mechanisms to insert and remove the ferromagnetic cores throughout the procedure (Shi *et al.*, 2021).

1.2.5 Fringe field navigation

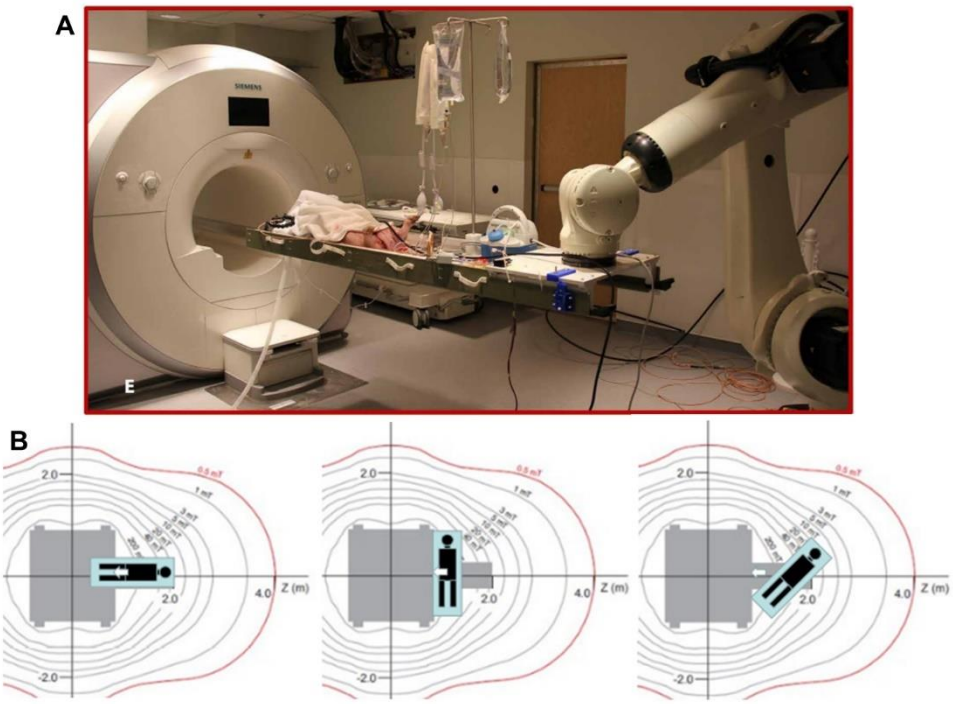

Figure 1.4 Fringe field navigation (FFN). FFN utilises the magnetic field external to the MRI scanner to navigate magnetic guidewires through narrow vessels for catheterisation. With the patient table attached to a robotic arm (**A**), the patient can be rotated and moved through the fringe field, allowing the direction of the magnetic field gradient to be aligned with the required axis of actuation (**B**). Figure adapted from Tremblay *et al.* (2014) and Azizi *et al.* (2019).

Alternatively, FFN takes advantage of the large magnetic field gradients surrounding the MRI scanner, known as the fringe field, that can be as large as 4 T m^{-1} (Tremblay *et al.*, 2014). The patient table is attached to a robotic arm, and the patient is rotated and moved through the field, allowing the magnetic field gradient to be aligned with the intended direction of navigation (Figure 1.4). These gradient strengths are ten-fold larger than what can be achieved with MRN and DFN and, therefore, could be used to navigate smaller therapeutic agents through narrower vessels, much deeper in the vascular network. Martel's group recently demonstrated this concept for the first time in vivo in a swine model, by navigating

a magnetically-tipped guidewire through vessels 2 mm in diameter (Azizi *et al.*, 2019). Although this technique shows some potential, a limitation is again the inability to track the navigable agent with MRI-based imaging. Real-time imaging is instead performed using x-rays, which are registered with pre-acquired MR-angiography images.

1.2.6 MRN through tissue

Although the work discussed so far has focused on the navigation of devices and particles through vasculature, navigating a device directly through tissue could expand the range of MRN applications, to include minimally invasive surgery and biopsies for example. However, the ability to penetrate tissue requires much larger actuation forces. Studies conducted as part of the VTF project determined that a force of 0.07 N was required to move a 3 mm diameter sphere through brain tissue at approximately 0.7 mm s^{-1} (Molloy *et al.*, 1990). To exert 0.07 N on a 3 mm ferromagnetic sphere using an MRI scanner would require a magnetic field gradient strength of 3.6 T m^{-1}. Since clinical MRI scanners can typically generate 40 – 80 mT m^{-1} magnetic field gradients, modifications, to either the MRI system or the penetrating device, would need to be made to perform MRN through tissue. This has led to the development of elaborate technologies such as the MRI-Gauss gun (Becker, Felfoul and Dupont, 2015) and magnetic hammer actuation (Leclerc *et al.*, 2018). The MRI-Gauss gun consists of three stages containing two magnetised spheres and a non-magnetic spacer (Figure 1.5A, B). The first stage is actuated using the magnetic field gradients of an MRI scanner until it collides with the second stage, starting a chain reaction of collisions that amplifies the velocities of the magnetised spheres until the final device is actuated with enough force to penetrate tissue. Although the MRI-Gauss gun was shown to actuate a 0.46 mm diameter needle ~15 mm into a brain tissue-mimicking phantom, it has several disadvantages, the main one being the size of the device. Each stage of the device is ~35 mm in length, and almost 10 mm in diameter, meaning it can only be used to penetrate tissue from outside the body.

Magnetic hammer actuation instead uses a single-component millirobot consisting of a magnetised sphere in a tube. A spring and an impact plate are placed at the tail and front end of the tube respectively, and a pointed tip is added to the front of the device to aid penetration (Figure 1.5C). Using the magnetic field

gradients generated by the MRI scanner, the sphere is projected towards the spring. Once the gradients are switched off, the sphere is released and propelled to the front of the device, generating a large force as it comes into contact with the plate. This process is then repeated to create a pulsed force. A 7.5 mm diameter, 50 mm long millirobot, containing a 5 mm steel ball, penetrated ex vivo brain tissue up to 9 mm using a magnetic field gradient of 23 mT m^{-1} (Figure 1.5E). Although this method is effective at penetrating tissue with small magnetic field gradients that are readily achievable on a clinical MRI scanner, once again the device is very large, thus inhibiting its use in vivo (Figure 1.5D).

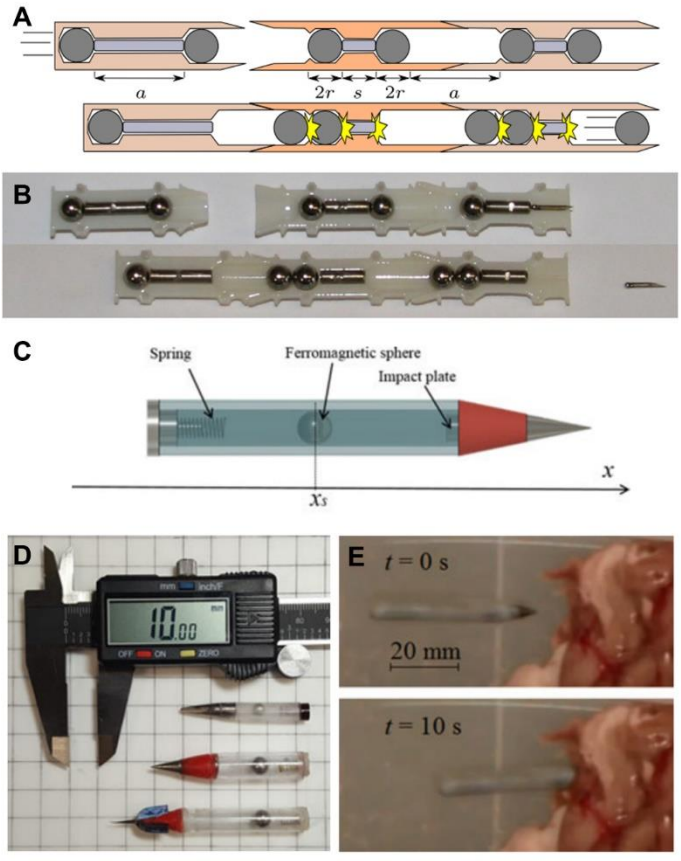

Figure 1.5 MRN-based tissue penetration technologies. A, B Schematic and cross-sectional photograph of the MRI-Gauss gun before and after triggering (Becker, Felfoul and Dupont, 2015). **C** Schematic of a millirobot designed for tissue penetration, actuated by a magnetic hammer. **D** Photographs of magnetic hammer millirobot designs. **E** Photographs showing the magnetic hammer millirobot driven by an MRI scanner to penetrate ex vivo brain tissue. C, D and E are adapted from Leclerc *et al.* (2018).

A key element of all MRN-based techniques and studies discussed in this chapter is the magnitude of the magnetic field gradients generated by the MRI scanner. With current clinical MRI gradient coils limited to just 10's of mT m^{-1}, this is one

of the greatest challenges in the field. Unlike clinical systems, high-field preclinical MRI scanners can typically deliver gradient strengths up to 1 T m^{-1}. Using a preclinical MRI scanner may therefore be advantageous in the development of MINIMA. Chapters 4 and 5 discuss this point further and include MRN experiments that investigate the navigation component of the MINIMA project.

1.3 Imaging magnetic devices

Medical imaging forms an essential part of minimally invasive therapies, as it is the only means by which the inside of the body can be visualised without open surgery. Image-guided therapies not only use imaging to diagnose and visualise the diseased tissue, but also to guide interventional tools and devices. A range of different imaging modalities are used in the clinic for diagnostic purposes and have been incorporated into image-guided interventions, including MRI, ultrasound, computed tomography (CT) and positron emission tomography (PET) (Kalinyak *et al.*, 2011). MRI has a distinct advantage when imaging magnetic devices, as it is particularly sensitive to the magnetic properties of metals. In addition, MRI provides excellent soft tissue contrast, high spatial resolution and does not use ionising radiation, thus allowing repeated scanning. These advantages make MRI an ideal method of imaging for MRN and the MINIMA project.

The sensitivity of MRI to the magnetic properties of metals has resulted in the use of magnetic nanoparticles (MNPs) as an image contrast agent for over 25 years (Estelrich, Sanchez-Martin and Busquets, 2015). MNPs appear as large hypointense regions, which makes them easy to track, and have been used for a range of applications including identification of liver (Semelka and Helmberger, 2001) and brain tumours (Enochs *et al.*, 1999), and molecular and cellular tracking (Bulte and Kraitchman, 2004). In fact, the hypointensities are so large, it is even possible to track a single cell (Korchinski *et al.*, 2015; Lee *et al.*, 2011).

Although advantageous when working with magnetic particles on the nano or micro scale, the presence of larger metal objects can cause significant problems in MRI. In the worst case, it is not safe for patients with certain orthopaedic implants or pacemakers to be exposed to the magnetic field of an MRI system, thus inhibiting them from having a scan. In more modest scenarios, for example

when patients have implants made from a paramagnetic material such as titanium, the patient's safety is not compromised, but large artefacts appear in the images, thus masking or distorting the anatomy. To overcome these challenges, specialised MRI pulse sequences have been developed for imaging near metals (Cho, Kim and Kim, 1988; Hargreaves *et al.*, 2018) and tracking ferromagnetic devices (Felfoul *et al.*, 2008). These methods may be useful in the development of MINIMA and will be discussed in more detail in chapter 3, following a brief introduction to MRI theory.

1.4 Thermal ablation therapies

Thermal ablation therapies increase temperatures in vivo to induce irreversible cell death and tissue damage. A modest temperature increase (41 – 45 °C) is termed hyperthermia, and within this range proteins become denatured, apoptotic cell death is induced and after prolonged periods (30 – 60 minutes) irreversible tissue damage can occur (Hilger, 2013). Heating to temperatures above 45 °C is referred to as thermal ablation and causes direct damage at the tissue and subcellular level, leading to coagulative necrosis (Chu and Dupuy, 2014). A range of different techniques have been developed to deliver focal thermal ablation and have been employed in the treatment of many diseases including epilepsy (Tovar-Spinoza *et al.*, 2013) and Parkinson's (Martinez-Fernandez *et al.*, 2018). Due to the increased thermo-sensitivity of cancer cells (Nikfarjam, Muralidharan and Christophi, 2005), hyperthermia and ablation can be particularly effective cancer treatments, with hyperthermia typically used as an adjuvant therapy and thermal ablation as a minimally invasive alternative to surgery.

Various methods have been developed for thermal ablation therapy, with each technique differing in its process of heat generation and delivery. Typically, these techniques treat focal regions, and are much less invasive than traditional surgical techniques, thus limiting side effects and reducing recovery times. Some of the more established thermal ablation methods include radiofrequency (RF) ablation, laser interstitial thermal therapy (LITT) and HIFU.

RF ablation involves the flow of an RF current through an electrode that has been inserted into the target tissue, with dispersion pads placed elsewhere on the patient to close the circuit (Hong and Georgiades, 2010). The electrode has a

small cross-sectional area, thus creating a high energy flux around it, while the large area of the pads disperses the energy. As a result, heat is generated at the electrode tip. RF ablation is most commonly used to treat liver tumours (McGahan and Dodd, 2001) and epilepsy (Quigg and Harden, 2014) and is often cheaper than other thermal ablation therapies. The main limitations of this technique is the inability to treat tumours > 3 cm with a single electrode, thus necessitating specialised electrode designs (Meijerink *et al.*, 2011) or the insertion of multiple electrodes, and the requirement for tissues to have high electrical conductivity.

LITT ablates tissue using laser light delivered via optical fibres that have been stereotactically inserted into the tissue of interest. The photon energy from the laser is converted to molecular motion when it encounters the tissue, which generates heat. Typically, this is performed within an MRI scanner, and imaging is interleaved with firing of laser pulses to monitor the boundary between the viable and non-viable tissue in real time (Patel and Kim, 2020). Diseases commonly treated with LITT include epilepsy and brain tumours. Like RF ablation, the therapy is delivered from a single source within the tissue, thus limiting the region of necrosis to 2 cm (Prince *et al.*, 2017). In addition, abnormally shaped lesions would require multiple fibres to be inserted at different locations to ensure full coverage.

HIFU consists of a piezoelectric transducer that delivers ultrasound waves to the target tissue, like those used for ultrasound imaging. The main difference is that the ultrasound waves are concentrated at a focal point, transferring energy to the tissue, which causes a rapid increase in temperature to above 70 °C. The size of the focal lesion can be varied, but is typically cylindrical in shape with a diameter and length of approximately 3 and 11 mm respectively (Illing and Emberton, 2006). The focal lesion is then rastered through the tumour to ensure complete coverage. The main advantages of HIFU are that it is completely non-invasive, and it does not use ionising radiation. Disadvantages include the need for the patient to remain very still, thus necessitating a general anaesthetic. HIFU has been used to treat cancer in a range of organs including prostate (van der Poel *et al.*, 2018), liver, pancreas (Diana *et al.*, 2016) and the brain (Alkins and Mainprize, 2018).

Magnetically mediated hyperthermia and ablation involves the application of an AMF to heat magnetic nanoparticles or thermoseeds, leading to a rise in temperature which subsequently induces localised cell death. This is the method of heating that will be used for MINIMA. The physical principles behind this heating process are presented in the next chapter, and its application within the literature is discussed further in chapters 6 and 7.

2 Magnetically mediated actuation and heating

The basic introduction to magnetism provided in this chapter has been summarised from the following texts: Coey (2009) and Griffiths (2017).

2.1 Magnetism

Magnetism is a natural phenomenon that arises from the movement of electric charges or the intrinsic magnetic moment of electrons or atoms and results in attractive and repulsive forces between objects. All materials interact with magnetic fields to varying degrees, depending on their atomic properties. This interaction (i.e., the extent to which a material is magnetised by an external magnetic field) can be described by magnetic susceptibility, a dimensionless parameter, which is defined in SI units as:

$$X = \frac{M}{H} \tag{2.1}$$

where M is the internal magnetisation of the material and H is the external magnetic field, both expressed in units of A m^{-1}. The magnetic behaviour of materials can be classified into 5 distinct types: diamagnetism, paramagnetism, ferromagnetism, anti-ferromagnetism, and ferrimagnetism.

Diamagnetism originates from the change in orbital motion of electrons in the presence of a magnetic field. This behaviour occurs in all materials and results in a weak magnetisation, antiparallel to the applied field. Diamagnetic materials, such as water, have a small, negative susceptibility (-10^{-3} to -10^{-6}) and do not exhibit any other form of magnetic behaviour.

Paramagnetism arises primarily from the spin of unpaired electrons. In the absence of a magnetic field, magnetic moments of paramagnetic atoms are randomly orientated, due to thermal motion, resulting in no net magnetisation. When a field is applied, the magnetic moments tend to align with the field. Paramagnetic materials do not retain their magnetisation, meaning the net magnetisation returns to zero once the applied field is removed.

Ferromagnetism is observed in metals such as iron, nickel, and cobalt; it is caused by the alignment of atomic magnetic moments (from unpaired electron spins) with one another over large regions called domains. Neighbouring domains are orientated randomly, resulting in no net magnetisation. When an external field is applied, domain boundaries shift, increasing the volume of regions in alignment with the field. Unlike paramagnetic materials, the interaction of magnetic moments within ferromagnetic materials results in residual magnetisation when the field is removed. The maximum magnetisation that can be achieved is called the saturation magnetisation. This process of magnetisation is irreversible due to the pinning of domain walls, a property referred to as hysteresis (Figure 2.1).

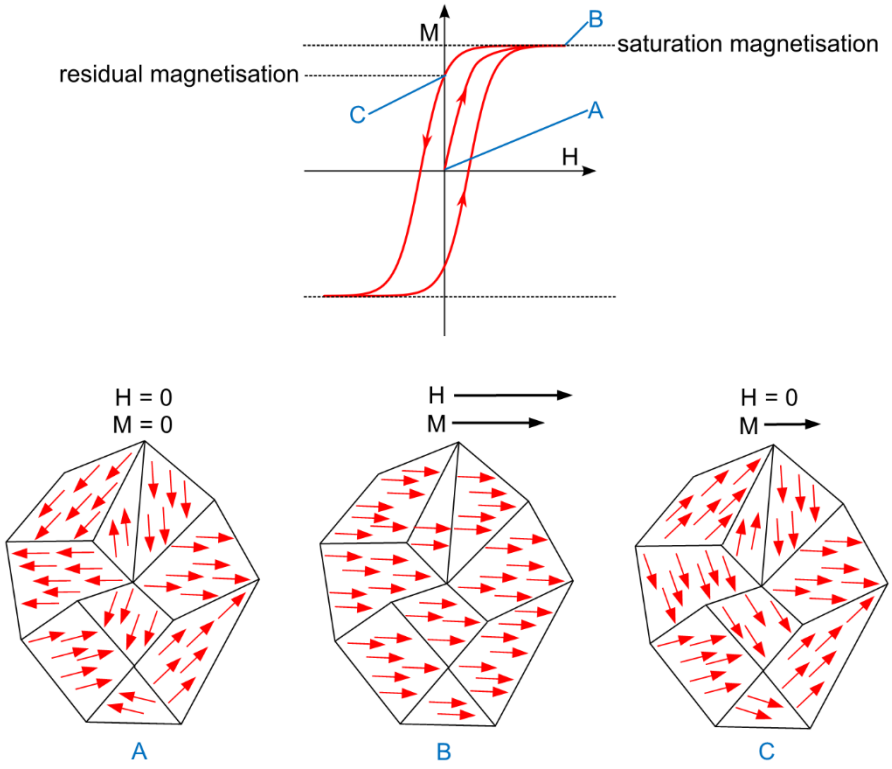

Figure 2.1 Magnetisation of ferromagnetic materials. In the absence of an external magnetic field (H), magnetic moments align with one another to form domains that are orientated at random, resulting in no net magnetisation (M). When an external field is applied, magnetic domains begin to align with one another in the same direction as H. When the magnetic field is removed, domains tend to remain aligned, resulting in some residual magnetisation. This process can be described by a hysteresis curve (top).

Anti-ferromagnetism is similar to ferromagnetism in the formation of magnetic domains; however, within each domain the magnetic moments are aligned anti-

parallel, leading to no net magnetisation. This is also true for ferrimagnetism, but with opposing magnetic moments of varying amplitude. Ferro-, anti-ferro- and ferrimagnetic materials become paramagnetic above a certain temperature, called the Curie, Néel and ferrimagnetic Curie temperature respectively, due to increased thermal motion.

2.2 Magnetic actuation

When a magnetic particle is placed within a magnetic field it will behave as a point-like magnetic dipole. The magnetic field will exert a torque ($\boldsymbol{\tau}$) on the particle, causing it to rotate and align its magnetic dipole moment ($\boldsymbol{m}$) with the magnetic field vector ($\boldsymbol{B}$):

$$\boldsymbol{\tau} = \boldsymbol{m} \times \boldsymbol{B} \tag{2.2}$$

$$\boldsymbol{m} = V_m \boldsymbol{M} \tag{2.3}$$

where V_m is the volume of the particle and $\boldsymbol{M}$ is the magnetisation of the particle.

To exert a translational force ($\boldsymbol{F_m}$) on the particle, a magnetic field gradient is required:

$$\boldsymbol{F_m} = (\boldsymbol{m} \cdot \nabla)\boldsymbol{B} \tag{2.4}$$

This can be written as (Pankhurst *et al.*, 2003):

$$\boldsymbol{F_m} = \frac{V_m \Delta\chi}{\mu_0}(\boldsymbol{B} \cdot \nabla)\boldsymbol{B} \tag{2.5}$$

where $\Delta\chi$ is the difference in magnetic susceptibility between the particle and its surroundings and μ_0 is the permeability of free space. Equation 2.5 shows the dependence of the force on both the magnitude and gradient of the magnetic field, as well as the magnetic susceptibility and volume of the material. If the particle is ferromagnetic and has reached saturation magnetisation ($\boldsymbol{M_s}$), equation 2.5 is simplified to give (Riegler *et al.*, 2011):

$$\boldsymbol{F_m} = V_m(\boldsymbol{M_s} \cdot \nabla)\boldsymbol{B} \tag{2.6}$$

Due to the high magnetic field generated by an MRI scanner, any ferromagnetic thermoseeds positioned within the bore will be fully magnetised, and the translational force will be dependent on the size of the particle, the saturation magnetisation, and the magnetic field gradient.

MRN uses the imaging coils of an MRI scanner to generate magnetic field gradients and exert a translational force on a ferromagnetic object. In the case of MINIMA, when the ferromagnetic thermoseed is placed within the MRI scanner its magnetisation will be aligned with the main magnetic field, traditionally defined as the z axis. Neglecting the x and y magnetisation components, equation 2.6 can be simplified to give:

$$\begin{bmatrix} F_{m,x} \\ F_{m,y} \\ F_{m,z} \end{bmatrix} = V_m M_z \begin{bmatrix} \frac{\partial B_z}{\partial x} \\ \frac{\partial B_z}{\partial y} \\ \frac{\partial B_z}{\partial z} \end{bmatrix} \tag{2.7}$$

Furthermore, if the gradient is applied along a single axis e.g., z:

$$F_{m,z} = V_m M_z \frac{\partial B_z}{\partial z} \tag{2.8}$$

In the literature, equation 2.8 is often quoted with an additional term, D, which stands for the duty cycle of the magnetic field gradient:

$$F_{m,z} = V_m D M_z \frac{\partial B_z}{\partial z} \tag{2.9}$$

The duty cycle describes the ratio of time for which the gradients can be applied within a set period without the hardware overheating and is often a limiting factor in MRN studies. Therefore, the effect of each of the parameters in equation 2.9 on the movement of a thermoseed is assessed in chapter 5, before attempting to navigate through tissue.

2.3 Magnetically mediated hyperthermia and ablation

Magnetically mediated hyperthermia and ablation uses an AMF to selectively heat magnetic particles or thermoseeds, inducing a rise in local temperature. Larger particles, such as the thermoseeds used in this thesis, are predominantly heated by two mechanisms when exposed to an AMF. The first is via the induction of eddy currents through the volume of ferromagnetic material, which dissipates energy via resistive heating. The density of these currents is non-uniform, with the majority carried on the surface. The depth at which current density is reduced to $1/e = 37\ \%$ of the surface value is called the skin depth:

$$\delta = \sqrt{\frac{\rho}{\pi \mu_r \mu_0 f}} \qquad (2.10)$$

where ρ is the resistivity of the material, μ_r is the relative permeability of the material and f is the frequency of the field. For a chrome steel thermoseed the skin depth is ~ 20 μm (calculated using: $\rho = 1.4 \times 10^{-7}$ Ω m, $\mu_r = 100$, $\mu_0 = 1.26 \times$ 10-6 H m^{-1}, $f = 710 \times 10^3$ Hz), which is just 1 % of a 2 mm thermoseed's diameter.

The total power generated via eddy current heating of a spherical thermoseed is given by (Stauffer, Cetas and Jones, 1984):

$$P_E \cong 3\sqrt{2}\pi a^2 \sqrt{\frac{f\mu}{\sigma}} H^2 \qquad (2.11)$$

where a is the radius of the sphere, μ is the magnetic permeability and σ is the electric conductivity of the material.

The second mechanism of heat generation is hysteresis loss, which results from the hysteretic properties of ferromagnetic materials (see section 2.1). When an AMF is applied, energy is delivered to the system allowing domain motion to occur and the net magnetisation vector to oscillate. The energy is subsequently transferred as thermal energy and is characterised by the area of the hysteresis loop (Pankhurst *et al.*, 2003):

$$P_H = \mu_0 f \oint \boldsymbol{H}\, d\boldsymbol{M} \qquad (2.12)$$

Since MINIMA will be performed within the bore of an MRI scanner, the static magnetic field will fully saturate the ferromagnetic thermoseed, preventing its magnetisation from oscillating. As a result, heating will occur from eddy current losses only.

Increasing the amplitude and frequency of the applied field would increase thermoseed heating, as defined by equations 2.11 and 2.12. However, an AMF may also induce eddy currents in tissue exposed to the field, due to the conductivity of biological fluids, which may lead to peripheral nerve stimulation or non-specific heating. To limit non-specific heating, limits on frequency and amplitude have been defined in various studies, with the most commonly quoted being the Brezovich criterion, $Hf < 4.85 \times 10^8$ A m^{-1} s^{-1} (Atkinson, Brezovich and Chakraborty, 1984). However, some studies have used field parameters that exceed this limit, without complaint from patients (Maier-Hauff *et al.*, 2007; Thiesen and Jordan, 2008), and there is still much debate around this topic (Pankhurst *et al.*, 2009).

Discussion on the applications of magnetically mediated thermal ablation is provided in chapters 6 and 7, before experimental results are presented, which explore the heating characteristics of ferromagnetic thermoseeds and show the effect of thermal ablation in healthy and diseased tissue.

3 Imaging background and theory

Chapter 3 introduces the different imaging techniques used in the experiments presented in this thesis. The bulk of the chapter focuses on MRI, as this is the imaging platform on which MINIMA has been developed. CT, ultrasound, and bioluminescence imaging (BLI) are also briefly introduced.

3.1 Magnetic resonance imaging

Performing MINIMA within the bore of an MRI scanner has the inherent advantage of image-guidance. Pre-acquired images will allow an optimum path to be defined from injection site to the target, avoiding essential biological structures and minimising damage to healthy tissue. MRI may also be used to track the thermoseed during the procedure, ensuring it does not deviate from the planned trajectory. Section 3.1 introduces the principles of MRI, the implications of imaging near metal objects using MRI and the hardware of an MRI scanner. The basic MRI concepts have been summarised from the following standard texts: Levitt (2001), Brown (2014), McRobbie *et al.* (2006) and Bernstein, King and Zhou (2004).

3.1.1 Basic principles of nuclear magnetic resonance

Nuclear magnetic resonance (NMR) concerns the behaviour of nuclear spins when subject to a magnetic field. Nuclei are composed of protons and neutrons, which respectively determine the element and isotope of the atom. The combination of protons and neutrons determines the atom's nuclear spin quantum number, I. The nucleus of ^{1}H consists of a single proton and has $I = ½$. Nuclear spin is an intrinsic form of angular momentum.

Quantum theory dictates that the angular momentum of atomic nuclei is constrained to $2I + 1$ possible spin states, ranging from $I, I - 1, \ldots, 0, \ldots, -I$; for ^{1}H there are two possible states, $+ ½$ and $- ½$. In the absence of a magnetic field, the spin states are equal in energy, but this degeneracy is lost when a magnetic field (B_0) is applied. Upon application of B_0, the states are separated by an energy difference $\Delta E = \hbar\omega$, where ω is the angular frequency and $\hbar$ is reduced Planck's constant. In the lower energy state (α) the spins are in parallel alignment with the field, whereas in the high energy state (β) they are oriented anti-parallel (Figure

3.1). For an ensemble of spins at thermal equilibrium, the population of the two states is defined by the Boltzmann distribution:

$$\frac{N_\beta}{N_\alpha} = exp^{-\frac{\Delta E}{k_B T}} \qquad (3.1)$$

where N_β and N_α are the number of nuclei in the upper and lower energy states respectively, k_B is the Boltzmann constant (1.381 × 10^{-23} J K^{-1}) and T is the temperature. The surplus of spins in the lower energy state yields a net magnetisation, M_0.

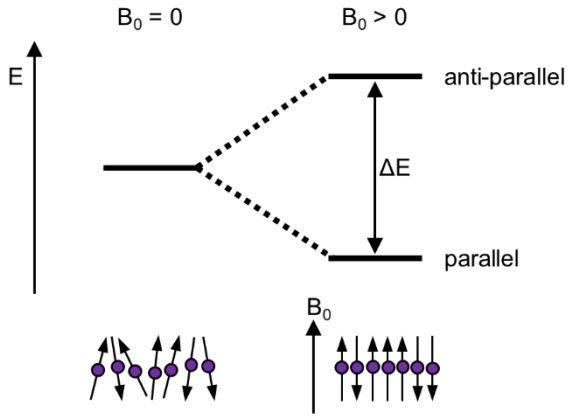

Figure 3.1 Nuclear Zeeman splitting. In the absence of a magnetic field (left) spins are randomly orientated resulting in no net magnetisation. When a magnetic field (B_0) is applied (right), the spins occupy one of two possible states, either parallel or anti-parallel to the magnetic field. Overall, there is a small excess of spins in the lower energy state, aligned with the field, resulting in net magnetisation along the same axis as B_0.

Classical mechanics can be used to describe the interaction of an ensemble of nuclei within an external magnetic field; this interpretation will be used for the remainder of this chapter and going forward the term ‘spins’ will be used to describe an ensemble of nuclei. Upon application of a magnetic field, spins experience a torque and begin to precess about the direction of the field. The frequency at which the spins precess is proportional to B_0 and is defined by the Larmor equation:

$$\omega_0 = -\gamma B_0 \qquad (3.2)$$

where γ is the gyromagnetic ratio. For ^{1}H, $\gamma = 2.675 \times 10^8$ rad T^{-1} s^{-1}, or $\bar{\gamma} = 42.57$ MHz T^{-1}, the highest of all nuclei. This, in addition to its high natural abundance (> 99.9 %), means that ^{1}H is the nucleus with the highest sensitivity. ^{1}H is also one of the most common elements found in biological systems, hence why it forms the basis of magnetic resonance imaging. The vector sum of all nuclear spins within a system gives the net magnetisation, M_0, which is aligned with B_0 when the system is in equilibrium.

To simplify our understanding of magnetic resonance experiments, precession is often modelled in a rotating reference frame. Consider a cartesian coordinate system (x', y' and z') that is rotating about B_0 at $\omega = \omega_0$, with z' and z aligned. If a spin precessing at the Larmor frequency is viewed from within this frame, it would appear to be static, and spins that are precessing at higher or lower frequencies would gain or lose phase respectively.

3.1.2 Relaxation and excitation

Felix Bloch and Edward Purcell discovered the phenomenon of NMR in 1946 (Bloch, 1946; Purcell, Torrey and Pound, 1946), whereby the application of a magnetic field perpendicular to B_0 oscillating at the resonance (Larmor) frequency rotates the spin magnetisation vector into the transverse (x-y) plane. When at equilibrium, the net magnetisation vector lies parallel to the B_0 field, defined as the z axis. Following excitation, spins interact with one another and their surroundings, which gives rise to two relaxation processes, causing the nuclei to lose coherence and the net magnetisation vector to realign with the z axis.

The first relaxation process is called longitudinal relaxation (Figure 3.2A), which is due to spins experiencing fluctuating magnetic fields, arising from the thermal motion of their surroundings. These fluctuations in both direction and magnitude of the local field allows the cone of precession to wander slowly, thus breaking the isotropy of polarization and allowing a net magnetisation to develop along the direction of the applied B_0 field. This relaxation is exponential with decay time constant T_1 and can be described by equation 3.3:

$$M_z(t) = M_0\left(1 - exp\left(\frac{-t}{T_1}\right)\right) \qquad (3.3)$$

Spins also interact with one another. By inducing small fluctuations in the local magnetic field, spins begin to lose phase coherence, which leads to the decay of transverse magnetisation to zero (transverse relaxation, Figure 3.2B). This relaxation process is also exponential, with time constant T_2:

$$M_{\perp}(t) = M_0 exp\left(\frac{-t}{T_2}\right) \tag{3.4}$$

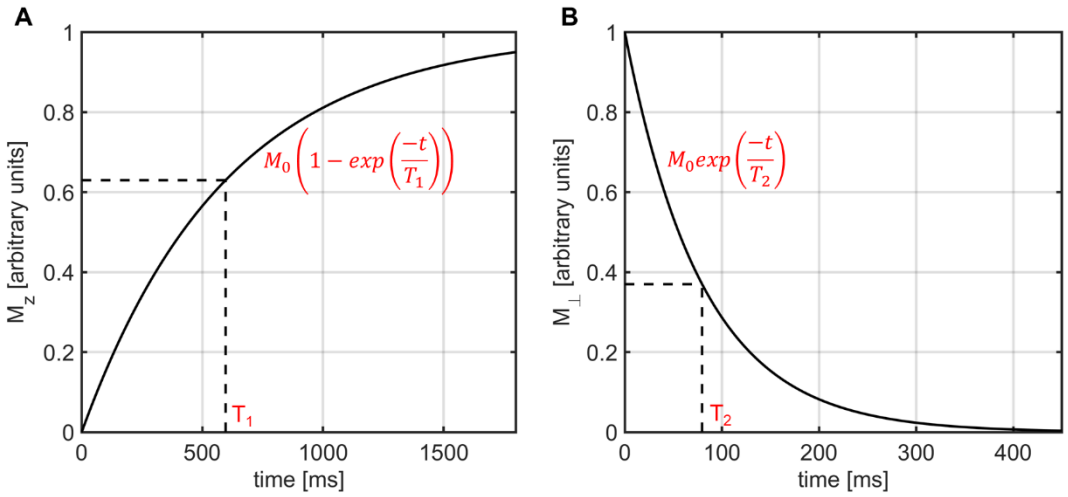

Figure 3.2 Longitudinal and transverse relaxation. Longitudinal relaxation is the return of net magnetisation to thermal equilibrium in alignment with B_0 and with time constant T_1 (left). At T_1, M_z is equal to 63 % of the net magnetisation at equilibrium (M_0). Transverse relaxation is the exponential decay of magnetisation in the x-y plane (orthogonal to B_0), with time constant T_2 (right). At T_2, $M_{\perp}$ is equal to 37 % of the equilibrium magnetisation. Relaxation time constants typical for white matter tissue in the brain have been used in these examples.

Inhomogeneities in B_0 can also contribute to transverse relaxation, with the time constant T_2'. The combination of relaxation due to static and fluctuating fields can be described as T_2*:

$$\frac{1}{T_2^*} = \frac{1}{T_2} + \frac{1}{T_2'} \tag{3.5}$$

It is the variation of time constants and proton density between tissues that allow contrast to be generated in images. The contrast can be adjusted by using different pulse sequences, a protocol detailing the order in which RF pulses, magnetic field gradients and signal acquisition are executed.

The simplest MR experiment is called a free induction decay (FID). This consists of a single pulse, followed by signal detection (Figure 3.3). The RF pulse is a magnetic field perpendicular to B_0 that is oscillating at the Larmor frequency; in the rotating frame this is a static magnetic field, B_1. The flip angle of the RF pulse (α) is defined by B_1 and the period for which the field is applied (τ_{RF}): $\alpha = \gamma B_1 \tau_{RF}$. Once the net magnetisation has rotated into the transverse plane it decays at a rate driven by T_2* relaxation.

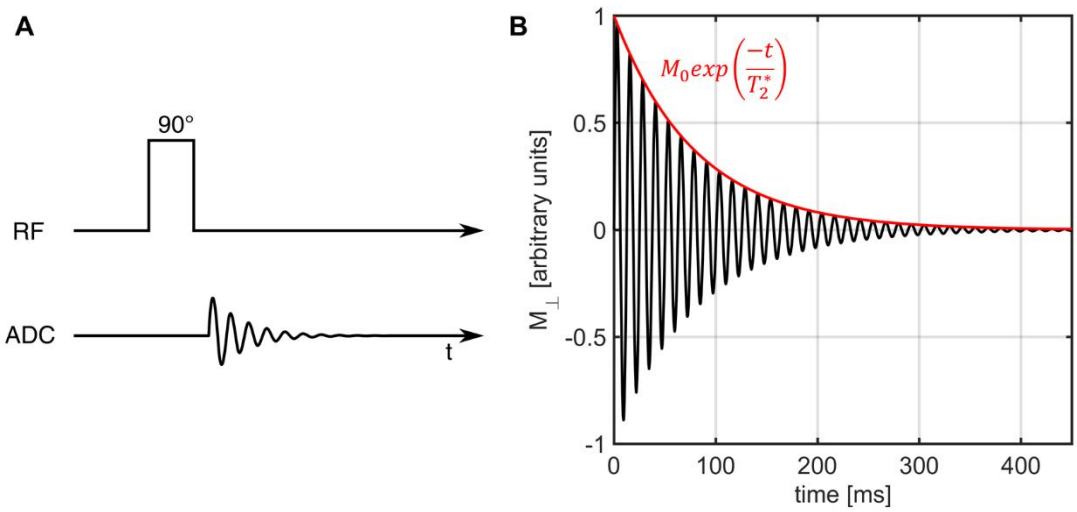

Figure 3.3 FID pulse sequence. A The simplest MRI pulse sequence consists of a single pulse followed by signal detection. Prior to the radiofrequency (RF) pulse, the net magnetisation is aligned with B_0. A 90 ° pulse rotates the net magnetisation into the transverse plane, and the spins precess about B_0 and begin to dephase. **B** The acquired free induction decay (FID) oscillates at the Larmor frequency, within an exponential decay envelope driven by T2* relaxation.

3.1.3 Image formation and k-space

The FID pulse sequence described above is used to acquire a global signal from a sample. To form an image, the signal detected from different locations within the subject need to be distinguishable. This is achieved using spatial localisation techniques: slice selection, frequency encoding and phase encoding.

3.1.3.1 Slice selection

Slice selection involves the application of a magnetic field gradient orthogonal to the desired imaging plane and a frequency-selective RF pulse, which results in spins only within the desired slice being excited. The location of the slice is dependent on the centre frequency of the pulse, and the bandwidth (BW_{RF}) and gradient strength determine the slice thickness (TH):

$$TH = \frac{BW_{RF}}{\gamma G_z} \tag{3.6}$$

Slice thickness can be reduced by decreasing the RF bandwidth or by increasing the gradient strength. Upon application of the slice selection gradient, the spins within the bandwidth of the RF pulse will acquire phase relative to their position across the slice thickness; this dephasing is subsequently refocused by applying a second gradient of equal amplitude, but opposite sign.

3.1.3.2 Frequency encoding

Frequency encoding involves the application of a linear magnetic field gradient during signal acquisition. The gradient creates a linear variation in magnetic field strength across the sample, thus manipulating the relationship in equation 3.8 and causing spins to precess at different frequencies dependent on their position along the gradient axis:

$$B_z(z,t) = B_0 + zG(t) \tag{3.7}$$

$$\omega(z,t) = \omega_0 + \gamma zG(t) \tag{3.8}$$

The resulting detected signal contains a range of frequency components, which can be analysed using the Fourier transform to give a profile of the sample projected onto the gradient axis.

3.1.3.3 Phase encoding

Phase encoding is used to obtain spatial information along the second in-plane axis, perpendicular to the frequency encoding axis. This involves the application of a magnetic field gradient for a finite time period prior to frequency encoding and signal acquisition. While the gradient is switched on, the spins gain or lose phase depending on their spatial location. Once the gradient is switched off, all spins revert to the same frequency of precession, however, their accumulated phase is retained. The resulting phase angle is dependent on the position of the spins along the phase encoding gradient axis. This process is then repeated with incrementally higher phase encoding gradient amplitudes, resulting in spins accumulating more phase. If this is repeated several times, equivalent to the desired number of pixels in the final image, the collective phase shifts form an

oscillating signal that can be analysed using the Fourier transform. Imaging can also be performed in 3D by exciting a slab, performing phase encoding along two axes and frequency encoding along the third axis; this allows large volumes to be imaged within 3D isotropic resolution.

3.1.3.4 Basic pulse sequences

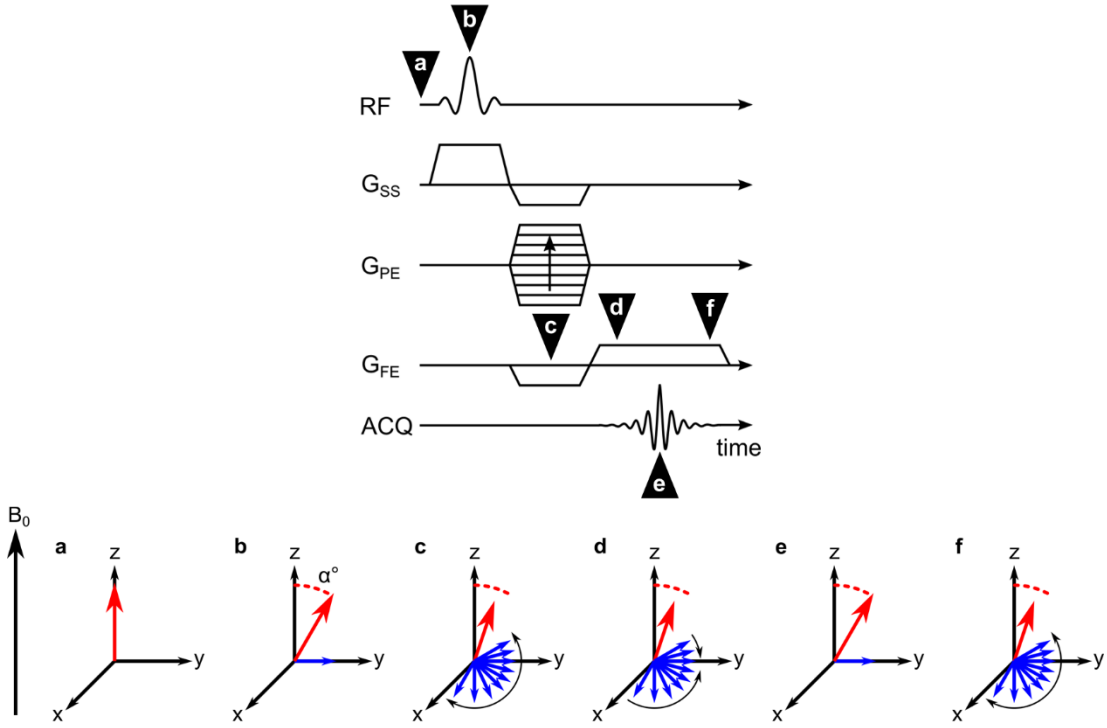

Figure 3.4 Gradient echo pulse sequence. Order of RF pulses and gradient waveforms and the corresponding effects on net magnetisation (red) and spins (blue). **a** The system is in equilibrium, with the net magnetisation aligned with B_0. **b** Spins are excited by an RF pulse with flip angle α°. **c** Spins are dephased by gradients. **d** Spins are rephased by frequency encoding readout gradient. **e** Signal echo occurs are the centre of the readout gradient. **f** Spins continue to dephase.

Gradient echo and spin echo are the two main pulse sequences that are used in MRI, each using slice selection, frequency encoding and phase encoding to form an image. Both sequences are extensions of the simple FID; the main distinction between the two is the method of echo formation. In the gradient echo sequence, a gradient of negative polarity is first applied along the frequency encoding axis to dephase the spins. Subsequently, when a readout gradient of equal magnitude but opposite polarity is applied, the spins begin to gain coherence and form an echo (Figure 3.4). In a spin echo sequence, a 180 ° refocusing pulse is applied at time τ after the initial excitation pulse, causing the spins to be rotated 180° and

their order with respect to the direction of precession to be reversed. The spins rephase and form an echo at time τ after the refocusing pulse (Figure 3.5). Each sequence has distinct advantages, with the gradient echo being typically faster, and the spin echo having a greater signal-to-noise ratio.

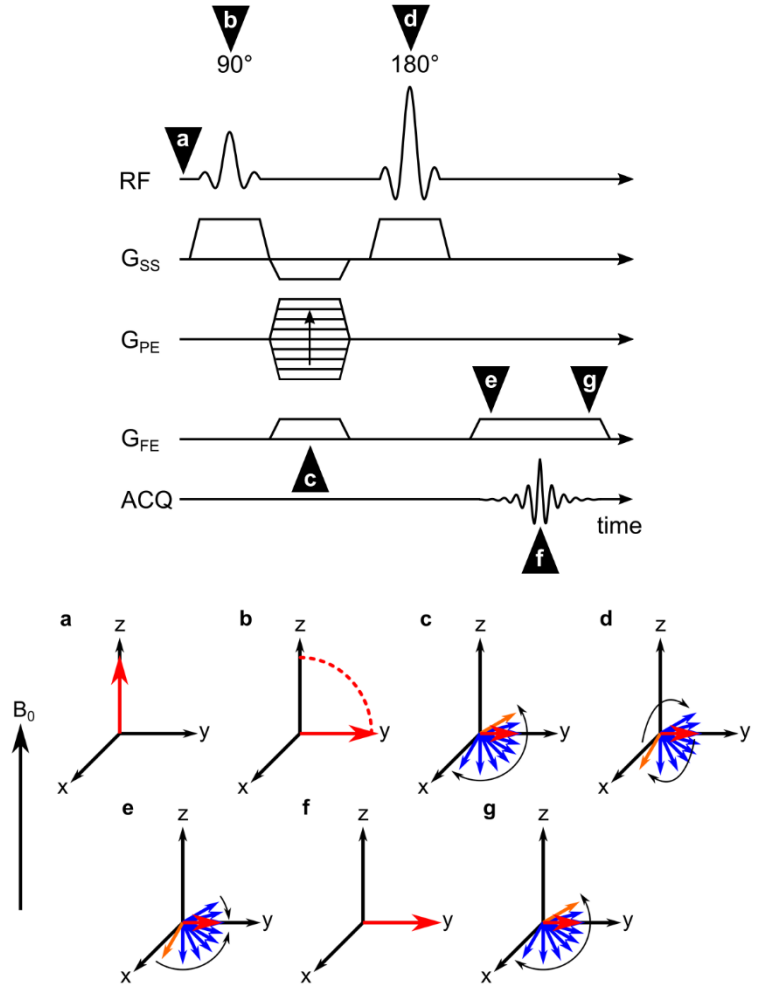

Figure 3.5 Spin echo pulse sequence. Order of RF pulses and gradient waveforms and the corresponding effects on net magnetisation (red) and spins (blue/orange). **a** The system is in equilibrium, with the net magnetisation aligned with B_0. **b** Spins are excited by an RF pulse, with a flip angle of 90° typically used in simple scans. **c** Spins are dephased by gradients and static field inhomogeneities. **d** An RF pulse rotates spins 180°, which causes spins to refocus and the loss of phase coherence due to static magnetic field inhomogeneities to be reversed. **e** Spins are rephased by the frequency encoding readout gradient. **f** Signal echo occurs are the centre of the readout gradient. **g** Spins continue to dephase.

3.1.3.5 K-space

K-space is a matrix representing spatial frequencies in an image, with the k_x and k_y axes corresponding to spatial frequencies along the x and y axes of the image respectively. Data points at the centre of k-space contain low spatial frequency

information, determining the basic image contrast, and the edges contain high spatial frequency information, defining the edges and fine details of the image. k is dependent on time and gradient amplitude:

$$k(t) = \gamma \int_0^t G(t')dt' \qquad (3.9)$$

The data points within k-space are filled with the signal received during an MRI scan; each row contains a frequency encoded echo acquired with a different phase encoding gradient amplitude (Figure 3.6). Performing a 2D fast Fourier transform of k-space converts the spatial frequency data into a complex image. Anatomical images that people are most familiar with are magnitude images, which are calculated by taking the modulus of the real and imaginary data.

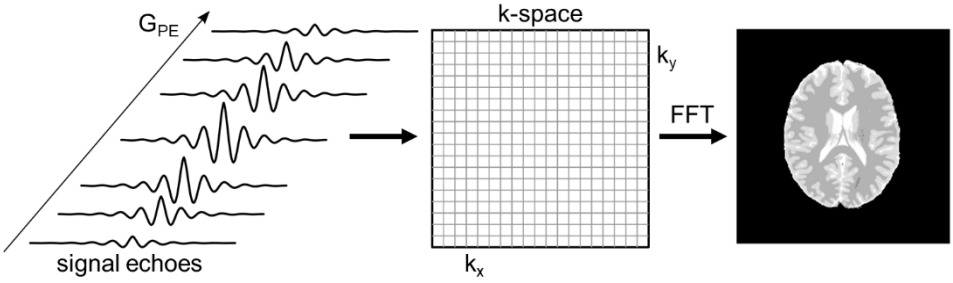

Figure 3.6 From echoes to images. Each echo forms a line in k-space. Multiple echoes are acquired with incremented phase encoding gradients to form a 2D matrix in k-space. An image is generated by performing a 2D fast Fourier transform on the k-space matrix.

3.1.4 Imaging near metals

3.1.4.1 Susceptibility and metal artefacts

Susceptibility is the extent to which a material is magnetised when subjected to an external magnetic field. When tissues of differing susceptibilities are neighbouring one another they interact, leading to distortions in the local magnetic field. This causes an increased rate of dephasing in the protons on either side of the boundary, which manifest as areas of signal loss within the image.

Metal artefacts are similar to susceptibility artefacts, but are much more disruptive, with large areas of signal loss, signal pile-up and geometric distortion (Figure 3.7). This is due to the large disparity in magnetic susceptibility between

most metals and biological tissue, which creates large field inhomogeneities around the foreign object. The appearance of artefacts can be improved by using spin echo pulse sequences (Eustace *et al.*, 1997), much higher receiver bandwidths and short echo times (Port and Pomper, 2000); however, these are unlikely to eradicate artefacts completely. This is of particular importance to the MINIMA project, as the thermoseeds used are made from chrome steel, a ferromagnetic alloy.

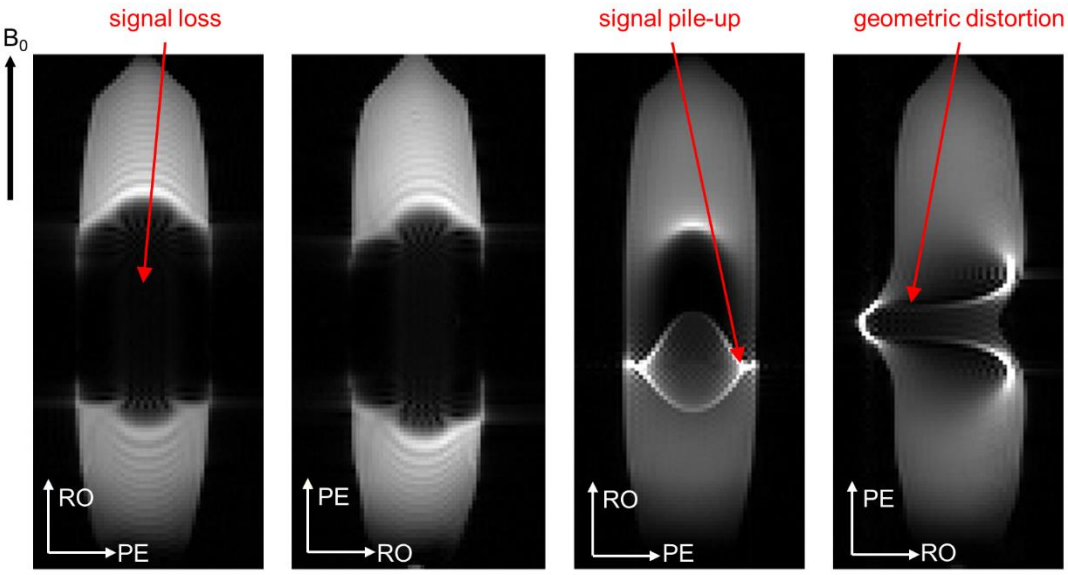

Figure 3.7 Metal artefacts. Images acquired of a 2 mm chrome steel, spherical thermoseed in agar. Gradient echo images (left, centre-left) have large regions of signal loss, whereas spin echo images (centre-right, right) exhibit severe geometric distortion and signal pile-up. Altering the readout (RO) and phase encoding (PE) directions can alter the appearance of the artefacts.

Various pulse sequences have been developed to improve image quality near metals. For example, view-angle tilting (VAT) applies an additional slice-select gradient simultaneously with the frequency encoding gradient (Cho, Kim and Kim, 1988). This tilts the readout axis towards the slice selection axis, which causes a shearing of the voxels and removes all in-plane geometric distortion. It does not, however, remove any through plane distortions and, due to the voxel shearing, additional blurring is introduced (Jungmann *et al.*, 2017).

Another technique is multi-spectral imaging (MSI), which includes the sequences SEMAC (slice-encoding for metal artefact corrections) and MAVRIC (multi-acquisition variable-resonance image combination). SEMAC uses VAT in

combination with 3D imaging to overcome the through slice distortions (Lu *et al.*, 2009; Ai *et al.*, 2012). Phase-encoding is additionally performed along the slice-select axis, thus providing spatial localisation of spins external to the slice. MAVRIC uses a non-slice-selective RF pulse before performing 3D imaging. This process is repeated using pulses centred at different frequencies, thus covering the spectrum of resonance frequencies around the metal object (Koch *et al.*, 2009; Hargreaves *et al.*, 2018). For both methods, the 3D images are combined to give a single composite image. Although SEMAC and MAVRIC remove both in-plane and through-plane distortions, the repeated 3D imaging makes the process very time-consuming. These sequences may be useful when imaging the tissue around the ferromagnetic thermoseed, however, it is unlikely that they will be able to delineate the thermoseed edge exactly.

3.1.4.2 Magnetic signature selective excitation (MS-SET)

The thermoseeds used in all experiments presented in this thesis are spheres made from chrome steel that has a saturation magnetisation of 1.36×10^6 A m^{-1} (Martel *et al.*, 2009). The magnetic field induced by a sphere can be described as a single dipole (Brown *et al.*, 2014):

$$\Delta B_z = \frac{\Delta\chi}{3+\Delta\chi}\left(\frac{a}{r}\right)^3 (3\cos^2\theta - 1)M_s \qquad (3.10)$$

where $\Delta\chi$ is the difference in magnetic susceptibility between the sphere and the surrounding medium, a is the radius of the sphere, r is the distance from the centre of the sphere and θ is the polar angle from $\boldsymbol{B_0}$. This equation is only valid if the sphere is in an external magnetic field greater than its saturation magnetisation, otherwise M_s should be replaced with B_0. Simulated changes in precession frequency surrounding a 2 mm chrome steel sphere in a magnetic field > 1.7 T, calculated from equation 3.10, are presented in Figure 3.8. With the frequencies as high as 4×10^7 Hz off-resonance, the observed susceptibility artefacts are extensive (Figure 3.7). The large regions of signal loss and the geometric distortions make it difficult to identify the position of the thermoseed as well as disrupting the surrounding image.

MS-SET, a method specifically designed to track ferromagnetic spheres using MRI, was developed by Sylvain Martel's group to ensure accurate navigation of an untethered seed through the artery of a swine (Felfoul *et al.*, 2008; Aboussouan and Martel, 2006; Martel *et al.*, 2007). This tracking method uses off-resonance selective excitation and the magnetic field induced by a ferromagnetic sphere to create a unique signature (Felfoul *et al.*, 2008, 2009). When a non-slice-selective excitation pulse is applied offset from the Larmor frequency, the selectivity of the excitation is defined by the magnetic field induced by the ferromagnetic material. This will create a positive contrast signature, with no signal from the surrounding sample. Typically, projection images are acquired using this technique, where a large sample volume or slab is excited, and the signal is condensed onto a single axis or plane, resulting in 1D and 2D projections respectively. Images of a 2 mm chrome steel thermoseed acquired using this method are shown in Figure 3.9.

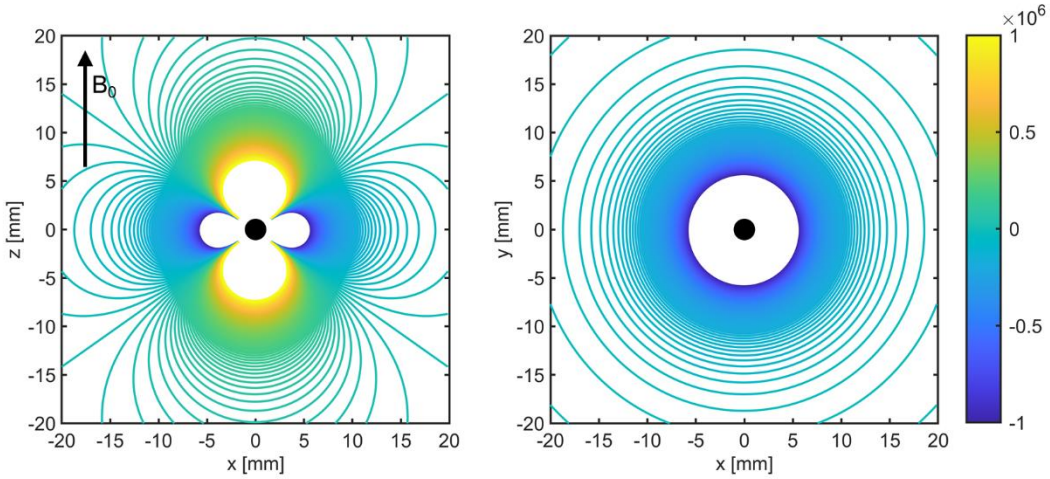

Figure 3.8 Magnetic field induced by a thermoseed. Simulation of the magnetic field induced by a saturated, 2 mm diameter chrome steel sphere, calculated using equation 3.10 (M_s = 1.36 × 10^6 A m^{-1}).

To determine the position of the thermoseed, two 1D projections are acquired along each axis, one with a positive readout gradient and one with a negative readout gradient. As distortion occurs primarily along the readout gradient direction, any shift in the signal when using a positive gradient will be reversed when using a negative gradient (Aboussouan and Martel, 2006). The centre of the signal signature within each projection, and therefore the position of the thermoseed, can be determined by performing a convolution (Aboussouan and

Martel, 2006). Convolving the positive and negative gradient projections will give a peak when the two signatures overlap (Figure 3.10); at this point, the displacement of the mask (negative projection) will be equal to twice the absolute position of the thermoseed, with respect to the isocentre of the MRI scanner. In practice, the projection acquired with a negative readout gradient is already flipped, and a cross correlation is used instead of a convolution.

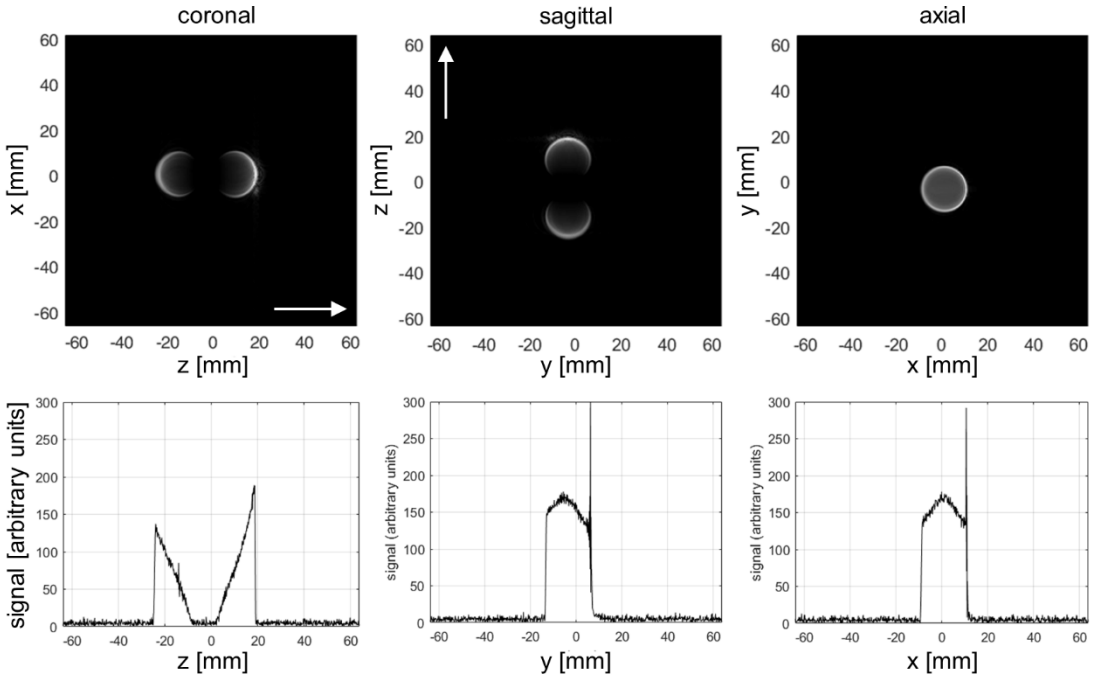

Figure 3.9 1D and 2D off resonance imaging projections. 2D (top) and 1D (bottom) off-resonance projection images acquired of a 2 mm chrome steel thermoseed. A spin echo sequence was used to acquire these projections with an excitation frequency offset and bandwidth of +3 kHz and 1 kHz respectively. White arrows indicate the direction of the B_0 field.

Once the absolute position of the thermoseed is known, a similar method can be used to measure its relative movement, which only requires the acquisition of a single projection along each axis (Felfoul *et al.*, 2009). The positive gradient projection from position 1 is used as a mask and correlated with the positive gradient projection from position 2. The maximum in the correlation is then directly related to the distance moved by the thermoseed.

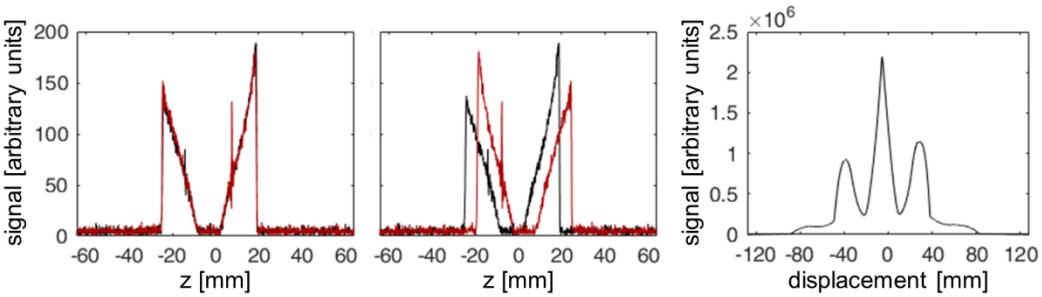

Figure 3.10 Cross correlation of 1D projections. 1D off-resonance projections acquired with a positive readout gradient (black) and negative readout gradient (red). The position of the thermoseed along the z axis can be identified as the centre of the two off-resonance signatures (left). This can be achieved using a convolution. In practice, the 1D projection acquired with the negative readout gradient is already flipped (centre) and therefore a cross correlation is performed, instead of a convolution. The peak of the resulting correlation (right) is directly related to the absolute position of the thermoseed along the z axis.

3.1.5 MRI hardware

An MRI scanner typically consists of the magnet that generates the B_0 field, the magnetic field gradient coils, the RF transmit system and the receive coils. A schematic depicting these different components is presented in Figure 3.11.

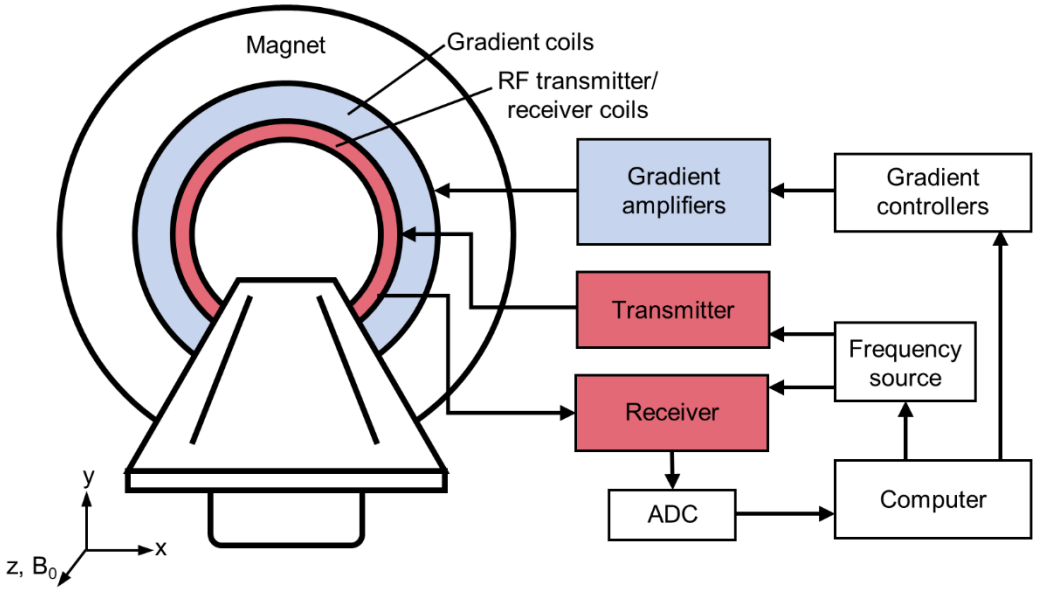

Figure 3.11 Schematic of MRI scanner hardware. The superconducting magnet is indicated by the outer circle. The gradient coils (blue) are positioned within the bore of the magnet. A computer provides an interface to prepare pulse sequences and view acquired images. The gradient controllers generate a gradient waveform, which is amplified by the gradient amplifiers. The frequency source produces an RF waveform, which is amplified by the RF amplifier. An RF receiver coil (red) detects induced currents from the excited spins, which is digitised and sent to the computer. ADC = analogue to digital conversion.

Superconducting magnets are most commonly used for MRI systems, as they provide the best field homogeneity, stability, and the highest field strengths. For clinical systems the field is typically 1.5 or 3 T, however, for preclinical research fields up to 21 T are used (Schepkin *et al.*, 2010). The majority of experiments presented in this thesis were conducted using a 9.4 T Bruker Biospec 94/20 system (Bruker, Germany).

Gradient coils are positioned within the bore of the magnet and generate linear magnetic field gradients across the sample. These are essential for spatial localisation of the MR signal. Three sets of coils are used to vary the z-component of the B_0 field along the x-, y- and z axes. It is these gradients that can exert a force on magnetic particles and devices, allowing them to be navigated within the bore of the MRI scanner. The gradient coil used for most of the work presented in this thesis can generate gradient amplitudes of up to 979 mT m^{-1}.

A radiofrequency coil is placed inside the gradient coils and the main magnet. This is used to generate RF pulses at the required frequency, bandwidth, and amplitude to excite nuclei within the correct slice geometry, as defined by the pulse sequence. A single coil can be used to transmit the RF pulses and receive the MR signal, however, a dedicated receive surface coil is often used to achieve a higher signal-to-noise ratio.

3.2 Computed tomography imaging

CT imaging is one of the most widely used techniques in diagnostic radiology, due to its low running costs, ease of use and short scan times. The principles of CT imaging are based on the interaction of x-rays with different biological tissues. X-rays are typically generated by a source that rotates around the patient and are sent through the body, where they are scattered and absorbed by different tissues. This leads to an attenuation in the x-rays, which is picked up by an array of detectors positioned opposite the source. This process is completed at multiple angles around the patient, resulting in a collection of 2D projection images, which are subsequently reconstructed to give a 3D topographic image. The contrast within a CT image is associated with the electron density of tissues. Bone has a high electron density when compared to soft tissues, which is why fractures are often assessed using x-rays. However, there is little difference in electron density

between different soft tissues, resulting in poor image contrast. This is a key disadvantage of CT compared to MRI.

In chapter 4, CT is used to assess the accuracy of thermoseed localisation using MRI. This is achieved be comparing images of a custom-designed phantom acquired with the two imaging modalities.

3.3 Ultrasound imaging

Ultrasound is a non-invasive imaging modality that is widely used in the clinic. Images are formed using high-frequency soundwaves, typically 1 – 20 MHz, that are generated using a piezoelectric crystal found in the ultrasound transducer. Different frequencies are used depending on the application, with lower frequencies providing further penetration, but poorer spatial resolution, and higher frequencies providing more detailed images, but at a cost to penetration depth. As the soundwaves are sent through the body, they interact with different tissues through reflection, absorption, and scattering. These processes can be defined collectively as acoustic impedance. Returning soundwaves are received by the transducer and converted back to electrical energy. The final image is constructed based on the amplitude, time, and frequency of the received echoes.

Since ultrasound has a high temporal resolution, it is often used for image-guided injections both in the clinic (Daniels *et al.*, 2018) and for preclinical studies (Prendiville *et al.*, 2014). Ultrasound is used in a similar fashion in chapter 6 to position a temperature probe within ex vivo tissue, enabling the measurement of temperature changes at varying distances from a heated thermoseed.

3.4 Bioluminescence imaging

Bioluminescence is the emission of visible light that occurs naturally in animals, such as the firefly and is responsible for their characteristic glow. Photon emission is the product of an enzymatic reaction between the substrate luciferin, oxygen, and the enzyme luciferase (Figure 3.12).

Bioluminescence imaging is an optical imaging technique that exploits this natural phenomenon to study biological processes in vivo, in real-time. Translation into a biomedical research tool is achieved by modifying cell lines of interest to

express the protein luciferase. These cells can then be studied in vitro or injected into small mammals that do not express the luciferase enzyme endogenously for in vivo experiments. The substrate is then added to the cells or injected via intraperitoneal (i.p.), intravenous (i.v.) or subcutaneous injection. Once the substrate encounters the enzyme, the reaction occurs, light is emitted, and the photons can be subsequently detected using a cooled charge-coupled device (CCD) camera (Figure 3.12).

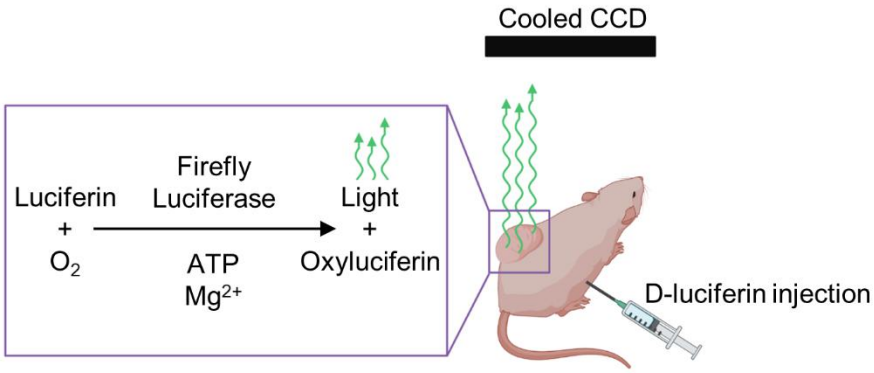

Figure 3.12 Bioluminescence reaction and imaging setup. A bolus of D-luciferin is injected intraperitoneally and reacts within the firefly luciferase-expressing cancer cells to emit photons of light. The emitted light is subsequently detected by a cooled charge-coupled device. The reaction requires ATP and can therefore be used to measure cell viability.

The most commonly used luciferase is from the firefly (*Fluc)*, which requires adenosine triphosphate (ATP) and Mg^{2+} for the reaction to occur, making this technique suitable for monitoring cell viability. In addition, the light emitted from *Fluc* has a peak emission at 562 nm, a long wavelength that improves tissue penetration and, therefore, allows an imaging depth of several centimetres. Other advantages of BLI include its high signal-to-noise ratio, due to intrinsically low bioluminescence of mammalian tissues, and its non-invasiveness, allowing ongoing investigations of biological processes without experimental animals having to be culled.

A key limitation of BLI is poor image resolution, which is due to diffuse light emission caused by the absorption and scattering of light as it passes through tissue. Depth of emission is also important, with superficial tissues giving higher signal than internal organs. Several other factors can also affect the measured signal, including changes in optical properties of tissue (Sadikot and Blackwell,

2005) and the dependence on multiple reactants, which, if lacking in abundance, could become reaction rate limiting. BLI is therefore considered to be a semi-quantitative technique.

Common in vivo applications of BLI include the tracking of stem cells (Thin *et al.*, 2020), monitoring tumour growth and metastasis (Drake, Gabriel and Henry, 2005) and measuring response to therapy (Zhao *et al.*, 2008). BLI is used in the experiments presented in chapter 7 to monitor tumour growth and response to thermal ablation therapy in vivo.

Having introduced the key concepts and imaging modalities used in this thesis, the following chapters cover the initial proof-of-concept studies of the MINIMA project. Chapter 4 focuses on the setup of the MRI scanner, implementing thermoseed tracking and navigation on the preclinical system in CABI. Following this, chapter 5 covers optimisation of thermoseed navigation in a viscous fluid, before attempting to navigate a thermoseed through tissue. The final two results chapters, 6 and 7, cover the heating component of the project, characterising thermoseed heating in vitro and studying its efficacy as a cancer therapy in a mouse tumour model. A final discussion on the presented data and the resulting implications for the MINIMA project are presented in chapter 8.

4 Thermoseed imaging and navigation on a preclinical MRI system

4.1 Introduction

MINIMA uses an MRI scanner not just to guide the procedure, but also as the driving mechanism to deliver the therapy. This alternative application undoubtedly demands different hardware specifications than those required for imaging, with the main consideration being the gradient coils used to exert a propulsion force on the thermoseed. In MRN studies performed to date, preclinical experiments have used both existing clinical imaging coils (Mathieu *et al.*, 2003; Mathieu *et al.*, 2005) and coils specifically designed for propulsion (Mathieu and Martel, 2007; Pouponneau, Leroux and Martel, 2009), which can generate up 80 mT m^{-1} and 400 mT m^{-1} gradient amplitudes respectively. In some cases, bench-top electromagnets have been designed to generate single-axis magnetic field gradients up to 140 mT m^{-1}, mimicking those generated by the MRI scanner, but with greater ease and at a lower cost (Leclerc *et al.*, 2018). Considering the different approaches taken in the literature, it was important to assess the equipment that may be used in the development of MINIMA, to ensure the project's potential would be investigated to its fullest.

At the UCL Centre for Advanced Biomedical Imaging (CABI) there are two 9.4 T preclinical MRI scanners that are available for research purposes. One is a Varian Inova (Varian, USA) that has three compatible imaging gradient sets, one of which has been designed by collaborators at Tesla Engineering Ltd. specifically for propulsion, to generate 1000 mT m^{-1} gradients continuously for a sustained period of time, along all three axes. The second system is a Bruker Biospec 94/20 (Bruker Germany), which has two imaging gradient sets that can achieve gradient strengths up to 440 mT m^{-1} and 997 mT m^{-1}. Although these specifications suggest that the Tesla gradient coil should enable greater forces to be exerted on the thermoseed, factors other than gradient strength may affect the ability to propel the thermoseed, such as the duration for which the gradients can be applied without overheating. Therefore, initial experiments investigating the maximum duration for which different gradient strengths could be applied continuously were performed on both systems. The results were subsequently

used to inform on which MRI system and gradient coils would be taken forward in the development of MINIMA and used throughout the work presented in this thesis.

Another aspect of the project that had to be considered in the early stages of development was the ability to track the movement of the thermoseed using MRI. This is important not only for patient safety in potential future clinical applications, but also to ensure preclinical experiments were performed with a high level of accuracy. As discussed in chapter 3, imaging a thermoseed is particularly difficult due to the metal artefacts caused by its ferromagnetic properties. To a certain extent, this is even more challenging in the preclinical setting due to the smaller imaging field of view (FOV) available on a preclinical MRI system, 12 cm ± 10 ppm homogeneity (Bruker, 2021), compared with 50 cm ± 1.1 ppm homogeneity on a clinical system (Siemens Medical Solutions USA, 2021).

Currently, the most promising technique used for tracking ferromagnetic spheres is magnetic signature selective excitation (MS-SET) (Martel *et al.*, 2015), as described in section 3.1.4.2. Since its original development (Aboussouan and Martel, 2006; Felfoul *et al.*, 2008; Felfoul *et al.*, 2009) and application, tracking a ferromagnetic sphere through the vasculature of a swine (Martel *et al.*, 2007), this method has been shown to be accurate to within 0.3 mm and has been successfully adapted for other technologies, such as the tracking of ferromagnetic-tipped catheters (Zhang *et al.*, 2010; Lalande *et al.*, 2015). Therefore, I aimed to implement and assess the accuracy of this technique on the MRI system in CABI, thus providing a method to reliably track the thermoseed in future experiments. Furthermore, I planned to edit the pulse sequence, adding propulsion gradient pulses that would allow the thermoseed to be propelled and tracked using a single sequence.

The final challenge in setting up the MRI scanner to be used for MINIMA concerned the ability to pass the ferromagnetic thermoseed through the fringe field and into the bore of the scanner safely. Due to the large fringe field of the MRI magnet (Figure 4.1), a large force is exerted onto the thermoseed as it enters the bore, which may cause it to move unexpectedly. This must be considered

when designing preclinical experiments, but more importantly must be addressed for any future clinical translation, to ensure patient safety.

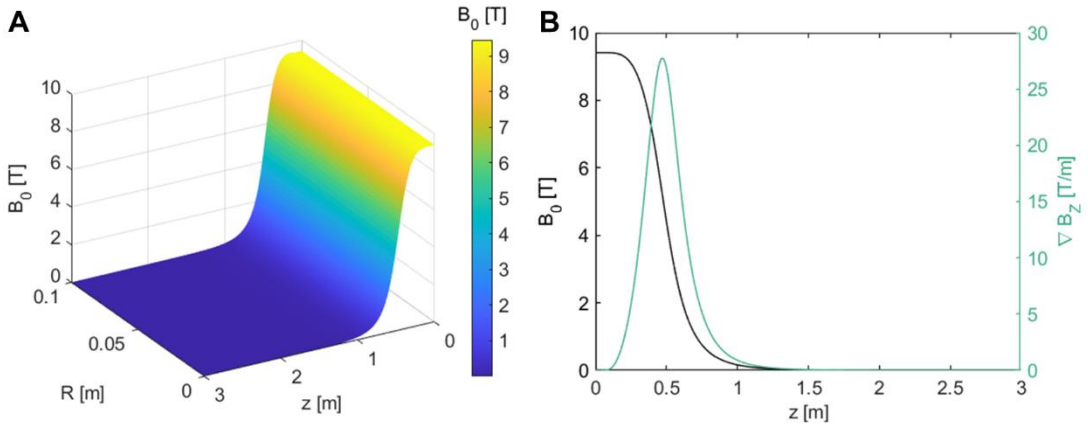

Figure 4.1 9.4 T Bruker MRI scanner fringe field. A Simulated magnetic field of the 9.4 T Bruker Biospec 94/20 MRI system, from the isocentre up to 3 m along the z axis (along the magnet bore and direction of the main magnetic field) and 0.1 m radially. **B** 1D plot of the simulated magnetic field along the z axis and the z component of the magnetic field gradient. A maximum magnetic field gradient of 28 T m^{-1} occurs at 0.47 m from the isocentre.

One possible solution is a brute force approach, in which the thermoseed is inserted into the subject outside the scanner and physically held in place as the subject enters the scanner bore. This simple and practical solution is attractive for preclinical experiments, particularly for in vitro work, for which phantoms can be designed with this in mind. Phantoms designed for this purpose have been used for experiments presented in this thesis and will be discussed in more detail in chapter 5. A similar approach could be achieved in patients or animals, and Martel *et al.* (2007) have shown how a catheter holding a ferromagnetic sphere can be positioned in a blood vessel while the animal passes through the fringe field of a clinical MRI scanner. However, this does carry some risk if the thermoseed cannot be navigated back to the catheter for removal.

A second approach is to insert the thermoseed once the subject is already positioned within the MRI scanner. This method is perhaps too complex for preclinical studies, especially when working with small rodents. However, it may be possible in patients by adapting pre-existing MR-compatible tools, such as MR-compatible needles designed for image-guided prostate biopsies (Krieger *et al.*, 2013) and stereotactic needle insertion into the brain (Masamune *et al.*, 1995; Patel *et al.*, 2020).

A neat solution is to simply switch off the main magnetic field. With the field at 0 T, the patient can be positioned within the MRI scanner before the field is ramped up to the required strength for the procedure and then switched back off once the procedure is complete. This would not only ease the insertion and removal of the thermoseed but would act as an additional safety measure throughout the procedure. However, switching the main magnetic field of an MRI scanner on and off is not something that is routinely done, due to the time it takes. The Siemens Helicon MRI scanner developed in the 1980's could ramp from 0 to 2 T within 25 minutes, but required a further hour for the field to stabilise (Reichert *et al.*, 1988); this amounts to an additional 2 hours spent in the scanner for the patient. There is, however, potential for this time to be reduced. A cryogen-free, preclinical MRI scanner recently developed by Rigla *et al.* (2020) can ramp up to 1 T, with the field stabilising within 1 minute. Similarly, the DryMag scanner from MR Solutions can ramp from 0 to 9.4 T within just a few minutes (MR Solutions, 2021). These recent developments in the preclinical arena will most likely be integrated into clinical scanners in time. Working with collaborators at MR solutions, I aimed to test this approach.

To summarise, the aims of the experiments presented in this chapter are:

1. To assess which of the two MRI scanners available in CABI should be used throughout my PhD and in the development of MINIMA
2. To implement MS-SET and assess its accuracy in locating ferromagnetic thermoseeds on the preclinical MRI system
3. To incorporate propulsion gradients into the imaging pulse sequence, thus enabling navigation of ferromagnetic thermoseeds using the MRI scanner
4. To assess the use of a rampable MRI scanner to safely insert and remove the thermoseed

4.2 Methods

4.2.1 Bruker vs. Tesla gradient coil performance

4.2.1.1 Bruker system

The Bruker system was a 9.4 T Biospec 94/20 fitted with a shielded imaging gradient set (BFG 65-100) that could achieve a maximum gradient strength of

979 mT m^{-1} and a slew rate of 9777 T m^{-1} s^{-1}. First, the maximum duration for which the gradients could be applied continuously along each of the three axes (x, y and z,) was determined in the gradient simulation platform provided in the Bruker Paravision 6.0.1 software. This was done in an iterative process, starting with an on time of 100 ms and incrementally increasing the on time until the simulation platform calculated a duty cycle of 95 – 100 %. Once the maximum duration had been determined in the simulation platform, the pulse sequence was run on the MRI system to test the hardware limitations manually. This process was repeated across a range of gradient strengths (300 – 979 mT m-1) starting with the largest, and once a gradient strength was reached that could run for 1 minute continuously, it was assumed that all lower gradient strengths could also be run indefinitely.

4.2.1.2 Tesla gradient coil

The propulsion coil was designed to fit a 9.4 T Varian Inova preclinical MRI system (Varian, USA) and produce 1000 mT m-1 gradient amplitudes at 100 % duty cycle, along the x, y and z axes, with a slew rate of 55000 – 78000 T m^{-1} s^{-1}. The performance of the gradient coils was tested in a similar manner to the Bruker system, by recording the maximum duration for which the gradients could be switched on continuously at different gradient strengths and along each of the three axes. Unlike the Bruker system, the software did not provide a duty cycle simulator, and therefore, the maximum duration was found empirically by running the gradients for increasing durations. If the maximum on time was exceeded, the MRI system would switch off due to overheating. At this point the gradient duration would be decreased by small amounts until the pulse sequence could be run without the system shutting off, thus determining the maximum possible duration for a given gradient strength. These experiments were performed by my colleague Matin Mohseni.

4.2.2 Thermoseed imaging sequence validation

4.2.2.1 Phantom preparation

Phantoms were prepared using 3 % (w/v) agar solution (Sigma Aldrich, USA) that was poured into the container and left to set at room temperature. Spheres were positioned at different heights within the container by cooling a layer of agar until set, laying a sphere on the surface and pouring hot agar over the top to create

the next layer. A 250 mL bottle was used for the container in phantom designs 1 and 2, and a 50 mL Falcon tube was used in phantom design 3. In design 1, 4 × 0.5 mm diameter thermoseeds were spaced evenly throughout the phantom volume, whereas in designs 2 and 3, a single 0.5 mm thermoseed was positioned in the centre of the phantom, with 3 × 2 mm diameter plastic spheres positioned around it, acting as fiducial markers.

4.2.2.2 Magnetic resonance imaging

Parameter	Phantom design 1	Phantom design 2		Phantom design 3	
	MS-SET	MS-SET	FSE	MS-SET	FSE
Repetition time (TR) [s]	1	1	3.6	1	2
Echo time [ms]	-	-	3.73	-	5.12 *4.26
Field of view (FOV) [mm]	50 #100	128	100 × 50	80	80 × 40 *40 × 40
Matrix size	1024	1024	512 × 256	1024	1024 × 512 *512 × 512
Resolution [µm]	48.8 #97.7	125	195 × 195	78.1	78 × 78
Slice thickness [mm]	-	-	1	-	1
Acquisition bandwidth (acqBW) [kHz]	250	250	500	200	600
Number of averages	100	1	1	8	4
Total scan time [min:s]	-	-	1:55	-	34:8
Excitation frequency offset (excOffset) [kHz]	5	3	-	3	-
Excitation bandwidth (excBW) [kHz]	5	1	-	1	-

Table 4.1 MRI acquisition parameters used for each phantom design in the imaging validation study. The magnetic signature selective excitation (MS-SET) method was used to determine the coordinates of the ferromagnetic thermoseeds. #For phantom design 1, a different FOV and resolution was used for the z axis. A 2D fast spin echo (FSE) sequence was used to determine the centre of mass of the plastic fiducial markers. FSE images were acquired in all three planes. *A different FOV, matrix size and TE was used for the axial orientation.

Images were acquired using a preclinical 9.4 T Bruker Biospec 94/20 MRI system (Bruker, Germany). The coordinates of the plastic spheres were determined using a multi-slice fast spin echo pulse sequence and the projections used to determine the coordinates of the thermoseeds were acquired using a 1D non-slice-selective spin echo sequence. 1D projections were acquired twice along each axis, once with a positive readout gradient once with a negative readout gradient. The parameters used for each sequence and phantom design were optimised via an iterative process and are detailed in Table 4.1.

4.2.2.3 Computed tomography

CT images of the different phantom designs were acquired, from which ground-truth distances between each of the thermoseed-marker pairs could be determined. CT images were acquired using a nanoScan PET/CT scanner (Mediso, Hungary). The FOV covered the entire phantom volume, and the images were reconstructed using the vendor software to a resolution of 251 μm^3.

4.2.2.4 Image analysis

In the MR images, the centre of mass of the plastic spheres were determined from a circular region of interest (ROI) drawn over the slice in which the circular signal void was largest. Each image gave two in-plane coordinates, which were averaged across the three images to give the final coordinates of the spheres. The analysis was performed using Analyze tools available in ImageJ (Rueden *et al.*, 2017).

For the chrome steel sphere, a cross correlation was performed between the positive and negative gradient 1D projections acquired for each axis. The location of the maximum in the resulting correlation was divided by 2 to give the coordinates of the sphere with respect to the isocentre. This analysis was performed using a custom script in Matlab (Mathworks, USA).

In the CT images, the in-plane coordinates for each sphere were determined from an ROI drawn over the slice in which the sphere appeared largest. The through plane coordinate was taken as the centre of the slice. This analysis was also performed in ImageJ.

The error of each marker-thermoseed and marker-marker pair distance was calculated by subtracting the distances measured with MRI from the distances measured with CT.

4.2.3 Magnetic resonance navigation sequence implementation

The 1D non-slice-selective imaging sequence validated in the previous section was edited to incorporate propulsion gradients, thus allowing the thermoseed to be propelled using the MRI system. Further details are provided in section 4.3.3 and Figure 4.7.

4.2.3.1 MRN sequence testing

A 0.25 mm thermoseed was added to a 22 × 25 × 25 mm^3 container filled with 0.1 % (w/v) agar solution (Sigma Aldrich, USA), and the phantom was transferred to the MRI scanner. The thermoseed was navigated in a zig-zag pattern in the horizontal plane. The following propulsion parameters were used: gradient strength = 979 mT m^{-1}, duty cycle = 100/900 ms on/off (10 %), number of loops = 15 – 40, total gradient on time = 1.5 – 4 s. 2D images were acquired at regular intervals to track the movement of the thermoseed using a fast low angle shot (FLASH) sequence. Imaging parameters: TR = 0.1 s, TE = 2.5 ms, resolution = 468.8 × 234.4 μm^2, slice thickness = 0.5 mm, FOV = 60 × 30 mm^2, matrix size = 128 × 128, acqBW = 50 kHz, 1 average.

4.2.4 Ramping magnet experiments

4.2.4.1 Phantom preparation

0.51 g of insoluble, black pigment powder was mixed into 100 mL of 0.3 % (w/v) agar solution (Sigma Aldrich, USA). ~6 mL of the mixture was added to 35 mm petri dishes and left to set at room temperature, allowing the pigment to settle and create an even layer beneath the agar. Immediately prior to each experiment, a 3 mm diameter thermoseed was laid on the surface of the agar and pushed down to the bottom of the petri dish using a pipette tip.

4.2.4.2 Magnet ramping procedure

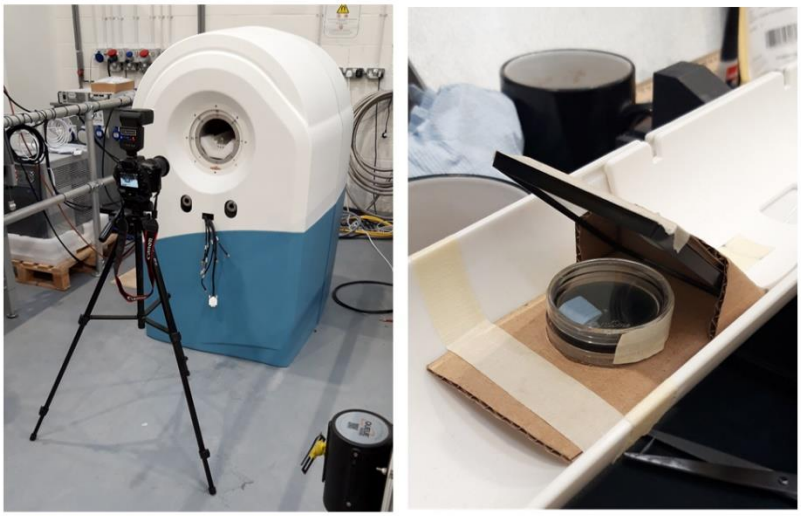

Figure 4.2 Camera set up for rampable magnet experiments. A camera was positioned a safe distance from the MRI scanner, directed along the scanner bore (left). The phantom was positioned in the scanner bore, beneath a mirror positioned 45° from horizontal (right), allowing the camera to view the phantom from above.

A phantom was positioned within the imaging volume of an MRS Magnetics 3 T 170 mm clear bore magnet (MR Solutions, UK), whilst at zero field. The magnet was then ramped up to 3 T across a period of 7 minutes, maintained at 3 T for 2 minutes and then ramped back down to zero field. A maximum field strength of 3 T was chosen, as this is the highest field strength typically used in a clinical setting. To ensure any movement could be readily detected using the phantom, the experiment was repeated with a phantom positioned approximately 13 cm from the isocentre, along the z axis, where a magnetic field gradient would be present and sufficient to cause the thermoseed to move. Photographs of the phantom were taken before and after each experiment, and a camera was positioned to look down the bore of the MRI scanner, to take photographs during the ramping process (Figure 4.2). Three replicates were performed under each set of conditions.

4.3 Results

4.3.1 Bruker vs. Tesla gradient coil performance

The performance of two imaging gradient coil inserts, manufactured by Bruker and Tesla Engineering Ltd., was assessed to infer which system should be used in the development of MINIMA. To empirically assess the performance of the two

gradient sets, the x, y and z coils were switched on and run continuously for increasing periods of time until the upper limit was reached. On the Bruker system this was assessed using the gradient simulation platform in Paravision 6.0.1 before running the actual scan. For both systems, if the gradient coils began to overheat, the scan would shut off immediately, thus indicating that the upper limit had been reached. Along all axes the Bruker coil performed better at the highest gradient strengths, with a total on time of 140 - 310 ms possible at 979 mT m^{-1} (Figure 4.3). In comparison, the Tesla coil could run for no more than 100 ms at its upper limit of 1100 mT m^{-1}. At the lower gradient strengths, the Tesla coil performed better, specifically along the y axis, which could be run continuously at 700 mT m^{-1}, compared to a maximum gradient strength of 400 mT m^{-1} on the Bruker y axis at 100 % duty cycle (Table 4.2).

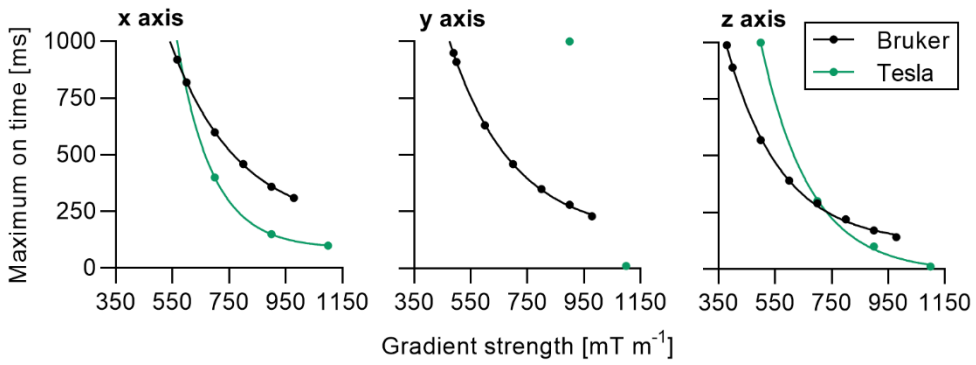

Figure 4.3 Performance comparison of Bruker and Tesla gradient coils. Maximum gradient on time for a single loop at different gradient strengths, fitted with an exponential decay.

Maximum gradient strength for continuous application [mT m^{-1}]		
Gradient axis	Bruker	Tesla
X	500	500
Y	400	700
Z	300	< 500[1]

Table 4.2 Maximum amplitude at which the gradients can be applied continuously (100 % duty cycle), along each individual axis.

[1] Z gradient coil was not tested at amplitudes below 500 mT m-1

Taken together, the data suggest that the Tesla coil performs better than the Bruker, as it can generate higher magnetic field gradients both overall and at 100 % duty cycle (1100 and 700 mT m^{-1} respectively).

4.3.2 Thermoseed imaging sequence validation

For MINIMA to be an effective minimally invasive treatment, a high level of accuracy is required in locating the thermoseed. To achieve this, MS-SET developed by Felfoul *et al.* (2008) was implemented, and a phantom was designed to measure the accuracy of the method.

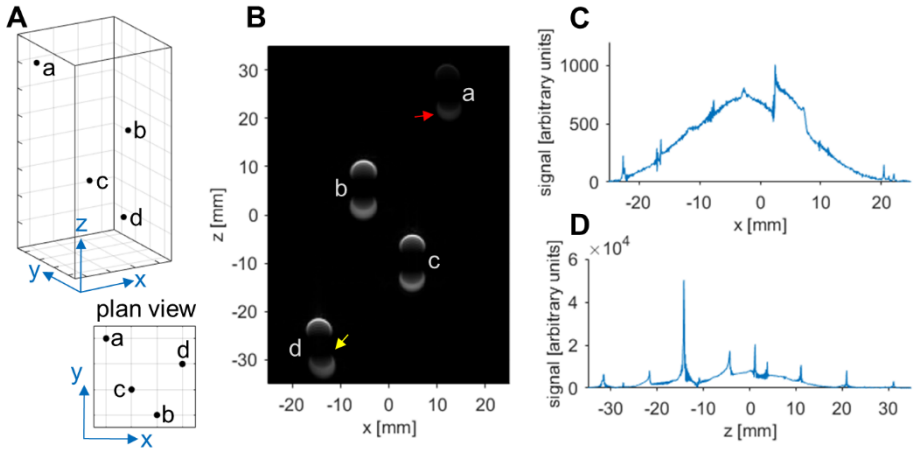

Figure 4.4 Imaging validation phantom design 1. A A schematic of the initial imaging validation phantom design, consisting of 4 × 0.5 mm diameter thermoseeds positioned within a cuboid bottle filled with 3 % agar. Each thermoseed is positioned at a unique coordinate in the x, y and z axes to ensure the magnetic signatures of each thermoseed do not overlap. **B** 2D projection image acquired in the x-z plane. **C, D** 1D projections acquired along the x and z axes respectively. B, C and D were acquired with an excitation frequency offset of + 5 kHz and excitation bandwidth of 5 kHz.

The initial phantom design consisted of four 0.5 mm diameter thermoseeds positioned with a container of agar (Figure 4.4A). The intention was to isolate the 1D projections from each thermoseed, use the projections to determine the position of each thermoseed and then calculate the distance between each thermoseed pair. These values would then be compared with 'ground-truth' values measured from CT images. There were a couple problems with this initial phantom design. First, the phantom was too large, and some of the thermoseeds were positioned outside the imaging volume of the MRI scanner, leading to a lack of signal (Figure 4.4B, red arrow) and distortions due to gradient non-linearity (Figure 4.4B, yellow arrow). Secondly, although the thermoseeds were positioned

to ensure their signature excitations did not overlap, it was extremely difficult to identify each of the individual signatures in the 1D projections (Figure 4.4C, D).

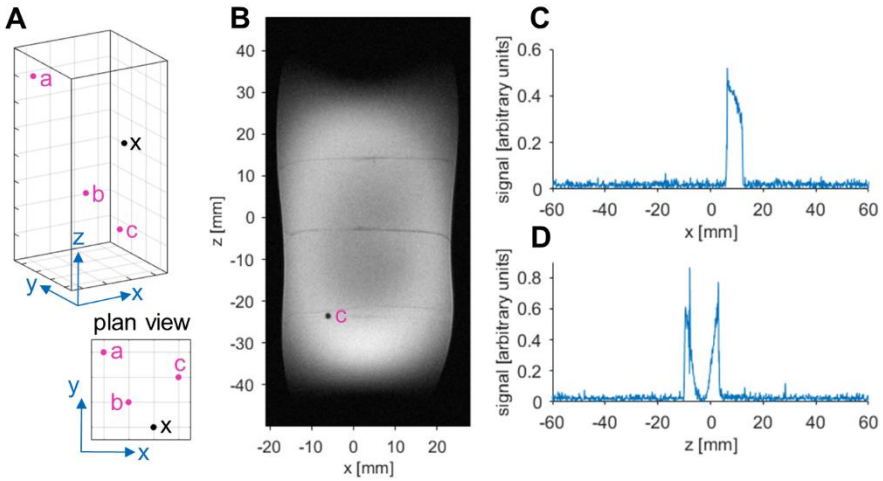

Figure 4.5 Imaging validation phantom design 2. A A schematic of the second imaging validation phantom design, consisting of 3 × 2 mm diameter spherical plastic markers and 1 × 0.5 mm diameter thermoseed positioned within a cuboid bottle filled with 3 % agar. **B** Multi-slice RARE image acquired in the x-z plane, showing the position of one of the plastic markers. **C, D** 1D projections acquired along the x and z axes respectively, acquired with an excitation frequency offset of +3 kHz and excitation bandwidth of 1 kHz.

In the second design, three of the four ferromagnetic thermoseeds were replaced with 2 mm diameter plastic spheres, acting as fiducial markers (Figure 4.5A). Unlike the ferromagnetic thermoseed, the positions of the markers could not be determined using MS-SET, as their material would not induce a local magnetic field. Instead, a multi-slice image was acquired using an FSE sequence, allowing the positions of the markers to be identified from their signal void in the agar (Figure 4.5B). Since just one thermoseed was used in this design, the single signature excitation was clearly visible in the 1D projections (Figure 4.5C, D). However, when the thermoseed-marker pair distances were calculated, they were found to differ from the distances measured using CT by up to 1 mm. Although this phantom was designed to position all markers more centrally within the phantom, it is likely that this error is due to gradient non-linearity in the periphery of the multi-slice image FOV, thus causing the positions of the markers determined from the MRI to be inaccurate. Increasing the resolution of the FSE image may also improve the accuracy of the plastic marker coordinates.

The final phantom design was very similar to that shown in Figure 4.5, but much smaller in size, to ensure that the fiducial markers were positioned within the high gradient linearity imaging volume. Ground truth distances between the thermoseed and markers were determined from CT images (Figure 4.6A) and compared with values calculated from the MR images (Figure 4.6B). The mean errors between fiducial marker pairs ranged from 0.23-0.50 mm (Figure 4.6). Distances measured between thermoseed-marker pairs had a mean error of 0.02-0.27 mm. The largest thermoseed-marker pair error was 0.38 mm. The standard deviation was less than 0.15 mm for all measurements.

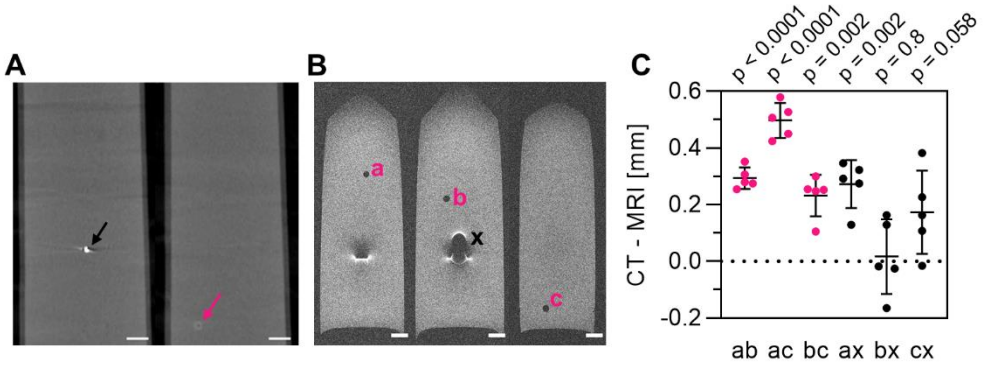

Figure 4.6 Thermoseed imaging validation. A Computed tomography (CT) image acquired for cross-validation. Black and pink arrows indicate the thermoseed and plastic markers respectively. **B** T_2-weighted magnetic resonance image acquired for fiducial marker localisation (pink letters). **C** Difference between mean CT and MRI distance replicates for each marker-marker (pink) and thermoseed-marker (black) pair (n = 5, mean ± SD). Scalebar = 5 mm.

4.3.3 Magnetic resonance navigation sequence implementation

Having validated MS-SET, the 1D pulse sequence was adapted to incorporate propulsion gradient pulses, to allow a thermoseed to be propelled using the MRI scanner hardware. The final propulsion pulse sequence consisted of a propulsion phase and an imaging phase (Figure 4.7A). During the propulsion phase the gradients are switched on to a defined gradient strength, allowed to run for a specified duration (gradient on time) and then switched off for a brief delay (gradient off time). This pulse pattern is then repeated for a defined number of periods. These four parameters (gradient strength, gradient on time, gradient off time, number of periods) can be adjusted in the Routine card in Paravision (Figure 4.7B). The direction of propulsion can also be defined as the x, y or z axis, or along any combination of the three by inputting the vector components that

combine to give a unit vector along the desired propulsion axis. Following the propulsion phase the imaging phase is completed, which involves acquiring a 1D projection along the axis of propulsion. This enables the user to easily calculate the distance moved by the thermoseed, but additional projections along the x, y and z axes may also be acquired to determine a more accurate thermoseed location.

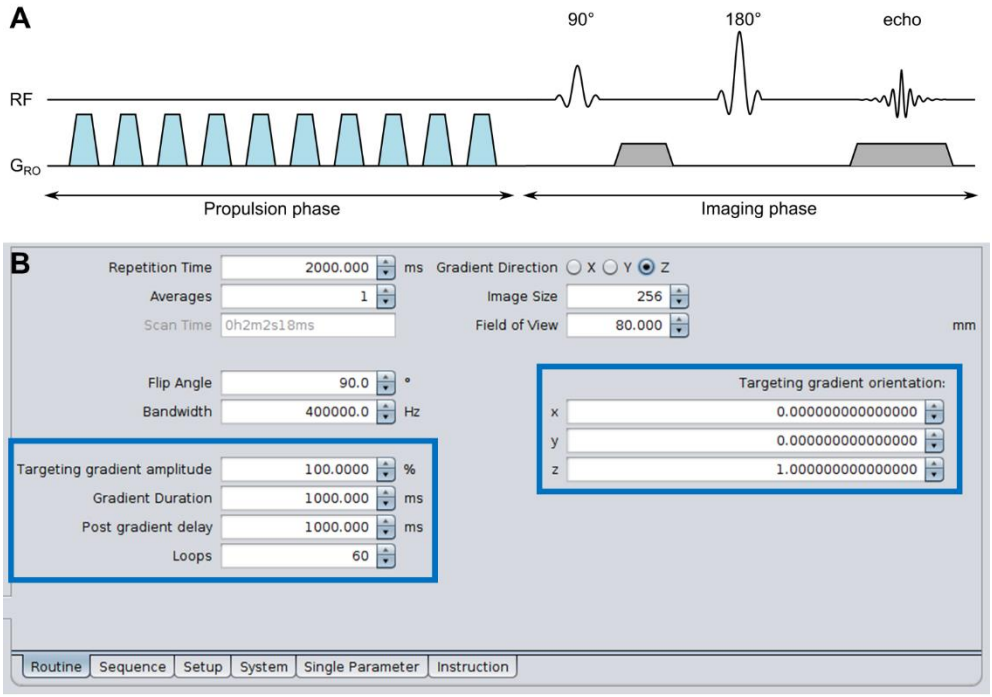

Figure 4.7 Propulsion pulse sequence. A Gradient pulses (blue) are applied rapidly in an on/off pattern along the intended axis of propulsion, thus exerting a translational force on a ferromagnetic thermoseed. A 1D spin echo is then performed along the same axis, allowing the position of the thermoseed to be tracked. **B** Propulsion parameters can be defined in the Routine Card in Paravision (blue boxes). Parameters include gradient strength (targeting gradient amplitude), gradient on time (gradient duration), gradient off time (post gradient delay) and the number of periods (Loops). The direction of propulsion is defined by entering the x, y and z vector components, which combine to give a unit vector along the intended axis of propulsion.

The propulsion sequence was tested by navigating a 0.25 mm thermoseed through a 0.1 % agar solution, along a square or zigzag path (Figure 4.8). For the square path the thermoseed was alternately navigated along the x and z axes. The path covered a total distance of 26.5 mm, with a total gradient on time of 22 s at 979 mT m^{-1}. For the zigzag path the thermoseed was propelled in the x-z plane, 45° from the x and z axes; this was achieved by setting the x and z components of the gradient orientation to 0.707 and -0.707 respectively. The path

covered 29.2 mm, with a total gradient on time of 41.1 s at 979 mT m^{-1}. These results confirmed that the propulsion pulse sequence worked and could be used in combination with MS-SET to precisely control the navigation of a thermoseed.

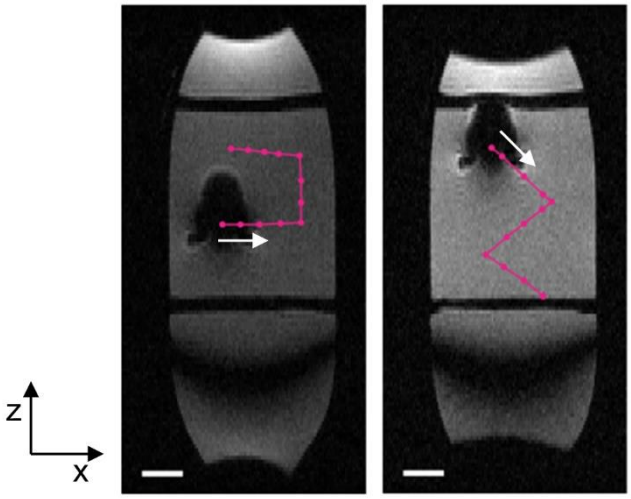

Figure 4.8 Propulsion of a 0.25 mm diameter thermoseed in agar. To assess the propulsion pulse sequence, a 0.25 mm thermoseed was propelled through a 0.1 % agar solution in a square (left) or zigzag (right) pattern. The path of the thermoseed is plotted in pink, with filled circles indicating individual movements. Direction of travel is shown with a white arrow. Scalebar = 5 mm.

4.3.4 Ramping magnet experiments

A key requirement of MINIMA is the safe insertion and removal of the thermoseed from the patient. This is particularly challenging due to the fringe field of the magnet, which has a large gradient and would exert a force on the thermoseed as the patient passes into the bore (Figure 4.1). One solution is to use a rampable magnet, which would allow the magnetic field to be adjusted in the range of 0 – 3 T within a reasonable time frame. The patient would enter the bore while the field was at 0 T, the magnet would be ramped up to the desired field for the procedure and then ramped back down to zero. In a collaboration with MR Solutions Ltd., a preclinical MRI system was ramped from zero field to 3 T and back down to assess the feasibility of this procedure. A custom-designed agar phantom was used to assess whether the ramping process would exert a force on the thermoseed, causing it to move. Through the comparison of photographs taken before and after the ramping protocol, no movement was detected in any replicates positioned within the FOV of the scanner (Figure 4.9A). The thermoseed did move in the control samples, which were purposefully positioned

outside the FOV, and a clear tract is visible in the black pigment of the phantom, thus confirming that any movement that may have occurred would have been visible with this phantom. This is also visible in camera recordings, with the thermoseed moving from the centre to the edge of the phantom after 30 s (Figure 4.9B). The time to ramp from 0 to 3 T was approximately 7.5 minutes. This result shows how a rampable MRI scanner may be used to ensure the safe insertion and removal of a thermoseed for MINIMA.

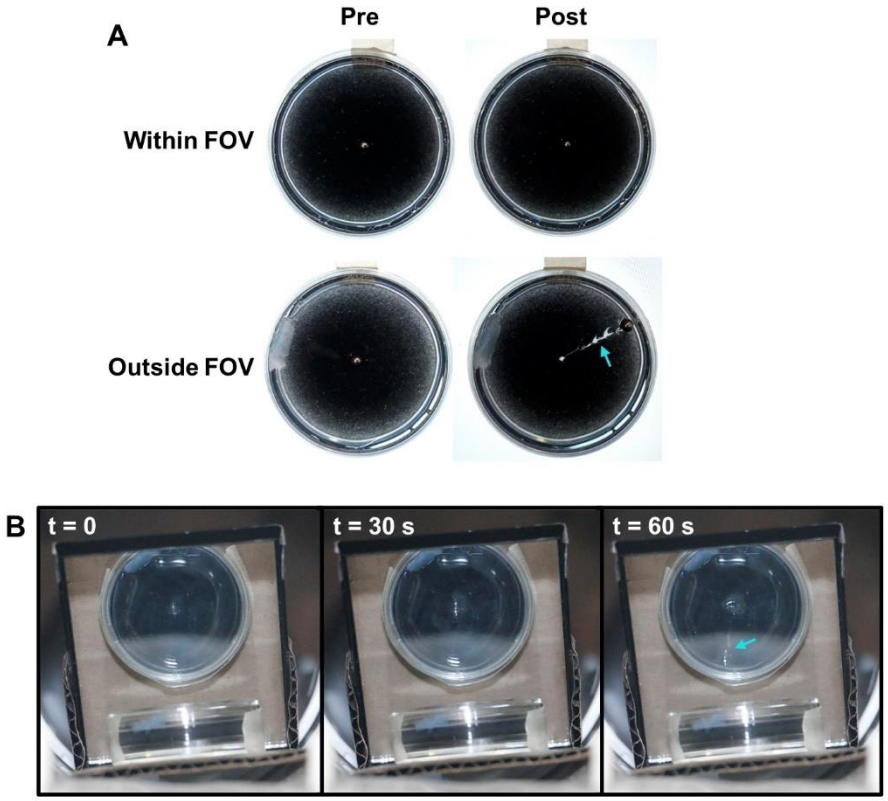

Figure 4.9 Ramping magnet experiment. A Photographs taken before and after a preclinical magnetic resonance imaging system was ramped from zero field to 3 T and back down. Samples were positioned either inside or outside of the magnet's field of view. **B** Still images taken from a recording of a phantom positioned outside the FOV, as the magnetic field was ramped up. After 60 s the thermoseed had moved to the edge of the phantom (arrow).

4.4 Discussion

A thermoseed imaging and navigation sequence was set up on a 9.4 T preclinical MRI scanner, providing a platform on which the MINIMA project could be developed. The gradient coil capability of the two MRI scanners available in the lab was assessed by ascertaining the maximum duration for which the gradients could be switched on continuously, along each axis (x, y and z) and at different

gradient strengths. The Tesla gradient insert used with the Varian Inova scanner provided larger gradient strengths along all axes (run for ≤ 100 ms) and also performed better at lower gradient strengths, with the ability to run each gradient axis indefinitely at 500 mT m^{-1} or less, and at ≤ 700 mT m^{-1} on the y axis. However, while completing these experiments some difficulties arose when using the Tesla gradient coil. Although the coil was designed to run at 1 T m^{-1} with 100 % duty cycle, due to hardware limitations of the Varian gradient amplifiers, the gradients would repeatedly cut out, thus limiting continuous gradient application to just 7 s. Therefore, to apply the gradients for > 7 s, 5 s pulses were applied in multiple loops with no delay in between, which was assumed to be equivalent to a single block pulse, as the rise time of the coil is negligible (< 20 µs). Although, this workaround allowed us to acquire some data, as presented in Figure 4.3, the unreliability of the Varian-Tesla setup would have been a limiting factor in future experiments. An additional consideration when deciding which system to take forward in the development of MINIMA was the imaging pulse sequences that were available. The Bruker system had an existing 1D sequence designed to provide a profile of the sample within the scanner, which could be used to implement MS-SET more easily than on the Varian system. Furthermore, I had recently attended a Bruker pulse programming course, which provided me with the skills to program new pulse sequences on the Bruker scanner. Therefore, considering both the hardware and software advantages offered, I decided that the Bruker system would be used throughout all remaining experiments in my PhD.

Based on MS-SET developed by Felfoul *et al.* (2008), thermoseed tracking was implemented on the Bruker system using the 1D profile imaging sequence that was available, named POSITION. Initial testing on a phantom involved offsetting the excitation pulse frequency by 3 kHz and setting a narrow excitation bandwidth of 1 kHz. This ensured that just two equipotential curves, defined by the magnetic field induced by the ferromagnetic thermoseed, were excited, as is shown in MR images in Figure 4.4. Once implemented, the accuracy of the method was assessed using a custom-designed phantom, the development of which is described in section 4.3.2. The mean error in detecting the position of the thermoseed was no more than 0.27 mm, which is comparable to other validation studies reporting errors of 0.1 – 0.3 mm (Felfoul *et al.*, 2008; Aboussouan and

Martel, 2006). This level of accuracy is considered adequate for MINIMA, as the error is smaller than the typical resolution of a clinical 2D MR image (~1.5 mm), enabling the thermoseeds position to be defined within a single voxel. In addition, the imaging can be performed in less than 1 s (Felfoul *et al.*, 2008; Felfoul *et al.*, 2009), thus allowing repeated imaging with no impact on the total procedure duration.

The 1D imaging sequence was then adapted to incorporate propulsion gradient pulses (Figure 4.7), allowing propulsion and tracking along a defined axis to be performed in a single scan. The propulsion phase of the sequence allowed a gradient to be switched on and off in a pulsed fashion. The parameters that can be defined in the sequence are the gradient strength, the on time, the off time and the number of periods. The gradient could also be applied in any direction, by applying the three orthogonal gradient coils at varying amplitudes. The sequence was subsequently tested by navigating a 0.25 mm thermoseed in a square or zigzag pattern (Figure 4.8). In both cases, the thermoseed travelled along the desired trajectory, thus demonstrating our ability to navigate the thermoseed in multiple different directions. The presented data replicate examples of navigating a ferromagnetic sphere using an MRI scanner in the literature and provide evidence that MRN can be performed on the 9.4 T Bruker system in CABI.

The possibility of using a rampable MRI scanner to ensure safe insertion and removal of the thermoseed was assessed using a preclinical MRI scanner. The magnetic field was ramped from 0 to 3 T within just 7.5 minutes, three times faster than the clinical Siemens Helicon scanner (Reichert *et al.*, 1988). A weak agar phantom containing a 2 mm ferromagnetic thermoseed was positioned in the scanner to assess whether a significant force would be exerted on the thermoseed during the ramping process. No movement of the thermoseed was observed on each of the three attempts, neither in the photographs taken throughout the process, nor when comparing the phantoms before and after. This example provides some support for incorporating a rampable MRI scanner into MRN procedures. However, this is by no means comprehensive and much more work would need to be done to ensure the safety of the patient. Furthermore, although there have been recent developments in rampable preclinical scanners,

including the DryMag system used in this work, there is little evidence of developments in the clinical arena to date.

To conclude, using the Bruker MRI system, I implemented an MR imaging and propulsion pulse sequence able to track a thermoseed to within 0.3 mm accuracy and demonstrated thermoseed navigation along an intended path. These experiments ensured the setup of the 9.4 T system, thus allowing the preclinical development of MINIMA to proceed. The next chapter builds on this by first characterising thermoseed movement through a viscous medium, whilst varying each of the propulsion parameters, and subsequently navigating a thermoseed though ex vivo tissue.

5 Navigation of ferromagnetic thermoseeds

5.1 Introduction

Having implemented a pulse sequence for navigating and tracking ferromagnetic thermoseeds on the preclinical MRI scanner in CABI, as presented in chapter 4, the next step in the development of MINIMA was to optimise the navigation for movement through tissue. Although my colleagues had previously demonstrated movement through ex vivo porcine brain tissue (Figure 5.4) as a preliminary test on the Varian system, before I started my PhD, little optimisation of the process had been performed. Therefore, I aimed to complete a series of experiments in both viscous liquids and ex vivo tissue including navigation in 3D, characterisation of different navigation parameters and navigation through ex vivo liver tissue.

The first stage of the optimisation process involved characterisation of thermoseed movement through a viscous fluid, while adjusting different propulsion parameters. As introduced in chapter 2, equation 2.8 describes how the force exerted on a thermoseed by the magnetic field gradient generated within an MRI scanner is dependent on the size of the thermoseed, it's magnetic properties (specifically M_s) and the gradient strength. It was also noted, and elaborated on in the previous chapter (section 4.3.3), that since the imaging gradients of an MRI scanner cannot typically be applied continuously, due to hardware heating, they are often applied in a pulsed fashion and described by the parameters: gradient strength, on time, off time and period duration (Figure 5.1).

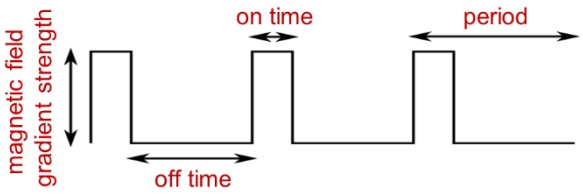

Figure 5.1 Navigation pulse sequence schematic. A magnetic field gradient is applied in a pulsed, on-off fashion. The sequence can be manipulated by changing the labelled parameters: gradient strength, on time, off time and period duration.

$$\text{duty cycle} = \frac{on\ time}{period\ duration} \tag{5.1}$$

To account for this on-off pattern, an additional term is often included in the force equation (2.9, $F_{m,z} = V_m D M_z \, \partial B_z / \partial z$) (Riegler *et al.*, 2011; Martel, 2013), termed the duty cycle (equation 5.1). Although the duty cycle value accounts for the proportion of time for which the gradient is switched on, it does not consider the specific pattern of gradient application. Consider the examples presented in Figure 5.2. In each case the total time for which the gradient is applied is equal, but the duty cycle and the pattern of gradient pulses varies. This suggests that the duty cycle alone is not sufficient in describing the effect of gradient pulsation on thermoseed movement, as equation 2.9 may suggest. The initial experiments presented in this chapter aimed to further understand the effect of each of the propulsion parameters and determine which may be most valuable in optimising thermoseed movement.

$$\text{total on time} = \text{on time} \times \text{number of periods} \tag{5.2}$$

$$\text{experiment time} = \text{period duration} \times \text{number of periods} \tag{5.3}$$

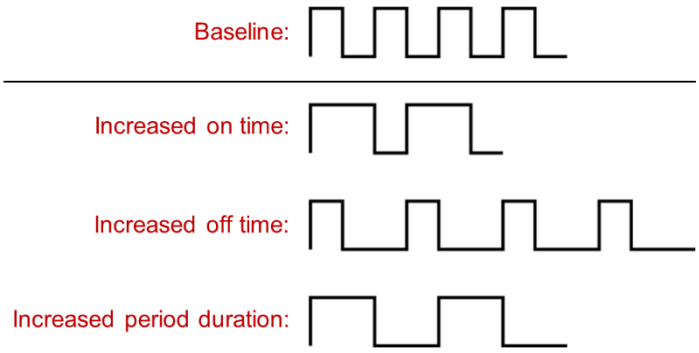

Figure 5.2 Manipulation of pulse sequence duty cycle. The duty cycle of the navigation pulse sequence can be varied by changing the on time or the off time but remains constant if both the on and off time are changed to the same extent (i.e., changing the period duration). In all the presented examples, the total time for which the gradient is applied is equal.

Having performed initial experiments in fluid phantoms, the next critical challenge for MINIMA was to assess thermoseed navigation through tissue. Although it may be possible, and in some cases easier, to navigate thermoseeds through the vasculature, certain regions within the body may not be reached with this method, due to restrictions in vessel size. Therefore, to be able to reach as many locations as possible, the ability to penetrate tissue is essential. As discussed in section 1.2.6, some attempts have been made to design tissue penetration devices

powered by MRI scanners, including the MRI-Gauss gun (Becker, Felfoul and Dupont, 2015) and magnetic hammer actuation (Leclerc *et al.*, 2018), but in both cases the devices are extremely large and may only be used to penetrate tissue from outside the body or within a large vessel.

The main challenge in achieving tissue penetration with a small device is maximising the exerted force. In a study conducted in 1990, it was suggested that 70 mN would need to be exerted on a 3 mm diameter sphere to penetrate brain tissue at 0.7 mm s^{-1} (Molloy *et al.*, 1990). This result, interpreted alongside simulated forces exerted on 1 – 4 mm thermoseeds at different gradient strengths, suggest that brain tissue penetration is not possible with gradients ≤ 1 T m^{-1} (Figure 5.3). It may also be noted that as part of the VTF project, the same group used a custom-built electromagnet to generate a 2 T m^{-1} gradient that was sufficient to navigate a 5 mm cylindrical thermoseed through dog brain tissue in vivo (Grady *et al.*, 1990).

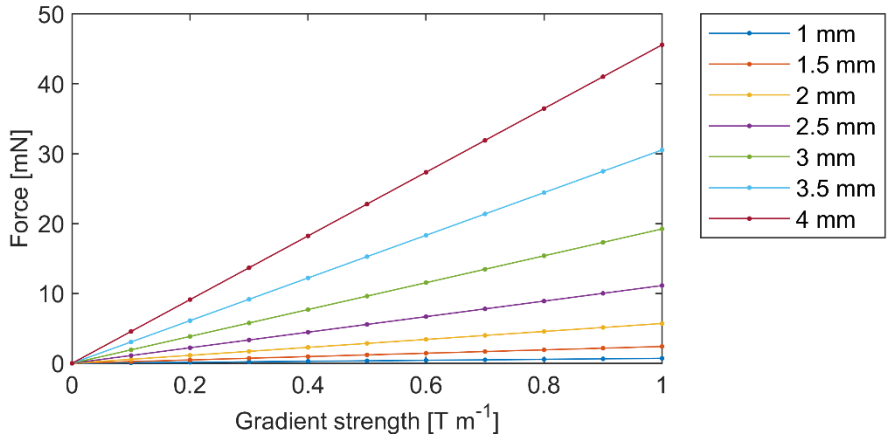

Figure 5.3 Force exerted on thermoseeds at different gradient strengths. Simulated forces calculated at different gradient strengths and for thermoseeds of different diameters using equation 2.8 ($F_{m,z} = V_m M_z \, \delta B_z / \delta z$), with M_s = 1.36 × 10^6 A m^{-1} used for M_z.

However, in spite of these supposed gradient requirements, my colleagues had previously been able to navigate both 2 and 3 mm thermoseeds through ex vivo porcine brain tissue using magnetic field gradients as low as 300 mT m^{-1} (Figure 5.4) (Baker *et al.*, 2022). The large discrepancy between the results of these two studies is likely related to the uncertainty of ± 30 mN for the reported 70 mN value, which the authors explain is due to inaccuracy of the measurement system (Molloy *et al.*, 1990). Furthermore, the 70 mN force specifically relates to

movement at a speed of 0.7 mm s^{-1}. Of the examples presented in Figure 5.4, the thermoseed moved fastest in sample D, travelling 53 mm in 8 minutes, which equates to 0.1 mm s^{-1}, 7 times less than the example in the dog brain. This proof of concept data demonstrating navigation of a thermoseed through brain tissue using an MRI scanner, is promising and provides assurance that MINIMA has the potential to be applied in the brain.

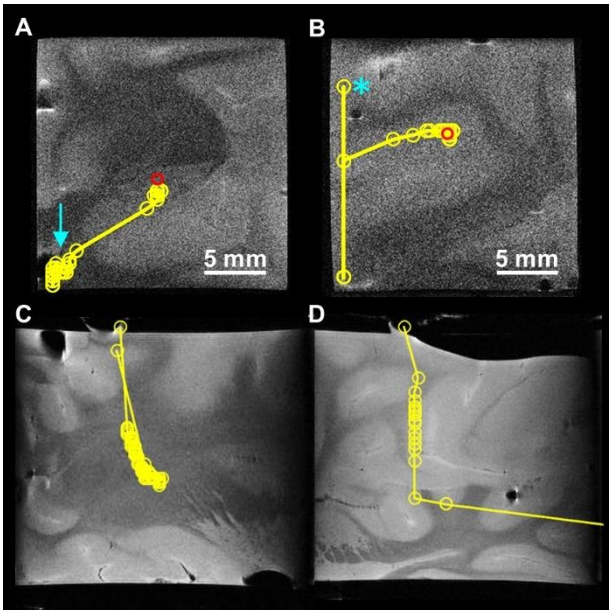

Figure 5.4 Thermoseed movement through brain tissue. A, B Navigation demonstrated through ex vivo, porcine brain tissue samples using a 2 mm thermoseed, overlaid onto pre-acquired T_2-weighted MR images (gradient strength = 300 – 500 mT m^{-1}, duty cycle = 20/70 ms on/off, number of periods = 500 – 5000). **C, D** Navigation through ex vivo brain tissue using a 3 mm thermoseed and a clinically relevant magnetic field gradient strength of 300 mT m^{-1} (duty cycle = 1.0). The thermoseed was navigated 45 mm and 53 mm in C and D, respectively. Image adapted from Baker *et al.* (2022).

Although MINIMA may be useful in treating cancer in the brain, an advantage of the technique would be its ability to be applied across different organs and diseases. Therefore, the next logical step in the development of the project was to assess navigation through different tissues. Since brain tissue is one of the softest in the body, other tissues would indeed be more challenging. However, with access to gradient coils capable of generating magnetic field gradients up to 1 T m^{-1}, I hypothesised that this would be possible, and attempts at navigating a 3 mm thermoseed through ex vivo liver tissue were performed. In this instance, liver tissue was chosen, as it is readily available, is stiffer than brain tissue, thus

providing more of a challenge, and it is an organ in which thermal ablation therapies are often used to treat liver metastasis (Takahashi and Berber, 2020).

To summarise, the aims of the experiments presented in this chapter are:

1. To demonstrate thermoseed movement in 3D
2. To investigate the effect of different propulsion parameters on thermoseed movement through a viscous medium
3. To attempt thermoseed movement through ex vivo liver tissue

5.2 Methods

A Bruker 9.4 T Biospec 94/20 preclinical MRI system was used for all experiments presented in this chapter. Unless otherwise indicated, the shielded imaging gradient set that was tested in the previous chapter and can generate a magnetic field gradient of 979 mT m^{-1} was also used.

5.2.1 Phantom designs

A variety of containers were used as phantoms for the navigation experiments presented in this chapter. The most basic consisted of a rectangular plastic box, which could be filled with the desired medium, before adding a thermoseed and sealing the lid. An example of this is presented in Figure 5.5A. To be able to use the MS-SET tracking method implemented in chapter 4, the thermoseed would be navigated to the centre of the sample before beginning the experiment, to ensure the entirety of the unique magnetic signature was enclosed within the signal-generating region of the phantom (i.e., the magnetic signature did not exceed the edge of the box).

In some cases, such as when moving through ex vivo tissue, this approach was not suitable. Therefore, a phantom was designed which consisted of two compartments (Figure 5.5B and C). Both compartments would be filled with a water-based material, providing signal across the container, however, the thermoseed would be limited to the centre compartment, thus ensuring that the entirety of the magnetic signature could be imaged and MS-SET could be performed as soon as the sample was inserted into the scanner.

5.2.2 Navigation in 3D

A 0.25 % or 0.35 % (w/v) agar solution was prepared by adding agar (Sigma Aldrich, USA) to distilled water in the required weight/volume ratio and heating the solution until boiling. The solution was then added to a 74 × 21 × 21 mm^3 container to set at room temperature. Once set, a 1 mm (0.25 % agar) or 2 mm (0.35 % agar) diameter thermoseed was added to the agar-filled container. Using a Bruker imaging gradient coil capable of generating a magnetic field gradient of up to 452 mT m^{-1}, the thermoseed was navigated along a 3D path. A range of navigation parameters were used throughout the experiments: gradient strength = 252 – 451 mT m^{-1}, duty cycle = 0.22 – 1.00, number of periods = 1 – 30000, total on time = 1 – 80 s. The displacement of the thermoseed was measured by cross-correlating 1D projections acquired before and after each movement (as per the method described in chapter 4). Imaging parameters: TR = 2 s, FOV = 80 mm, matrix size = 256, resolution = 312.5 µm, acqBW = 44.643/300 kHz (1/2 mm thermoseed), 1 average, excOffset = 10/45 kHz (1/2 mm thermoseed), excBW = 4/10 kHz (1/2 mm thermoseed).

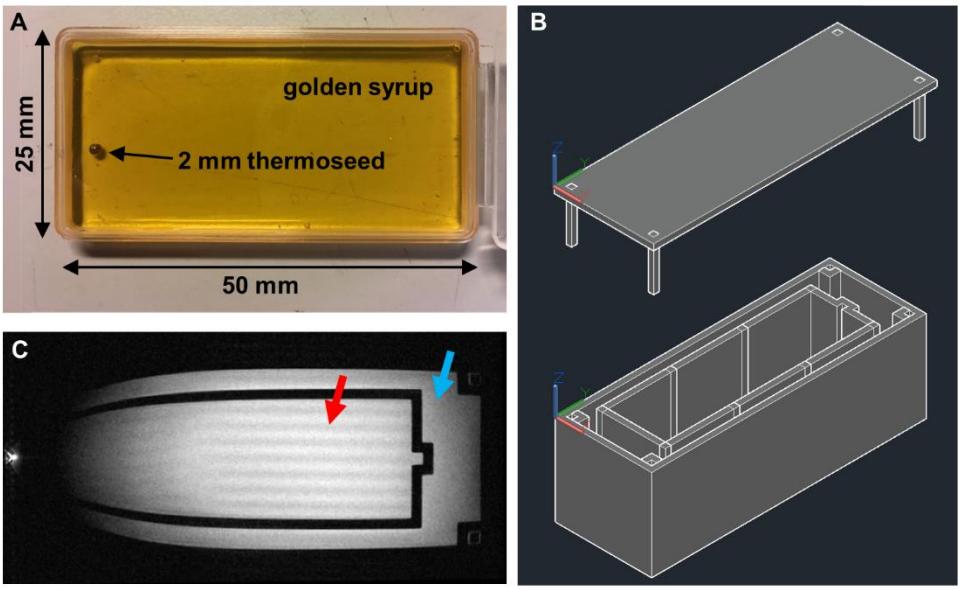

Figure 5.5 Phantom designs for navigation experiments. A A simple rectangular box filled with golden syrup, used for initial thermoseed movement characterisation experiments. **B** 3D rendering of a phantom designed with two compartments. **C** MR image of the phantom in B 3D printed and filled with agar. The thermoseed movement would be limited to the inner compartment (red arrow). The outer compartment (blue arrow) provides signal on the image, so that the full magnetic signature of the thermoseed could be detected, allowing the thermoseed's position and movement to be measured accurately.

5.2.3 Characterisation of navigation parameters

A 25 × 50 mm^2 plastic box was filled with golden syrup (Tate and Lyle PLC, UK) to a depth of approximately 5 mm. A thermoseed (0.5, 1, 2 or 3 mm diameter) was added and the box sealed (Figure 5.5A). Once the phantom was inserted into the scanner bore, the thermoseed was first navigated to the centre of the box by applying the magnetic field gradients along the x and z axes. Once at the centre, the thermoseed was moved forwards and backwards along the x axis with 3 repetitions recorded in each direction. For all experiments a total on time of 4 s was used. Gradient strength, off time and period duration were systematically varied in turn. Full details of the navigation parameters used are provided in Table 5.2. The displacement of the thermoseed was measured by cross-correlating 1D projections acquired before and after each movement. Imaging parameters: TR = 2 s, FOV = 60 mm, matrix size = 512, resolution = 117.2 µm, acqBW = 200/300 kHz. Other imaging parameters were optimised for sphere size (Table 5.1).

Thermoseed diameter [mm]	Excitation frequency offset [kHz]	Excitation bandwidth [kHz]	Number of averages
0.5	5	6	8
1.0	5	6	8
2.0	10	10/18[2]	1
3.0	30	36	1

Table 5.1 Imaging parameters used for characterisation experiments. Parameters were optimised for thermoseed size

5.2.4 Navigation in ex vivo tissue

Sections of lamb liver were cut into 20 × 10 × 14 mm^3 pieces, stored at 37 °C in PBS for 1 hour and added to the inner compartment of a 3D printed phantom (Figure 5.5B, C). The outer compartment was filled with 2 % (w/v) agar solution. Navigation was performed using two different imaging gradient coils, capable of producing gradients of up to 447 and 979 mT m^{-1}; two attempts were made with each setup.

Before the thermoseed was added to the sample, a pre-image was acquired using a fast spin echo pulse sequence. Imaging parameters for samples A and B (using 447 mT m^{-1} gradients): TR = 2 s, effective TE = 19.9 ms, FOV = 80 × 40

[2] An excitation bandwidth of 18 kHz was used for the duty cycle period experiment.

mm^2, matrix size = 512 × 256, resolution = 156.3 × 156.3 μm^2, slice thickness = 1 mm, number of slices = 21, acqBW = 300 kHz, 1 average, total scan time = 1 min 4 s. Imaging parameters for samples C and D (using 979 mT m^{-1} gradients): TR = 2 s, effective TE = 18.8 ms, FOV = 60 × 30 mm^2, matrix size = 512 × 256, resolution = 117.2 × 117.2 μm^2, slice thickness = 1 mm, number of slices = 23, acqBW = 300 kHz, 1 average, total scan time = 1 min 4 s.

A 3 mm thermoseed was subsequently added to the inner compartment of the phantom and navigated through the liver tissue. A range of navigation parameters were used throughout the experiments. For samples A and B: gradient strength = 250 – 447 mT m^{-1}, duty cycle = 0.33 – 1.00, number of periods = 1 – 500, total on time = 3.5 – 400 s. For samples C and D: gradient strength = 350 – 979 mT m^{-1}, duty cycle = 0.1 – 1.0, number of periods = 1 – 10000, total on time = 7 – 450 s.

The displacement of the thermoseed was measured by cross-correlating 1D projections acquired before and after each movement (as per the MS-SET method described in chapter 4). Imaging parameters for samples A and B: TR = 2 s, FOV = 80 mm, matrix size = 1024, resolution = 78.1 µm, acqBW = 455 kHz, 1 average, excOffset = 45 kHz, excBW = 10 kHz. Imaging parameters for samples C and D: TR = 2 s, FOV = 60 mm, matrix size = 512, resolution = 117.2 µm, acqBW = 455 kHz, 1 average, excOffset = 45 kHz, excBW = 10 kHz.

.

Parameter	Gradient strength [mT m^{-1}]	On time [ms]	Off time [ms]	Period duration [ms]	Duty cycle	Number of periods	Total on time [s]	Experiment time [s]
Number of periods	500	2	7	9	0.22	250: 250: 2000	0.5: 0.5: 4.0	2.25: 2.25: 18
Gradient strength	50: 50: 500	2	7	9	0.22	2000	4	18
Period duration	500	2	7	9	0.22	2000	4	18
		4	14	18		1000		
		8	28	36		500		
		20	70	90		200		
		40	140	180		100		
		100	350	450		40		
		200	700	900		20		
		500	1750	2250		8		
		1000	3500	4500		4		
		2000	7000	9000		2		
		4000	14000	18000		1		

Table 5.2 Navigation parameters used for movement characterisation experiments. (Correspond to figures 5.8 and 5.9, x: i: y indicates values from x to y in intervals equal to i).

Parameter	Gradient strength [mT m^{-1}]	On time [ms]	Off time [ms]	Period duration [ms]	Duty cycle	Number of periods	Total on time [s]	Experiment time [s]
Off time	500	2	0	2	1.00	2000	4	4
			1	3	0.67			6
			2	4	0.50			8
			3	5	0.40			10
			4	6	0.33			12
			5	7	0.29			14
			6	8	0.25			16
			7	9	0.22			18
			8	10	0.20			20
			10	18	0.11			36
			32	34	0.06			68
Gradient strength (up to 1 T m^{-1})	100: 100: 1000	2	7	9	0.22	2000	4	18

Table 5.2 continued. Navigation parameters used for movement characterisation experiments continued. (Correspond to figures 5.8 and 5.9, x: i: y indicates values from x to y in intervals equal to i).

5.3 Results

5.3.1 Navigation in 3D

In the previous chapter, the imaging and navigation pulse sequence was initially tested by navigating a 0.25 mm thermoseed along a simple 2D path (section 4.3.3). The next step was to ensure the thermoseed could be moved in 3D. Since the imaging gradient coils of the MRI scanner can generate magnetic field gradients along 3 orthogonal axes, there should be no issue with moving the thermoseed in any chosen direction. The only additional factor that must be considered is gravity, which would provide additional resistance to the thermoseed moving vertically up.

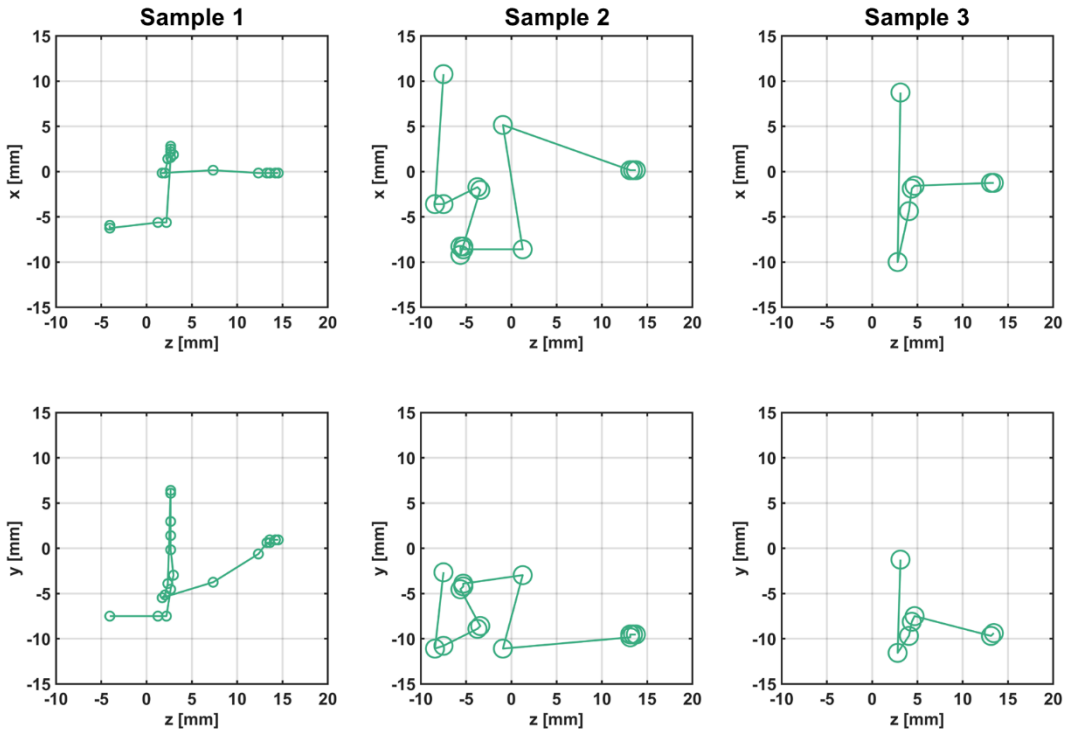

Figure 5.6 Navigation in 3D. 1 mm (sample 1) and 2 mm (samples 2 and 3) thermoseeds were navigated along a 3D path in 0.25 and 0.35 % agar, respectively. x and z axes are in the horizontal plane, and y is the vertical axis.

Figure 5.6 shows three examples of a thermoseed being navigated along a 3D path. Unfortunately, due to the composition of the agar, the thermoseed was not well supported and would begin to drop down within the sample when no upwards gradient was applied. Nonetheless, this data demonstrates movement along all three axes. This is essential for MINIMA, to ensure that the thermoseed can follow a path to any target, whilst avoiding critical and delicate structures.

5.3.2 Characterisation of navigation parameters

Having demonstrated movement of a thermoseed in 3D using the magnetic field gradients generated by an MRI scanner, the next stage of development was to optimise the process. Therefore, experiments were performed to investigate the effect of different navigation parameters (number of periods, gradient strength, period duration and off time) on the movement of thermoseeds of varying size. These experiments were performed in golden syrup, a purely viscous fluid, and the movement was measured using the validated MS-SET method. Example projections showing two consecutive movements of a 3 mm thermoseed following continuous application of a 500 mT m^{-1} magnetic field gradient for 4 s are presented in Figure 5.7.

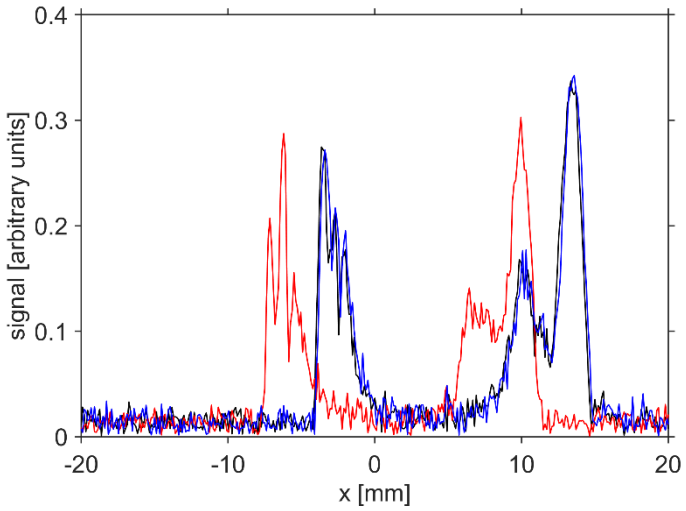

Figure 5.7 1D projections showing thermoseed movement. A 3 mm thermoseed was moved from its starting position (blue), – 3.5 mm (red) along the x axis and back (black) in two separate movements. This data is taken from the gradient duty cycle off time experiments, with an off time of 0 ms and duty cycle of 1.0.

Displacement was observed to have a positive linear relationship with the number of periods, with 500 additional repetitions (an additional 1 s of gradient application) increasing displacement by 0.65 mm (R^2 = 0.90, r < 0.0001, Figure 5.8A). Furthermore, a positive linear relationship was observed between displacement and gradient strength for 1, 2 and 3 mm thermoseeds ($R^2 \geq 0.50$, r < 0.0001, Figure 5.8B). A slight positive correlation was observed between displacement and period duration (Figure 5.8C). Although, the slope was very small, and a period duration of 18 s provided just 0.4 mm greater displacement

than a period of 9 ms, this data does suggest that if hardware allows, applying the gradient for longer periods of time is beneficial over lots of shorter pulses. Finally, increasing the off time caused a decrease in displacement (Figure 5.8D). The greatest displacement observed throughout the experiments in this section was 3.5 mm and was achieved using a 3 mm thermoseed and a 500 mT m^{-1} gradient applied continuously for 4 s. This equates to an approximate speed of 0.9 mm s^{-1}. Throughout all experiments, a larger thermoseed size had a marked effect on the distance moved, with the displacement of a 3 mm thermoseed up to 6 times larger than a 1 mm thermoseed.

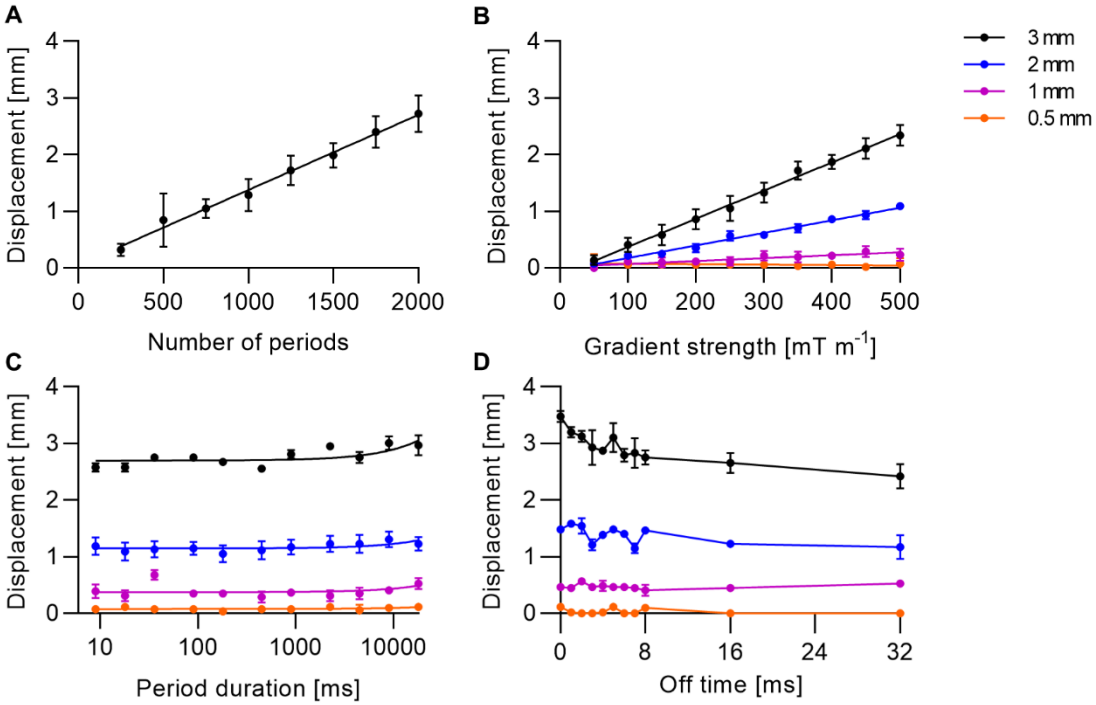

Figure 5.8 Effect of navigation pulse sequence parameters on thermoseed movement. 0.5 – 3 mm thermoseeds were navigated through a viscous medium to assess the effect of different navigation parameters. Displacement was linearly dependent on the number of periods (**A**, n = 4, $p < 0.0001$), gradient strength (**B**, n = 6, $p < 0.0001$ for 1 – 3 mm thermoseeds) and period duration (**C**, n = 6, $p < 0.05$ for 1 – 3 mm thermoseeds). **D** A shorter time also led to an increase in displacement. Full linear regression data for A – C is presented in Table 5.3.

Parameter	Thermoseed diameter [mm]	Slope	Intercept [mm]	R^2	p
Number of periods	3.0	1.3×10^{-3}	0.05	0.90	< 0.0001
Gradient strength	0.5	-8.3×10^{-5}	0.08	0.03	0.21
	1.0	5.2×10^{-4}	0.02	0.50	< 0.0001
	2.0	2.2×10^{-3}	-0.05	0.96	< 0.0001
	3.0	5.0×10^{-3}	-0.13	0.95	<0.0001
Period duration	0.5	2.0×10^{-6}	0.08	0.04	0.13
	1.0	6.4×10^{-6}	0.38	0.07	0.04
	2.0	8.1×10^{-6}	1.15	0.08	0.02
	3.0	2.0×10^{-5}	2.70	0.37	< 0.0001

Table 5.3 Linear regression analysis for data presented in Figure 5.8.

For the final characterisation experiment, the displacement of a 3 mm thermoseed was measured when applying gradients of different strengths, up to 1 T m^{-1} (Figure 5.9). As with the previously reported data, a linear relationship was observed and the linear regression analysis gave a similar slope (5.0×10^{-3} mm mT^{-1} vs. 5.3×10^{-3} mm mT^{-1}, Table 5.4).

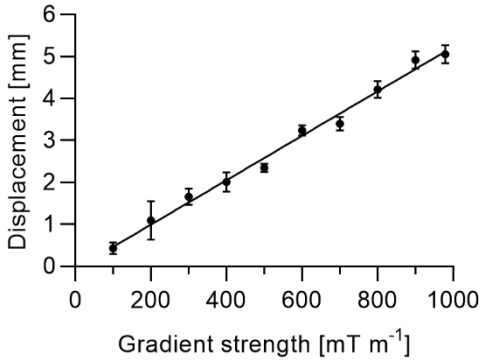

Figure 5.9 Effect of gradient strength on thermoseed movement up to 1 T m^{-1}. A 3 mm thermoseed was navigated through a viscous medium. Displacement was linearly dependent on gradient strength. n = 6, p < 0.0001. Full linear regression data is presented in Table 5.4.

Thermoseed diameter [mm]	Slope [mm mT^{-1}]	Intercept [°C]	R^2	p
3.0	5.3×10^{-3}	-0.06	0.97	< 0.0001

Table 5.4 Linear regression analysis for data presented in Figure 5.9.

5.3.3 Navigation in ex vivo tissue

Having investigated the effect of each of the propulsion parameters on thermoseed movement, attempts were made to navigate a thermoseed through ex vivo liver tissue. Since liver tissue is denser than brain tissue, it was expected that larger gradient strengths and/or duty cycles would be required to achieve sufficient thermoseed movement. A total of four attempts were made using a 3 mm thermoseed. In the first two samples (Figure 5.10A, B) a gradient coil capable of generating 447 mT m^{-1} was used, providing a greater imaging volume at cost to the gradient strength. The thermoseed was navigated a total of 2.8 and 2.5 mm along the z axis in samples A and B respectively, with each experiment taking approximately 55 minutes. As can be seen in Figure 5.10A and B, the path taken by the thermoseed was not straight, although the gradient was applied directly along the z axis. This is most likely due to the structure of the tissue and the thermoseed taking the path of least resistance.

In the final two samples, an imaging coil capable of generating a stronger magnetic field gradient was used (979 mT m^{-1}), in an attempt the navigate the thermoseed over a greater distance. In total the thermoseed was navigated 3.4 and 1.3 mm along the z axis in samples C and D, with each experiment taking 3 and 4 hours respectively. Unlike samples A and B, the thermoseed consistently travelled in the intended direction. This result would suggest that it is not possible for a 3 mm thermoseed to penetrate tissue at a rate that would be required to deliver therapy within a reasonable time frame. Further discussion on how this could be improved is provided in the next section.

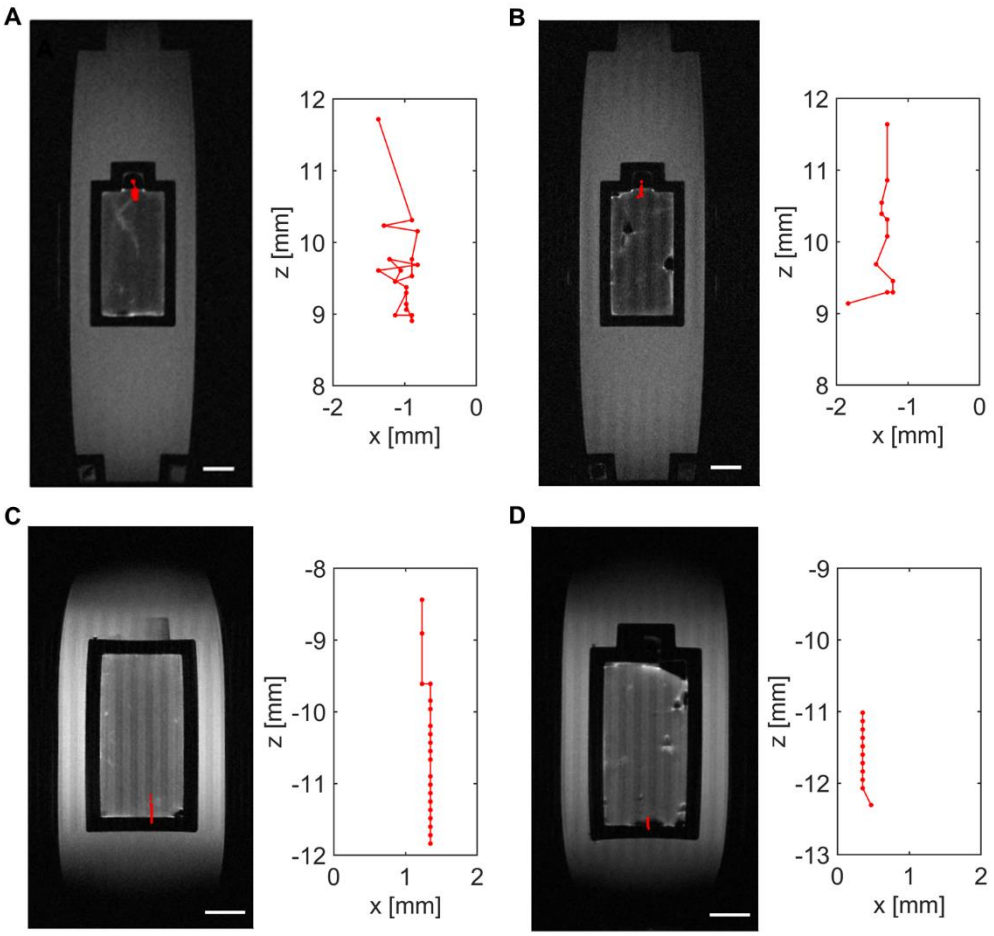

Figure 5.10 Thermoseed navigation through ex vivo liver tissue. A 3 mm thermoseed was navigate through ex vivo liver tissue using magnetic field gradients up to 447 mT m^{-1} (A, B) and 979 mT m^{-1} (C, D). LHS images show thermoseed path overlaid onto MR image of the tissue placed in the 3D printed, 2 compartment phantom, scale bar = 5 mm. RHS images show the path of the thermoseed zoomed in, each red point represents an individual movement.

5.4 Discussion

In this study, a series of experiments were performed to characterise and optimise thermoseed movement. Initially, navigation was performed along a 3D path through an agar solution, demonstrating that thermoseed movement is possible in any direction. Next, propulsion parameters were investigated one at a time, to assess the effect that each parameter has on thermoseed movement. Finally, following on from experiments performed in brain tissue, attempts were made to navigate a thermoseed through ex vivo liver tissue.

The movement of a ferromagnetic thermoseed was measured whilst incrementally changing individual propulsion parameters, to characterise the effect of each parameter on thermoseed movement. Gradient strength and

thermoseed size were found to have the greatest effect, in accordance with the relationship described in equation 2.8, alongside the number of periods, which was also expected, as this simply increases the duration for which the gradient is applied. When increasing the off time (the interval between gradient pulses), thermoseed displacement decreased, despite the total on time remaining constant. This observation may be explained by the momentum of the thermoseed being lost during the 'off' interval. While the gradient is switched on the thermoseed builds momentum but as soon as the gradient is switched off this momentum decays; as the off time increases there is a longer interval in which the thermoseed can lose its momentum, thus resulting in a shorter displacement. Finally, a very small increase in displacement was observed when the duty cycle period was increased 2000-fold (9 – 18000 ms). Although this is insignificant for the distances covered in this experiment, it may be useful to bear this effect in mind when optimising movement through tissue. These initial experiments were performed in golden syrup, as it is a Newtonian fluid with a high viscosity, thus providing the simplest possible model. Although this is unrealistic compared with movement through tissue, the results provide an indication of the parameters to consider when optimising navigation through more complex samples and perhaps in designing bespoke propulsion gradient coils.

Having characterised movement through a liquid, attempts were then made to navigate a thermoseed through ex vivo liver tissue. Although these were the first known attempts at navigating an individual ferromagnetic thermoseed through tissue other than the brain, the results were, unfortunately, limited. The greatest distance moved in a single sample was just 3.4 mm. This result was disappointing, especially as previous work showed successful thermoseed navigation through ex vivo brain tissue (Figure 5.4). There may be several reasons for this. First, the experimental set up was not optimal. Due to the small imaging volume of the preclinical MRI scanner, and the need for the thermoseed to be central within the sample for the MS-SET tracking method to be used accurately (see sections 4.3.2 and 5.2.1), only very small tissue samples could be used in these experiments. When cutting the samples to this size and fitting them into the containers, the structural properties of the tissue were likely to be different to those within the body. Future studies should be performed on alternative MRI scanners designed for imaging larger animals or humans, which

would allow larger tissue pieces, or preferably entire organs, to be used, thus retaining the structural properties and integrity of the tissue as much as possible. However, even if larger tissue samples were used there would still be differences between the in vivo and ex vivo tissues, which would affect thermoseed movement. One factor is the temperature of the tissue, with the ex vivo liver experiments conducted at room temperature (~20 °C) rather than body temperature (37 °C). Furthermore, the in vivo tissue would be more hydrated. Although the liver samples were soaked in PBS for 1 hour prior to experiments in order to rehydrate them as much as possible, the tissue is still likely to have been dehydrated compared to live tissue, due to a lack of blood and interstitial fluid, which may aid thermoseed movement in vivo.

Another reason for the limited thermoseed movement could simply be that the force exerted on the thermoseed was not sufficient to penetrate liver tissue. There are two possible ways this force could be increased, first is through optimisation of the thermoseed shape and size and second is to increase the gradient strength. To increase the gradient strength above 1 T m^{-1} on a preclinical system would require development of a specialist gradient coil. A more practical option for testing thermoseed movement at higher gradient strengths might be to design a bench top electromagnet that can generate a uniaxial magnetic field gradient, such as the one used by Leclerc *et al.* (2018). This setup would allow further experiments to be performed without having to conform to the safety restrictions necessitated by the MRI scanner and at a lower cost. If efficient movement was successfully demonstrated with this set up, then the development of equivalent MR-compatible gradients may proceed. Regarding thermoseed optimisation, the most effective option to increase the propulsion force is to increase the size of the thermoseed. In this study, the size of the thermoseed was limited to 3 mm diameter, due to the small imaging volume of the preclinical scanner. The imaging volume of a clinical MRI scanner would remove this restriction, potentially allowing larger thermoseeds to be used. However, larger thermoseeds may not be appropriate for certain applications and would likely cause more damage when navigated through healthy tissues. Consequently, the need to increase thermoseed size may impact clinical translation. Another property of the thermoseed to consider is the material. Although chrome steel has a high magnetic saturation point, there are a few metal alloys that have higher values,

such as Permendur, an iron-cobalt alloy with M_S = 1.9 × 10^{-6} A m^{-1} (Gosselin, Lalande and Martel, 2011) (40 % higher than chrome steel). Finally, changing the shape of the thermoseed may reduce the force required to penetrate tissue, for example if the seed was elongated like a grain of rice. However, this would raise other challenges, since the long axis of the thermoseed would align with the main magnetic field, thus restricting its range of motion in the x-y plane.

Although our previous work has successfully demonstrated thermoseed navigation through ex vivo brain tissue, this was performed at a rate of no more than 0.1 mm s^{-1} (Baker *et al.*, 2022), allowing a distance of 10 cm to be traversed in 15 minutes. This speed could be improved in a number of ways. First, the thermoseed could be adapted, as described above, to increase the translational force, which would lead to greater navigation speeds. Other ways to improve the speed of movement would be the adjust the navigation parameters. Based on the results presented in Figure 5.8, increasing the gradient strength as much as possible and the duty cycle to 100 % would have the greatest impact. However, to achieve these specifications, on either a preclinical or clinical system, would require further developments to the gradient coils currently available for MRI scanners.

For MINIMA to be an effective minimally invasive therapy, it is essential that the thermoseed can be moved with a high degree of control and precision. The initial data presented in this study demonstrates that this is possible in viscous liquids, since submillimetre distances were navigated and measured using the MS-SET method. Although the initial aim of MINIMA was to develop a therapy that could be used to treat cancers across different organs, this now seems unlikely when considering the ex vivo data presented in this chapter. However, MINIMA could still be effective in the brain, with the possibility of treating not only brain cancers, but potentially other diseases that are treated using open surgery, such as epilepsy. In each case, having navigated the thermoseed through the brain to the target under image-guidance, the therapy would be delivered in the form of thermal ablation. Heating of the thermoseed to deliver a thermal therapy is the final of the three key components of the MINIMA project and forms the basis of the next two chapters of this thesis.

6 Characterisation of thermoseed heating

6.1 Introduction

Chapters 4 and 5 have demonstrated the ability to image and navigate a ferromagnetic thermoseed using an MRI scanner with a high degree of precision. It is therefore possible to envisage how magnetic resonance navigation may be used as a minimally invasive tool to diagnose and treat different diseases by adapting the device for sensing or surgical applications, or to deliver a therapeutic drug. One possible application is hyperthermia or thermal ablation, which may be delivered remotely, using an AMF to heat the thermoseed.

As discussed in section 1.4, heating therapies can be separated into two categories based on the temperature rise that is induced in the tissue. Heating between 41 and 45 °C is termed hyperthermia and above 45 °C is considered thermal ablation. Typically, for hyperthermia to be effective, the modest temperature increase must be maintained for a prolonged period of time and delivered through a repeated number of treatments. Each treatment is often described in terms of thermal dose (TD), which has the units of cumulative equivalent minutes at 43 °C (CEM_{43}). TD can be calculated from the temperature achieved and the exposure time (Mouratidis, Rivens and ter Haar, 2015):

$$TD = CEM_{43} = \sum_{t=0}^{t=final} R^{(43-\bar{T})}\Delta t \qquad (6.1)$$

where $\bar{T}$ is the average temperature during time Δt and R = 0.25 for temperatures < 43 °C and 0.5 for temperatures > 43 °C; a clinical dose is considered to be 240 minutes. Although CEM_{43} has some limitations as a thermal dose parameter, especially when hyperthermia is applied as an adjuvant to radiotherapy, these limitations are less relevant when ablating at higher temperatures (van Rhoon, 2016). Most thermal ablation therapies, including HIFU, aim to reach temperatures > 60 °C, as this will induce cell death within less than 1 s (Zhou, 2011). Since the MINIMA concept involves using a single thermoseed to heat at multiple locations, it is important for thermoseed heating to be rapid, thus ensuring the entire procedure can be performed within a reasonable time frame.

A target temperature of 70 °C is therefore used in the experiments presented in this chapter.

To improve thermoseed heating and ensure 70 °C is reached, larger field amplitudes and frequencies can be used, as described in equation 2.11. However, other factors must also be considered and place limitations on the parameters that can be used. For example, frequencies < 50 kHz and > 2 MHz should not be used to avoid skeletal muscle stimulation and to ensure sufficient penetration depth respectively (Pollert and Zaveta, 2012). Non-specific eddy current heating is another consequence of AMF application, and the Brezovich criterion, which limits $H \cdot f$ to 4.85 × 10^8 A m^{-1} s^{-1}, is often employed to inhibit the onset of such effects (Atkinson, Brezovich and Chakraborty, 1984). However, since the Brezovich criterion is applicable to heating across the whole body, a higher limit, up to 5 × 10^9 A m^{-1} s^{-1} is appropriate when treating smaller regions such as the head (Hergt and Dutz, 2007). Furthermore, clinical trials performed in the brain showed that field strengths up to 13.5 kA m^{-1} at 100 kHz were well tolerated by patients (Maier-Hauff *et al.*, 2007). Considering these limitations and examples from the literature, I hypothesised that sufficient temperatures could be obtained with the chrome steel thermoseeds used in previous chapters, when heated using a custom-built MR-compatible heating coil.

In this study, the heating of ferromagnetic thermoseeds was characterised to investigate this hypothesis. Initial experiments involved heating thermoseeds of different sizes in air, using a bespoke MR-compatible heating device to determine the maximum temperatures that could be attained and the time taken to reach the target temperature of 70 °C. Next, experiments were performed under more biologically relevant conditions, including in water and ex vivo liver tissue. Finally, the distribution of heat surrounding the thermoseed was measured in tissue, using a fibre optic temperature probe positioned at a range of distances from the thermoseed's surface.

To summarise, the aims of the experiments presented in this chapter are:

1. To determine the maximum temperatures that can be attained when heating thermoseeds of different sizes with a bespoke MR-compatible heating device, in air
2. To determine the time taken for thermoseeds to heat to a target temperature of 70 °C, in air
3. To assess the extent of thermoseed heating under more biologically relevant conditions, such as in water and ex vivo tissue
4. To measure the distribution of heat surrounding a thermoseed when heated in ex vivo tissue

6.2 Methods

All heating experiments were performed using a custom-designed MR-compatible magnetic alternating current hyperthermia (MACH) system, made by collaborator Paul Southern from Resonant Circuits Ltd. (Figure 6.2A). The MACH system consists of a 5-turn solenoid coil, 40 mm in diameter and 50 mm in length, which is connected to a circuit board and power supply by long cable extensions, allowing it to be set up in the preclinical 9.4 T MRI scanner safely (Figure 6.2B). The coil can produce an AMF ranging from 2 – 8 kA m^{-1}, at a frequency of 710 kHz (Figure 6.2D). Along the longitudinal axis of the coil the field strength is greatest at the centre and decreases by almost half at the coil openings (Figure 6.2C). For all experiments presented in this thesis, a field strength of 8 kA m^{-1} was used.

A fibre optic temperature probe (FOTEMP1-OEM, Weidmann Optocon, Germany) was used to measure the temperature of the thermoseed and its surrounding media in the relevant experiments. Thermoseeds were spherical in shape, made from chrome steel and purchased from Simply Bearings, UK. Statistical analysis was performed in GraphPad Prism.

6.2.1 Heating in air

The fibre optic temperature probe was supported vertically with a cardboard structure, allowing a thermoseed to be positioned on and in contact with the tip of the probe (Figure 6.1). The heating coil was then placed around the probe and thermoseed, with the thermoseed centred to align with the maximum field generated by the coil. For initial experiments, performed to assess the

repeatability of heating, 5 different 2 mm diameter thermoseeds were heated for 15 s, and the surface temperature of the thermoseeds was recorded for the heating duration and up to 3 minutes post heating. The heating protocol was repeated 5 times per thermoseed, and one-way ANOVA testing was carried out across the thermoseeds.

Thermoseeds ranging from 1 – 3 mm in diameter were then heated for 1 minute to assess the maximum temperatures that could be attained using the MACH system. To ensure the coil did not overheat, the maximum duration for which the AMF could be applied was 1 minute. A total of 3 repetitions were performed for each thermoseed size, and the temperature of the thermoseed was recorded up to 2 minutes post heating. Linear regression analysis was performed on the measured temperature change vs. thermoseed size following 30 s and 60 s of heating.

Figure 6.1 Setup for heating experiments in air. A fibre optic temperature probe was supported with a cardboard structure, allowing the tip to be pointing up vertically. The thermoseed was positioned on and in contact with the tip of the probe (left). The coil was placed around the cardboard support, with the thermoseed positioned in the centre of the coil to align within the maximum field generated by the coil.

Next, the time taken for thermoseeds (1.5 – 3 mm diameter) to reach the target temperature of 70 °C, upon application of an AMF, was determined. The time taken for thermoseeds of different sizes to reach 70 °C in the previous experiment (Figure 6.5A) were used as an initial estimate. If heating for this duration caused the thermoseed to heat above 75 °C, the experiment was repeated for a shorter duration. This process was repeated while iteratively decreasing the AMF application time until the thermoseed heated to 70 – 75 °C. Heating for the

determined duration was then repeated an additional 4 times to give 5 repeated measurements. Thermoseed cooling was monitored for up to 3 minutes, and the cooling curves were fitted with a mono-exponential decay.

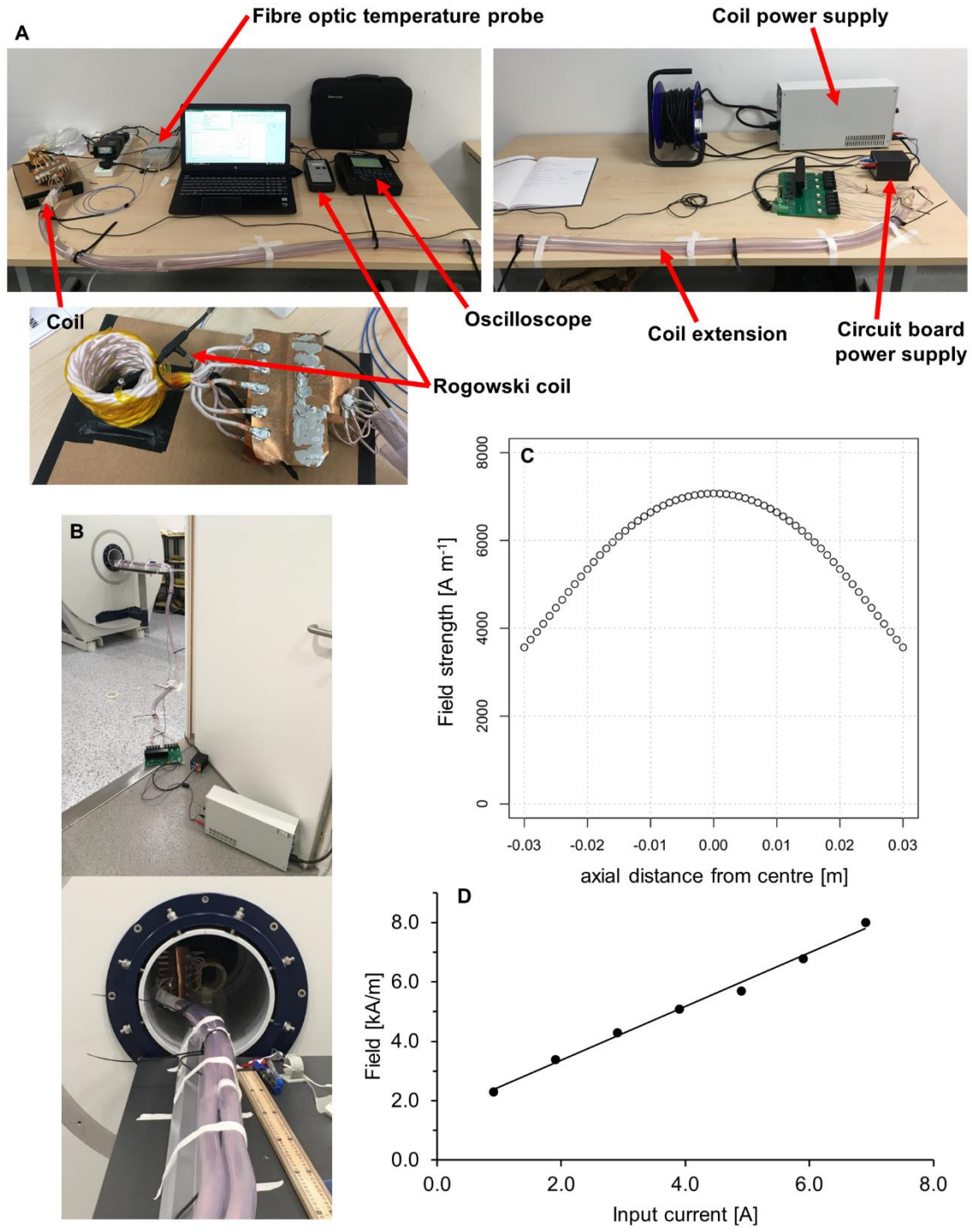

Figure 6.2 Magnetic alternating current hyperthermia (MACH) system setup. **A** MR-compatible MACH system set up on the bench top for in vitro experiments. **B** MACH system set up in the bore of a 9.4 T preclinical MRI scanner. **C** Modelled field strength for the MACH system with a maximum field strength of 7 kA m^{-1}. Simulation data supplied by Paul Southern, Resonant Circuits Ltd. **D** Measured field strength generated by the MACH system across a range of input currents.

6.2.2 Heating in water

Thermoseeds ranging from 2 – 3 mm in diameter were submerged in 1 mL of water in a 1.5 mL Eppendorf. The heating coil was placed around the sample, and the fibre optic temperature probe was passed through an opening in the lid of the Eppendorf to be positioned on the surface of the thermoseed. The temperature of the thermoseed was recorded while heating for 1 minute and for an additional minute once the AMF was removed.

6.2.3 Heating in ex vivo liver tissue

6.2.3.1 Liver tissue preparation

Lamb liver tissue was purchased from a local butcher within 48 hours post mortem and refrigerated until use. Samples were prepared by sectioning the liver into ~ 2 × 2 × 2 cm^3 cubes and allowing them to warm to room temperature.

6.2.3.2 Gross ablation following 1 minute of heating

A 2 or 3 mm diameter thermoseed was inserted through the base into the centre of the liver section, the sample was placed into the heating coil, and an AMF was applied for 1 minute. The liver tissue was then sliced in half, through the position of the thermoseed, so that the ablated region was readily visible on the inside faces of the two sections.

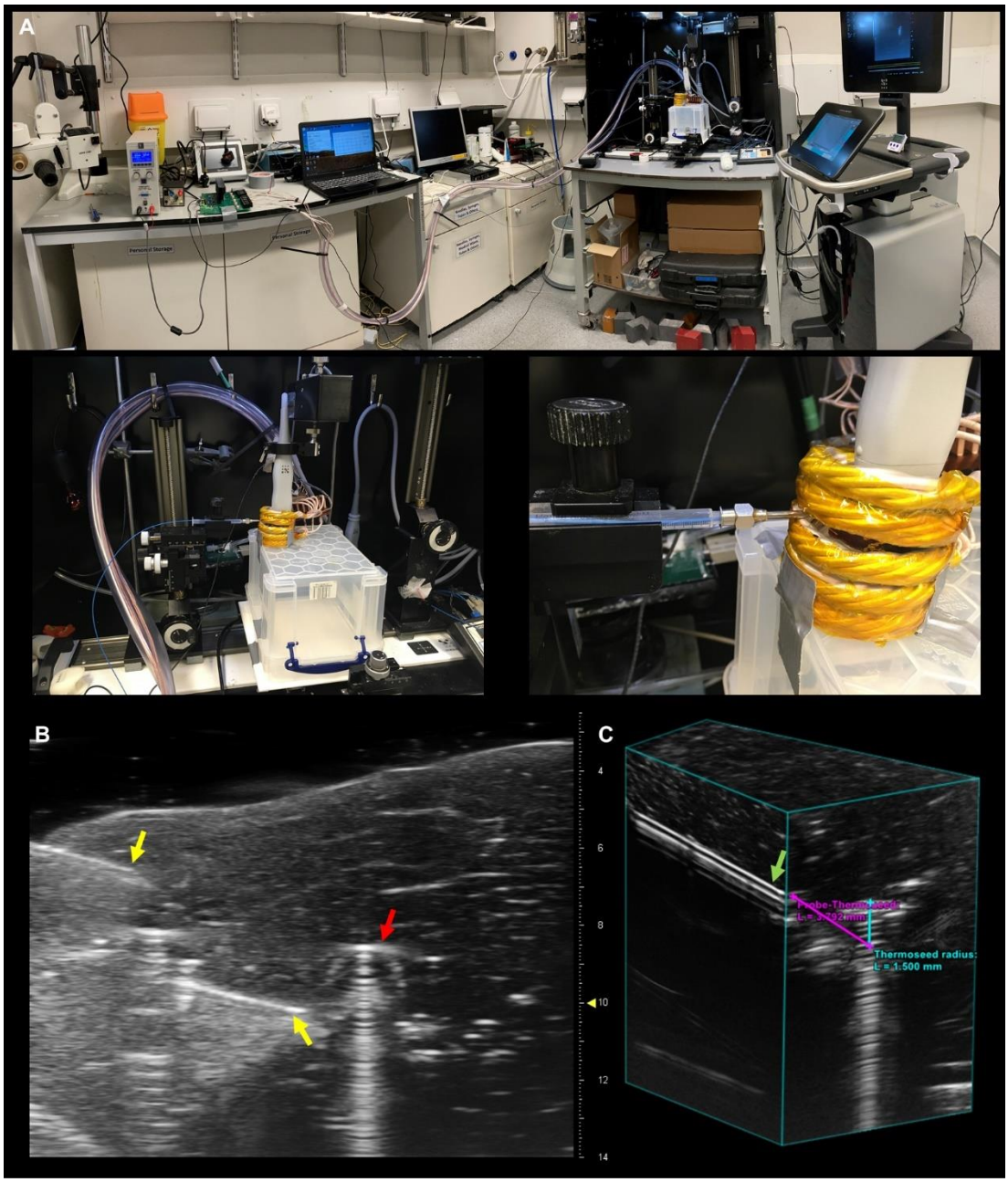

Figure 6.3 MACH system and ultrasound setup for heating in ex vivo liver tissue. A The MR-compatible MACH system was set up in the ultrasound lab, allowing the ex vivo liver tissue to be imaged whilst in the heating coil. **B** Ultrasound image of a 2 mm thermoseed (red arrows) in ex vivo liver tissue, with a needle inserted under ultrasound guidance (yellow arrows), to allow a fibre optic temperature probe to be placed a known distance from the thermoseed's surface. **C** 3D ultrasound images were used to measure the distance from the fibre optic probe (green arrow) to the thermoseed. Repetitions performed with the fibre optic probe at different distances from the thermoseed's surface allowed an understanding of the temperature distribution around the thermoseed to be formed.

6.2.3.3 Temperature measurement around the thermoseed

A 2 or 3 mm diameter thermoseed was inserted through the base into the centre of the liver section. The sample was positioned in the heating coil, and a fibre

optic temperature probe was inserted into the sample under ultrasound-guidance, enabling the temperature of the surrounding tissue to be measured during the heating procedure. This was achieved by first inserting a 12 gauge needle through the turns of the heating coil and into the liver sample, whilst imaging with ultrasound (Figure 6.3A). Ultrasound imaging was carried out on a VisualSonics Vevo 3100 system fitted with a VisualSonics MX550S transducer. Once the bevel of the needle was positioned close to the thermoseed (Figure 6.3B), the fibre optic temperature probe was passed through the needle and into the liver tissue. The needle was then retracted, whilst keeping the probe in place, and a 3D ultrasound image was acquired. Subsequently the ultrasound probe was removed, and the AMF applied for 1 minute. Once the thermoseed and sample had cooled for 3 minutes, the heating was repeated twice more with the same sample and set up to give a total of 3 measurements for each thermoseed-probe distance. Using the 3D ultrasound image, the distance between the thermoseed surface and the tip of the fibre optic temperature probe was determined (Figure 6.3C); this was performed using vendor software Vevo Lab. This entire process was repeated with a 2 and 3 mm thermoseed in a total of 10 and 11 liver samples respectively. Across all samples, the fibre optic probe was positioned within 0.3 – 5.3 mm of the thermoseed's surface. Due to difficulty when positioning the probe, the temperature could not be recorded with the probe directly touching the surface of the thermoseed.

6.3 Results

6.3.1 Heating in air

A total of 5 different thermoseeds, all 2 mm in diameter, were heated 5 times to assess the repeatability of heating. The mean heating curves for each of the thermoseeds were very similar (Figure 6.4A), and following 15 s of heating, no difference in temperature change was observed between thermoseeds (Figure 6.4B). For each individual thermoseed, the maximum temperature change had a standard deviation of no more than 3.0 °C, thus demonstrating the repeatability of thermoseed heating when using the MR-compatible MACH system.

Thermoseeds of different sizes were then heated in air to assess the maximum temperatures that could be attained when applying an AMF for 1 minute. A

maximum temperature of 201 °C and 43 °C was measured for 3 and 1 mm diameter thermoseeds respectively, corresponding to heating rates of 3.35 °C s^{-1} and 0.72 s^{-1} (Figure 6.5A). The change in temperature was directly proportional to thermoseed size, with larger thermoseeds heating more quickly (Figure 6.5B, Table 6.1). A thermoseed of 1 mm diameter was not able to reach the target temperature of 70 °C within the 1 minute heating window and, therefore, was not used in future experiments.

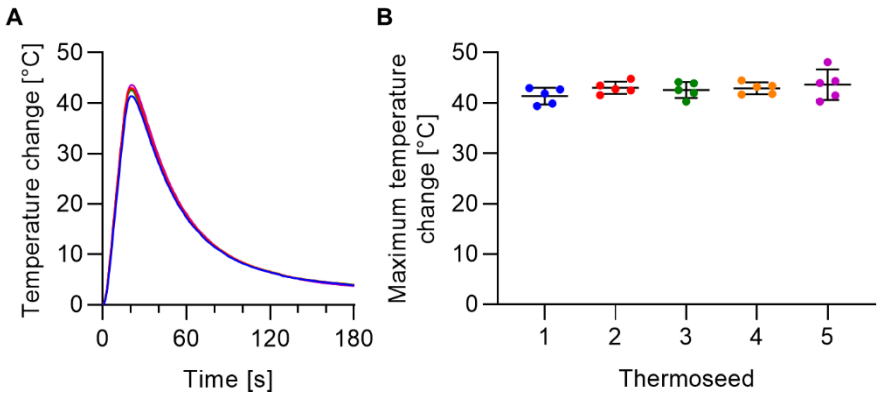

Figure 6.4 Repeatability of thermoseed heating. A Mean change in temperature of 5 different 2 mm thermoseeds heated for 15 s (n = 5). **B** Maximum temperature change measured for each thermoseed.

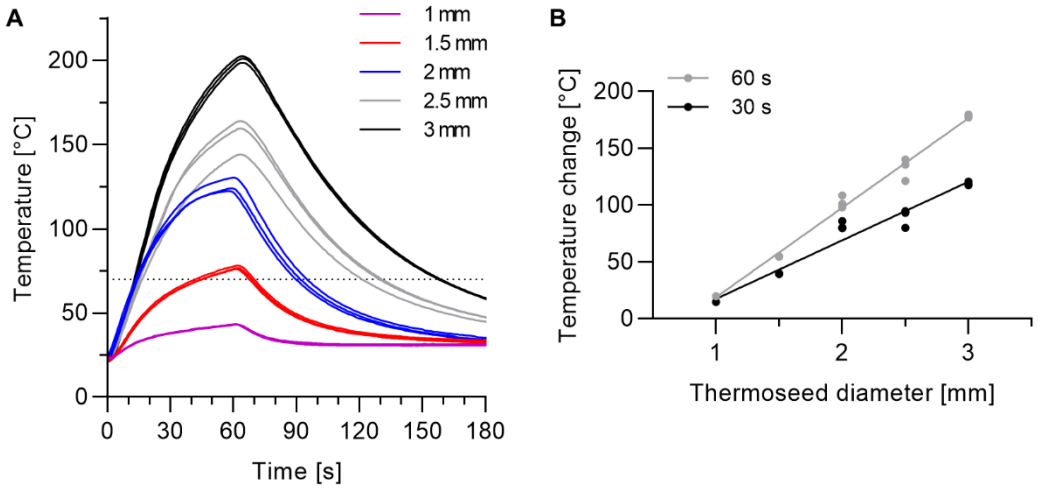

Figure 6.5 Thermoseed heating in air. A Temperature of 1 – 3 mm diameter thermoseeds heated in air for 1 minute (n = 3). The dotted line indicates the target temperature of 70 °C. **B** Temperature change following 30 s and 60 s of heating vs. thermoseed diameter. Data fitted with a simple linear regression model (n = 3). Full linear regression analysis presented in Table 6.1.

Heating duration [s]	Slope [°C s^{-1}]		Intercept [°C]		R^2	p
30	51.5	2.9	-33.9	6.1	0.96	< 0.0001
60	78.8	2.2	-59.7	5.0	0.99	< 0.0001

Table 6.1 Linear regression analysis for thermoseed heating in air. Temperature change = slope * (thermoseed diameter) + intercept. Coefficient and standard error reported for the slope and intercept, n = 3, Figure 6.5B.

For MINIMA to be effective, thermal ablation must be delivered efficiently and in a reasonable time frame. Therefore, the minimum heating duration required for thermoseeds of different sizes to reach the target temperature of 70 °C was measured. A 3 mm thermoseed only required the AMF to be applied for 9 s to reach 70 °C, whereas a 1.5 mm thermoseed required heating for 40 s (Figure 6.6A, Table 6.2). However, the 3 mm thermoseed also required longer to cool down (Figure 6.6B), with a cooling half-life of 52.2 s, compared with 20.6 s for the 1.5 mm thermoseed (Table 6.3). The rate of cooling is important to consider, as once the treatment has been delivered the thermoseed would need to return to body temperature before it can be navigated from the target back to the insertion site from retrieval.

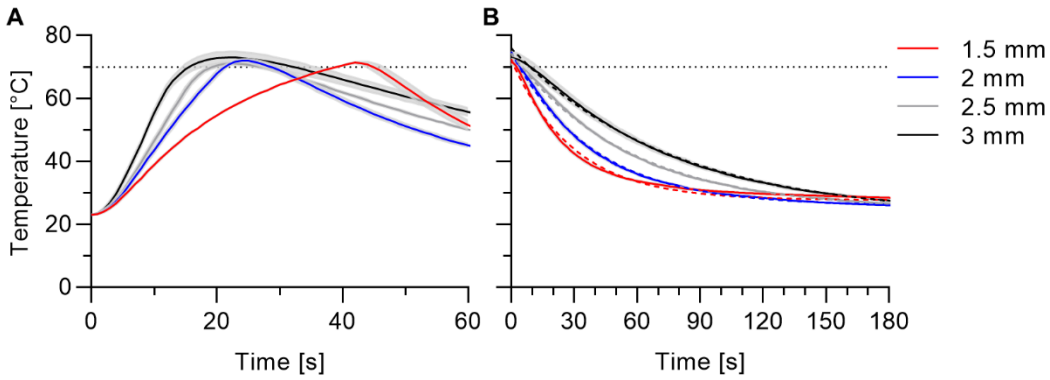

Figure 6.6 Thermoseed heating to 70 °C and subsequent cooling. A Temperature of 1.5 – 3 mm diameter thermoseeds heated to a target temperature of 70 °C. Corresponding heating times are detailed in Table 6.2. **B** Cooling of thermoseeds from 70 °C. Data fitted with a mono-exponential decay. Full fit data is provided in Table 6.3. (n = 5). The dotted line indicates the target temperature of 70 °C.

Thermoseed diameter [mm]	Time to heat to 70 °C [s]
1.5	40
2.0	19
2.5	14
3.0	9

Table 6.2 Thermoseed heating to 70 °C. Time taken for 1.5 – 3 mm diameter thermoseeds to heat to a target temperature of 70 °C (Figure 6.6A).

Thermoseed diameter [mm]	k [s^{-1}]	Plateau [°C]	Intercept [°C]	Cooling half-life [s]	R^2
1.5	0.034	27.7	72.4	20.6	0.99
2.0	0.026	25.9	74.8	26.8	1.00
2.5	0.018	24.6	74.4	38.7	1.00
3.0	0.013	22.6	76.0	52.2	1.00

Table 6.3 Thermoseed cooling exponential decay fit parameters. Temperature = (intercept – plateau) * exp(–k * thermoseed diameter) + plateau, n = 5, Figure 6.6B.

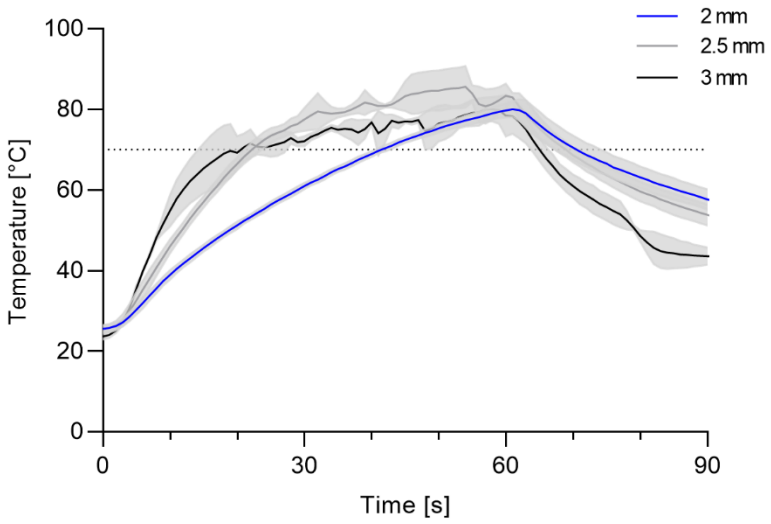

Figure 6.7 Thermoseed heating in water. Temperature of 2 – 3 mm diameter thermoseeds heated in water for 1 minute (2, 2.5 mm, n = 5; 3 mm, n = 2).

6.3.2 Heating in water

To investigate the effect of surrounding media on the temperatures attainable, thermoseed temperature was measured when heated in water for 1 minute. Although fluctuations in the heating curve were observed at temperatures greater than 70 °C (Figure 6.7), 2, 2.5 and 3 mm thermoseeds were all successfully heated above the target temperature, reaching approximately 80 °C within 1 minute. This was markedly lower than temperatures measured in air, with a

difference of 23, 47 and 99 °C for 2, 2.5, and 3 mm thermoseeds respectively; this is due to differences in the thermal properties between air and water. Since water is more comparable to tissue in this regard, these data provide confidence that temperatures required to deliver thermal ablation could be attained in vivo.

6.3.3 Heating in ex vivo liver tissue

Although the experiments in air and water provide some indication that temperatures required to achieve thermal ablation are attainable, it is also important to understand the temperature distribution around the thermoseed. To do this, thermoseeds were inserted into ex vivo liver tissue and heated for 1 minute. Using ultrasound-guidance, a fibre-optic temperature probe was inserted into the tissue and placed at a measured distance from the thermoseed's surface. Liver tissue was chosen to mimic in vivo heating more closely, however, this phantom still had limitations, such as lack of perfusion, which may lead to an overestimation of heating.

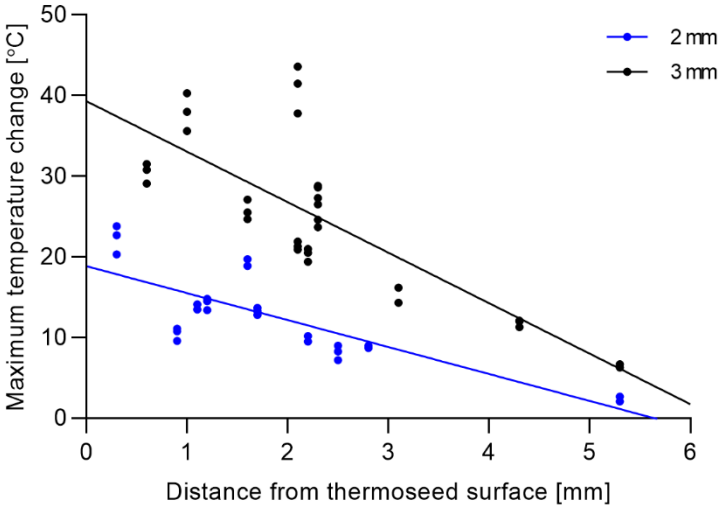

Figure 6.8 Thermoseed heating in ex vivo liver tissue. Maximum temperature change measured 0 – 6 mm from the surface of 2 and 3 mm thermoseeds heated in ex vivo liver tissue. Data is fitted to a linear model. Full linear regression data is presented in Table 6.4.

Thermoseed diameter [mm]	Slope [°C mm^{-1}]		Intercept [°C]		R^2	p
2	-3.3	0.4	18.9	1.1	0.66	< 0.0001
3	-6.3	0.8	39.3	2.2	0.66	< 0.0001

Table 6.4 Linear regression analysis for ex vivo liver data. Temperature change = slope * (distance from thermoseed surface) + intercept. Coefficient and standard error reported for the slope and intercept, n = 3. Slopes are significantly different, p = 0.003.

Due to variation in the starting temperature for repeat measurements recorded at each distance, temperature change has been plotted in Figure 6.8 instead of absolute temperature. Temperature change was negatively correlated with distance from the thermoseed (Figure 6.8), and linear regression analysis showed that the temperature gradient for the 3 mm thermoseed was more negative than the 2 mm thermoseed, -6.3 °C mm^{-1} vs. -3.3 °C mm^{-1} ($p = 0.003$, Table 6.4). To reach the target temperature of 70 °C in vivo, a temperature increase of 33 °C would be required; this degree of change was achieved up to 1 mm from the surface of the 3 mm thermoseed. Similarly, when liver tissue was dissected following 1 minute of heating with a 3 mm thermoseed, the average reach of the ablation area from the thermoseed's surface was 1.1 mm (calculated from a mean ablation area of 21.4 mm^2, Figure 6.9). The target temperature change of 33 °C was not observed with the 2 mm thermoseed, although a 14 °C increase was measured at 1 mm from the surface, which may be useful for alternative heating strategies, such as AMF pulsing (Tansi *et al.*, 2021). The gross ablation area was negligible in the samples heated for 1 minute with a 2 mm thermoseed, and therefore, photographs of these samples are not presented.

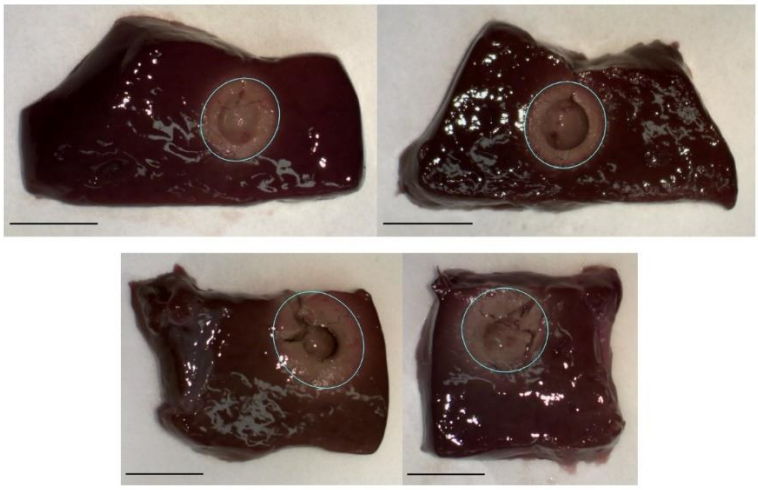

Figure 6.9 Thermal ablation in ex vivo liver tissue. Photographs of two samples of ex vivo liver tissue (top and bottom) heated with a 3 mm thermoseed for 1 minute. Mean area of ablated regions (blue ovals) = 21.4 mm^2. Scale bar = 5 mm.

6.4 Discussion

In this study, I have demonstrated that ferromagnetic thermoseeds can be heated to a target temperature of 70 °C, using an externally applied AMF delivered with a bespoke MR-compatible heating coil. Initially, thermoseed heating was shown to be repeatable in air, with recorded temperatures having a standard deviation of no more than 3 °C. This high degree of repeatability is essential for MINIMA, to ensure the thermal dose can be controlled and delivered with precision throughout the procedure. The result also provided assurance that any variation observed in future experiments would unlikely be due to the thermoseed itself.

Next, thermoseeds of different sizes were heated in air and water, with thermoseeds ≥ 2 mm in diameter reaching a target temperature of 70 °C under both conditions. To ablate at multiple locations using a single thermoseed, which is navigated between locations using the MRI scanner, rapid thermoseed heating is required to induce immediate cell death via coagulative necrosis and minimise the overall procedure duration. The data presented in this chapter suggests that the thermoseed must be at least 2 mm in diameter to achieve this. This is a reasonable size for the intended application and aligns with the navigation data, which required a 2 mm thermoseed or larger to penetrate brain tissue (Figure 5.4).

Fluctuations in temperature were observed when heating 2.5 and 3 mm thermoseeds in water, at temperatures ≥ 70 °C. These fluctuations are likely due to poor contact between the fibre optic probe and the thermoseed, caused by water boiling on the thermoseed's surface. Looking at the first 10 s of the heating curves provided in Figure 6.7, the rate of heating is much more rapid for the 2.5 and 3 mm thermoseeds; this alongside the data acquired in air (Figure 6.5) suggest that thermoseeds of this size may heat up to temperatures > 80 °C in water. It is possible at these high temperatures that water on the surface of the thermoseed begins to evaporate, forming bubbles, which may impair contact with the probe. This could then result in fluctuating temperatures and a lower temperature recorded overall. Since the 2 mm thermoseed only reached 80 °C following the full 1 minute of AMF application, the same effect was not observed. Despite these discrepancies, all thermoseeds ≥ 2 mm in diameter heated above the target temperature of 70 °C in water, suggesting that temperatures sufficient for thermal ablation may be attainable in vivo.

Finally, experiments were performed in ex vivo liver tissue to provide some indication of the temperature distribution around a heated thermoseed. Based on the linear regression analysis, a temperature increase of 39 °C was reached with a 3 mm thermoseed following 1 minute of heating, which would give an absolute temperature of > 70 °C if starting from 37 °C. A sufficient temperature change was also measured up to 1 mm from the thermoseed's surface, equating to a 65 mm^3 spherical ablation volume; heating at this rate would enable a 1 cm^3 volume to be ablated within 15 minutes. The 2 mm thermoseed only increased in temperature by 19 °C, equating to just 56 °C if starting from body temperature. These results were unexpectedly low, and contrary to previous data acquired in 3D cell culture, which showed that ablation volumes as large as 85 mm^3 could be obtained by heating a 2 mm thermoseed for 1 minute (Baker *et al.*, 2022). This discrepancy is most likely due to the target temperature of 70 °C being too high and cell death occurring at lower temperatures. Interpreting the ex vivo liver data alongside the cell culture data may allow a more realistic target temperature to be determined. An 85 mm^3 spherical ablation volume is equivalent to a reach of 1.75 mm from the surface of a 2 mm thermoseed. Using the linear regression analysis presented in Figure 6.8 and Table 6.4, a temperature increase of 13 °C would be measured at this distance, giving a 50 °C threshold temperature for cell

death. For the 3 mm thermoseed, a 13 °C temperature increase was measured up to 4.2 mm from the thermoseed's surface, which is equivalent to a 775 mm^3 ablation volume; this would allow a 1 cm^3 volume to be ablated within just 1.3 minutes. In reality the threshold temperature is likely to be somewhere in between 50 and 70 °C, as although coagulative necrosis is reported to occur at temperatures ≥ 50 °C (Chu and Dupuy, 2014), 1 minute at 50 °C gives a thermal dose of just 1.875 CEM_{43} (calculated using equation 6.1), which is 128 times lower than the widely accepted clinical dose of 240 CEM_{43} (Mouratidis, Rivens and ter Haar, 2015).

The ex vivo liver data also disagreed with the other experiments presented in this chapter; particularly the heating in water, in which a 2 mm thermoseed reached 80 °C within 1 minute, when starting from a baseline temperature of 25 °C. This discrepancy may be due to a systematic error when identifying the tip of the fibre optic probe or the thermoseed on the liver ultrasound image. For example, if the distance between the probe tip and the thermoseed's surface was underestimated, then a lower temperature would be recorded for a given distance. Alternatively, the discrepancy may be due to the volume of water and liver used in the two experiments, 1 cm^3 and ~ 8 cm^3 respectively. Assuming the two samples have similar values for thermal conductivity and specific heat capacity (Hasgall *et al.*), the larger volume of tissue available to disperse heat generated by the thermoseed may explain why lower temperatures were recorded in the liver in comparison to water.

In all experiments, the relationship between heat generation and thermoseed size, as described in equation 2.11, is supported, with larger thermoseeds heating to greater temperatures under all conditions. It is therefore possible to envisage thermoseed size being adjusted and used as an additional measure of temperature control, alongside AMF duration. In addition to thermoseed size, the material of the thermoseed is an important factor. Since the eddy currents responsible for heat generation are predominantly on the surface of the thermoseed (section 2.3), different electrical conducting coatings may be added to improve the heating capability, without compromising the ferromagnetic core required for navigation (Cetas, Gross and Contractor, 1998). Field strength and frequency are two parameters that may also be used to adjust thermoseed

heating, and optimisation of the AMF in combination with the specific thermoseeds used for MINIMA should be performed in the future to improve both the extent and efficiency of heating.

Preliminary data presented in this chapter suggests that thermoseed's can be heated using an MR-compatible heating coil, to reach temperatures required for thermal ablation. However, when performed in vivo, additional factors will affect the heating capability of the thermoseeds. For example, blood flow may act as a heat sink, thus limiting the temperature of the thermoseed and consequently the therapeutic effect. Chapter 7 aims to address this by delivering thermal ablation in vivo, in animal models of both healthy and diseased tissue.

7 Thermal ablation in vivo

7.1 Introduction

In the previous chapter, an MR-compatible MACH system was used to heat thermoseeds in both air and biologically relevant media in vitro. Thermoseeds 1.5 mm in size or larger were readily heated above 70 °C, at which point cell death would be induced within seconds (Nikfarjam, Muralidharan and Christophi, 2005; Lecornet *et al.*, 2010; Valerio *et al.*, 2014). Furthermore, a temperature increase of 33 °C, which is sufficient to reach 70 °C in vivo, could be achieved up to 1 mm from the thermoseed's surface, providing some indication of achievable ablation volumes. However, when heating thermoseeds in vivo, additional consideration must be given to biological processes, such as perfusion, that may limit the rate of heating and the maximum attainable temperature.

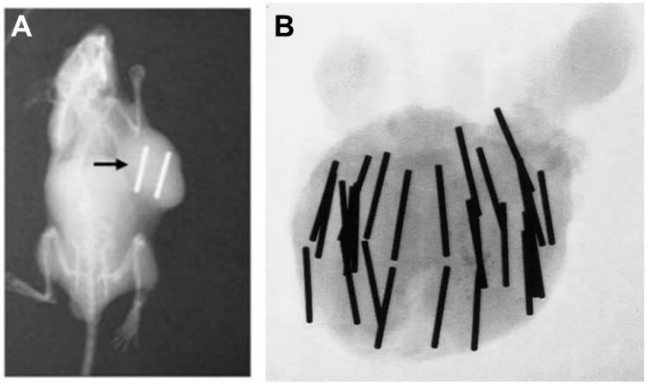

Figure 7.1 Implanted rod-shaped thermoseeds for thermal ablation. A X-ray of two 0.9 mm diameter, 1.04 cm long thermoseeds positioned in a melanoma cancer cell line mouse subcutaneous tumour (Xia *et al.*, 2011). **B** X-ray showing typical placement of multiple 1 mm diameter, 1 cm long thermoseeds in the prostate to deliver thermal ablation therapy (Tucker, Huidobro and Larson, 2005).

Preclinical in vivo studies performed to date have predominantly used an array of rod-shaped, 'constant-temperature' thermoseeds that do not heat past their defined Curie temperature (typically 50 - 60 °C) (Burton, Hill and Walker, 1971; Brezovich, Atkinson and Chakraborty, 1984). This method allows the maximum temperature to be tightly controlled, but requires prolonged heating to deliver an effective thermal dose across the entire tumour volume. Geng *et al.* (1998) showed how two 1 cm rod-shaped thermoseeds positioned in parallel increased temperatures at the centre of a subcutaneous hepatic tumour in mice to 50 °C

within 30 minutes; typical thermoseed positioning is shown in Figure 7.1A. A similar study, performed in melanoma subcutaneous tumours, also observed a plateau in interstitial temperature at 50 °C across a 20 minute heating period (Xia *et al.*, 2011). Some variation in maximum interstitial temperatures can be attained by altering the Curie temperature of the thermoseed, but these typically remain within the range of 45 – 55 °C (Ouyang *et al.*, 2010).

Few clinical studies have used AMF heating of thermoseeds to perform thermal ablation in cancer, with the majority focusing on treatment in the prostate. One study found that using a single rod did not provide extensive heating, but when using an array of rods with a Curie temperature of 70 °C positioned 1 cm apart, consistent necrosis was observed following four 1 hr treatments (Tucker *et al.*, 2000). This approach was repeated in a later study conducted by the same group, and of the twenty patients treated, just five had a positive biopsy 1 year post treatment (Tucker, Huidobro and Larson, 2005). However, 30 – 60 rods had to be inserted into the prostate of each patient (Figure 7.1B), and it was observed that those with negative biopsies had a higher rod density on average than those with a positive biopsy, suggesting that a larger number of rods was required for the treatment to be effective. Some clinical studies have combined thermoseed heating with radiation therapy to provide additional cytotoxicity and sensitisation (Deger *et al.*, 2002). And although this has similarly proved to be effective, with interstitial temperatures reaching 48 °C within a 60 minute heating period, once again a large number of thermoseeds were used (15 – 80) (Deger *et al.*, 2004).

With the ability to move thermoseeds through tissue, effective thermal ablation may be delivered using a single seed, thus minimising the complexity and invasive nature of the procedure. The MINIMA concept involves a single thermoseed navigated through the tumour, heated at different, distinct locations to ensure full coverage of the diseased tissue. For this procedure to be performed within a reasonable time frame, the thermoseed must be heated rapidly at each location, unlike the prolonged heating protocols used in the studies described previously. In vitro data presented in chapter 6 provides confidence that this is possible using the MR-compatible MACH system with spherical thermoseeds. Therefore, I hypothesised that an external alternating magnetic field at radiofrequency would efficiently heat a spherical ferromagnetic thermoseed to

induce localised regions of cell death in vivo, leaving distant tissue unaffected, and that this method of thermoablation would be effective as a cancer therapy. Experiments presented in this chapter aim to test this hypothesis, first by heating thermoseeds in healthy tissue in the rat brain and subsequently in a subcutaneous tumour model in mice. In the latter experiments, bioluminescence imaging was used to monitor cell viability.

To summarise, the aims of the experiments presented in this chapter are:

1. To assess whether sufficient thermoseed heating can be attained to induce cell death in vivo, in the rat brain
2. To develop a suitable experiment protocol to allow cell death induced by thermoseed heating to be measured using imaging techniques such as BLI and MRI
3. To perform a longitudinal study, assessing the efficacy of the thermal ablation component of MINIMA as a cancer therapy, in a mouse subcutaneous tumour model

7.2 Methods

All animal work was performed in accordance with the United Kingdom's Animals (Scientific Procedures) Act of 1986 and was previously approved by UCL's internal Animal Welfare and Ethical Review Body.

Thermal ablation was performed using a custom-built MR-compatible MACH system (Resonant Circuit Ltd., UK) consisting of a 5-turn solenoid coil, 40 mm diameter. An alternating magnetic field up to 8 kA m^{-1} could be generated at 710 kHz. The coil could only be applied continuously for 1 minute at a time, to mitigate overheating. For longer heating durations, the field was pulsed on and off at 1 minute intervals.

Although in the previous chapter 3 mm thermoseeds were shown to heat more rapidly and to higher temperatures than thermoseeds < 3 mm in diameter, 2 mm thermoseeds were alternatively used for in vivo experiments. This decision was made due to the relatively small size of the rat brain and the subcutaneous tumours used in the study. By reducing the thermoseed size, less damage to the

tissues would occur during thermoseed insertion, thus allowing a more accurate measure of damage specifically caused by thermal ablation. Furthermore, the experiments performed in air (Figure 6.5) and water (Figure 6.7) both suggest that a 2 mm thermoseed could be heated to sufficient temperatures to induce cell death in vivo.

7.2.1 Rat brain experiments

7.2.1.1 Animal model

A male Wistar rat (n = 1, 8 weeks-of-age) was bred by Charles River (UK) and delivered to CABI one week prior to experiments. The rat (300 g) was anaesthetised with 3.5 % isoflurane vaporised in oxygen at a flow rate of 1 L min^{-1}. The head was shaved, and the animal positioned in a stereotaxic frame in the horizontal skull position, where 2.5 % isoflurane (delivered in 1 L min^{-1} oxygen) was delivered via a nose cone. A midline incision was made in the scalp, and a cranial window made by removing a ~6 mm disc of skull above the left striatum (3 mm lateral and 0.2 mm anterior to bregma). A 27 gauge needle was inserted into the striatum (6 mm ventral to the brain surface) and removed. This process was subsequently repeated at the same position with a 21 and 18 gauge needle to create a tract. A 2 mm thermoseed was positioned on the surface of the brain, above the needle tract. The sphere was inserted into the striatum using a blunt 18 gauge needle, prior to the needle being retracted, and the skin sutured closed to cover the exposed brain surface and the skull.

7.2.1.2 Thermal ablation

The rat was transferred to the MACH system, with the head positioned in the centre of the coil and anaesthetic delivered via a nose cone (2.5 % isoflurane delivered in 1 L min^{-1} oxygen). An AMF (8 kA m^{-1}) was applied for 1 minute.

7.2.1.3 Brain tissue sample preparation

Following the heating, the animal was sacrificed with an overdose of pentobarbital administered via intraperitoneal injection. The animal was decapitated, sutures removed, and the sphere extracted through the original needle tract using a permanent magnet. The brain was removed from the skull and sectioned into 1 mm thick slices using a McIlwain tissue chopper (Mickle Laboratory Engineering Co. Ltd., UK). Each slice was placed into freshly prepared 1% TTC (2,3,5-

Triphenyltetrazolium chloride) solution (Sigma Aldrich, USA) and incubated at 37 °C for 10 minutes. The slices were removed from solution and were placed on a petri dish to be photographed immediately.

7.2.1.4 Image analysis

Images were loaded into ImageJ and an ROI was manually drawn around the area of cell death on each slice.

7.2.2 Subcutaneous tumour experiments

7.2.2.1 Cell culture

The human colorectal adenocarcinoma cell line SW1222, previously stably transduced with a lentiviral vector to express firefly luciferase enzyme (*Fluc*), were grown in T175 flasks (Fisher Scientific, Loughborough, UK) in DMEM, supplemented with 10% foetal calf serum (FCS, Invitrogen, Paisley, UK) in a humidified incubator at 37 °C with 95 % air and 5 % CO_2. Cells were grown to 80 % confluence before being trypsinised, centrifuged for pelleting at 300 g, counted and re-suspended in phosphate-buffered saline (PBS) for in vivo cell injection.

7.2.2.2 Animal model

Female CD-1 nude mice (7 ± 1 weeks old, 27.5 ± 2.5 g) were subcutaneously injected on the right flank with 5×10^6 or 2.5×10^6 SW1222^{Fluc} cells in 100 µL of PBS. Tumour growth was monitored every 3-5 days using BLI and calliper measurements. Measurements were taken in three orthogonal directions and tumour volumes were estimated using the following formula:

$$Volume = length \times width \times height \times \frac{\pi}{6} \qquad (7.1)$$

Mice were anaesthetised for all procedures with 4 % isoflurane delivered in 1 L min^{-1} oxygen and maintained at 2 % isoflurane. All mice were sacrificed by cervical dislocation, in accordance with regulations. A total of 3, 7 and 2 mice were used for the preliminary, sham and further preliminary studies respectively. In the final study, 6 mice were used in the treatment group and 7 in the control group.

7.2.2.3 Bioluminescence imaging

Mice were anesthetised, administered 120 mg kg^{-1} of D-luciferin in 200 µL of PBS intraperitoneally and placed on their side in the imaging chamber with the tumour facing up towards the camera. In preliminary studies, a single image was acquired at a set time point following luciferin injection, typically 12 minutes. For time course data, images were acquired 8 – 35 minutes post luciferin injection, at 1 minute intervals. In the final study, time course data was acquired at each time point, with the maximum luminescence reading used at each time point. During thermal ablation, single images were acquired at specific stages of the procedure, as described in sections 7.3.2 and 7.3.3. All images were acquired using auto exposure.

7.2.2.4 Magnetic resonance imaging

All images were acquired on a 9.4 T horizontal bore Bruker Biospec 94/20 system, using an 86 mm RF volume coil. A heat mat was used to maintain the core body temperature at 37 °C and respiration rate was monitored at 60 – 80 bpm. T_2-weighted images were acquired using a respiratory gated RARE spin echo sequence using the following parameters: TR = 820 ms, TE = 25 ms, FOV = 40 × 40 mm^2, matrix size = 256 × 256, 1 average, 10 contiguous 1 mm thick slices ensuring complete tumour coverage.

7.2.2.5 Thermal ablation

Mice were anaesthetised and a 19 gauge needle was inserted into the centre of the tumour and removed to create a tract. A 1.5/2 mm diameter thermoseed was inserted along the tract, into the tumour, using a blunt 19 gauge needle[iii]. The animal was transferred to the coil and the AMF was applied for a total of 1, 3 or 5 minutes, pulsed in a 1 minute on, 1 minute off fashion. Following ablation, the thermoseed was extracted through the original tract using a permanent magnet. BLI was performed throughout the procedure, as described in section 7.2.2.3.

[iii] Although I had planned to use 2 mm thermoseeds for all in vivo experiments, there was initially some difficulty inserting the thermoseeds into the subcutaneous tumours. For this reason, 1.5 mm thermoseeds were used for two animals in the preliminary study and all animals in the sham study. Once the thermoseed insertion had been refined, 2 mm thermoseeds were used for the remaining preliminary and final studies.

7.2.2.6 Image analysis

The total photon flux (radiance) from the BLI data was calculated within a defined ROI drawn around the tumour, using the Living Image software package (PerkinElmer, USA). MRI datasets were manually segmented to determine tumour volume using MATLAB (Mathworks, USA).

7.2.2.7 Histology

Mice were sacrificed 15 minutes (1 min heating) or 24 hours (3 x 1 min heating) post heating and the tumours removed for histology. Tumours were fixed in 4 % formalin, dehydrated in 70 % ethanol, and embedded in paraffin wax blocks. Tumours were sectioned at 3 µm and stained with hematoxylin for 1 min and eosin for 30 s using an automated slide stainer (Sakura, Netherlands). Sections were imaged using a NanoZoomer Digital Scanner and analysis software NDP.view2 (Hamamatsu, Japan). Images were processed in ImageJ using the NDPITools plugin (Deroulers *et al.*, 2013). Area of necrosis was segmented manually.

7.2.2.8 Statistical analysis

Statistical significance was determined using repeated measures one-way ANOVA followed by t tests multiple comparisons correction (Bonferroni method; IBM SPSS Statistics 27).

7.3 Results

7.3.1 Thermal ablation in the rat brain

A 2 mm thermoseed was inserted into the left striatum of the rat brain and heated for 1 minute. Then, once the brain had been removed and sectioned, the tissue was stained using TTC to distinguish healthy respiring tissue, stained red, from regions of cell death, which would remain unstained. In the brain slice where the thermoseed had been positioned, a 12.3 mm^2 area of cell death was clearly visible in the grey matter (Figure 7.2). Cell death was also observed in neighbouring slices, with smaller areas in slices further from the thermoseed.

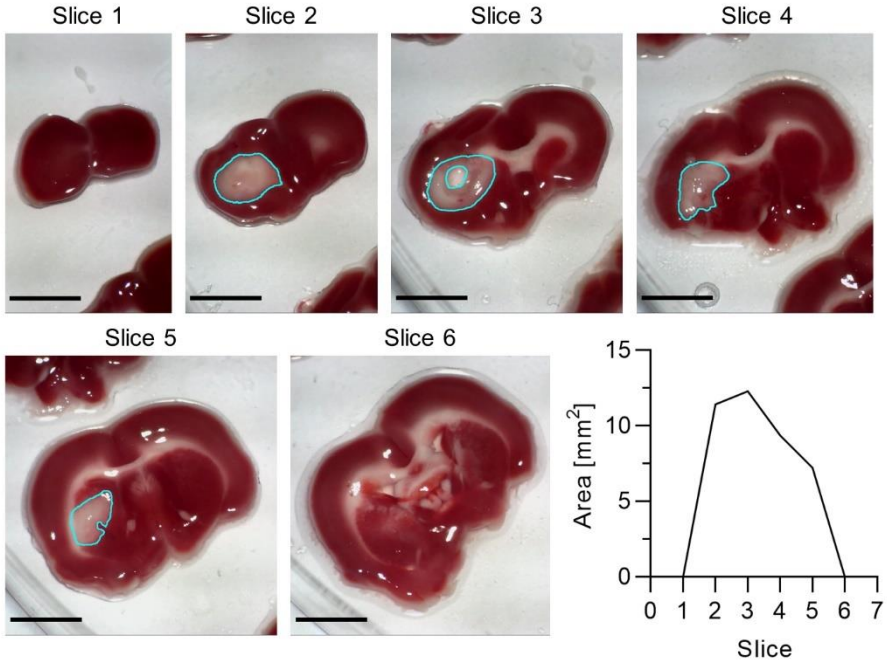

Figure 7.2 Cell death following thermal ablation in the rat brain. Rat brain slices stained with TTC, following 1 minute of heating with a 2 mm thermoseed (AMF = 8 kA m^{-1}, 710 kHz). Outlined regions indicate area of cell death. Area of cell death per slice (bottom right). Scalebar = 5 mm.

7.3.2 Subcutaneous tumour model: preliminary experiments

Thermal ablation was performed in a mouse subcutaneous tumour model, with cell viability monitored throughout the study using BLI. Images were acquired at four stages in the thermal ablation procedure: before (1) and after (2) thermoseed insertion, prior to heating, 3) post heating, and 4) following removal of the thermoseed (Figure 7.3A). The procedure led to a decrease in BLI signal in all mice, with the largest change observed following insertion of the thermoseed, between images 1 and 2 (38 – 55 % decrease, Figure 7.3C). In the mice treated with a 1.5 mm thermoseed, the signal continued to drop with each stage of the procedure. On the contrary, heating a 2 mm thermoseed lead to a 98 % increase in signal following heating, which decreased again once the thermoseed was removed; this result was unexpected, as the larger thermoseed should heat to higher temperatures and, therefore, induce a greater volume of cell death. The bioluminescence images show a clear void of signal in the centre of the tumour where the thermoseed was positioned (Figure 7.3B), which may be due to blocking of light by the thermoseed, as well as any damage caused upon insertion and removal of the thermoseed.

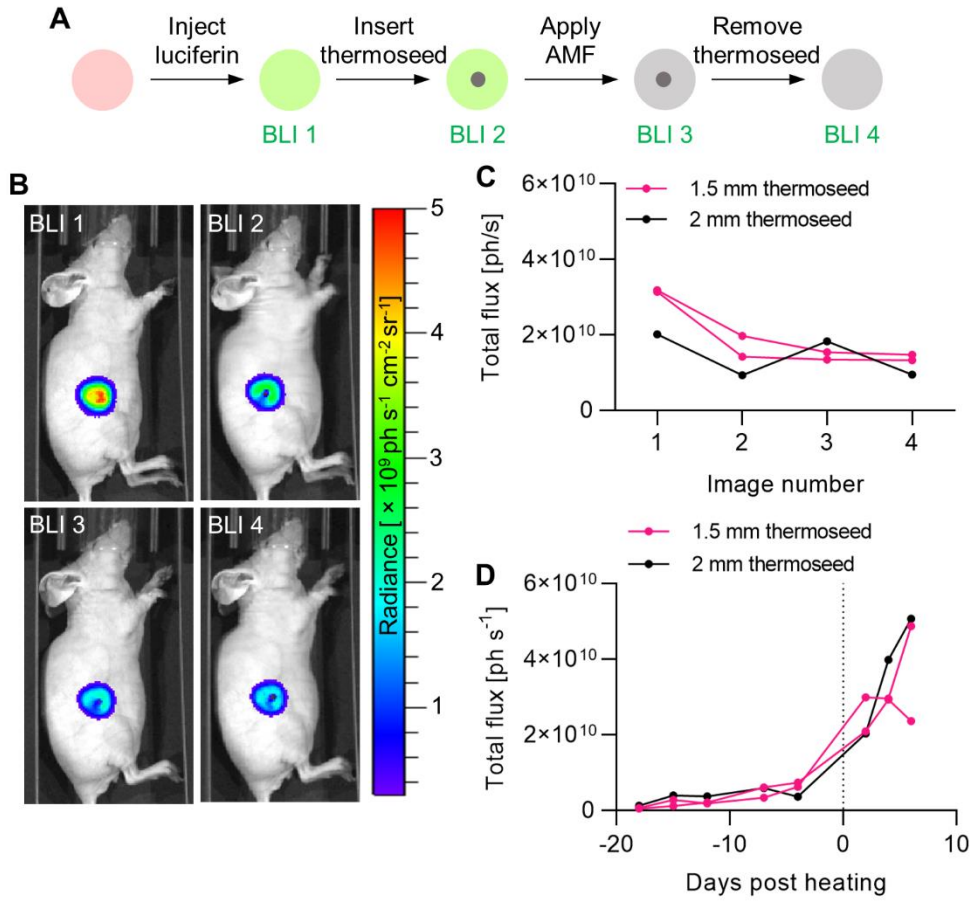

Figure 7.3 Bioluminescence imaging for preliminary ablation experiments in subcutaneous tumours. A Schematic outlining the thermal ablation procedure. Heating was performed with 1.5 mm thermoseeds in two mice and a 2 mm thermoseed in the third mouse. The alternating magnetic field was applied for 1 minute. Bioluminescence images were acquired at four stages of the procedure. **B** Representative bioluminescence images acquired at each of the four BLI timepoints. A clear void of signal is observed where the thermoseed was inserted. **C** Total bioluminescence signal detected across the tumour at each time point. Each line represents a different animal (n = 3). **D** Longitudinal BLI data acquired up to 18 days prior to and 6 days post heating. Each line represents a different animal (n = 3).

BLI was also performed up to 18 days prior to and 6 days post heating to track the growth of the tumours longitudinally. Although in one animal the signal does begin to decay following treatment, generally the growth of the tumours does not appear to be hindered (Figure 7.3D). Similarly, tumour volume, measured from MR images, continued to increase in all animals (Figure 7.4). Hypointense regions were observed on MR images of the tumours following heating.

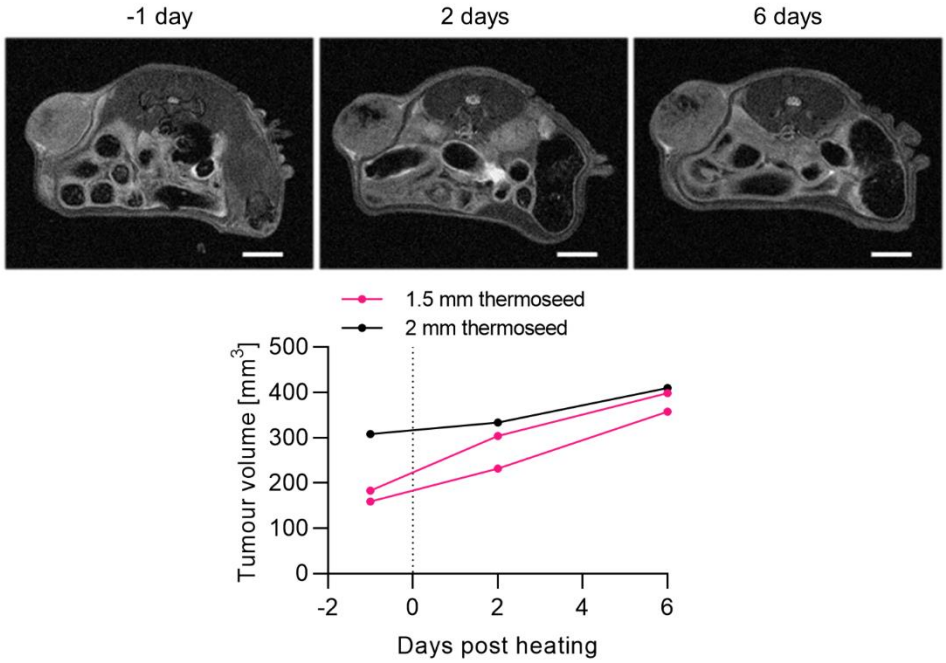

Figure 7.4 Tumour volumes measured using MRI. Representative T_2-weighted MR images acquired 1 day prior to and 2 – 6 days post heating (1.5 mm thermoseed, AMF applied for 1 minute, 8 kA m^{-1}, 710 kHz). Tumour volumes continued to increase in all animals following treatment.

A control study was conducted to further understand the variation in signal observed in the preliminary results. Once again, BLI was performed at four stages throughout the sham procedure: 1) before thermoseed insertion, 2) following creation of a needle tract, 3) after insertion of the thermoseed, and 4) following thermoseed removal (Figure 7.5A). The results were extremely variable, with no general trend following creation of the needle tract or insertion of the thermoseed (Figure 7.5B). However, when the thermoseed was removed the signal remained constant or increased in all animals except one (Figure 7.5B, pink line), in which case a 71 % decrease was observed. Images acquired at time points 1 and 3 were the only pair for which the signal intensity was found to be significantly different ($p = 0.022$, $n = 7$, Figure 7.5C). At this stage it was unclear as to why there was such variation in the detected BLI signal. However, based on the experiments in the previous chapter, it was possible that the 1.5 mm thermoseed was not inducing a volume of cell death large enough to cause a consistent change in signal. Therefore, having improved the method of thermoseed insertion, further preliminary heating experiments were performed using a larger, 2 mm thermoseed.

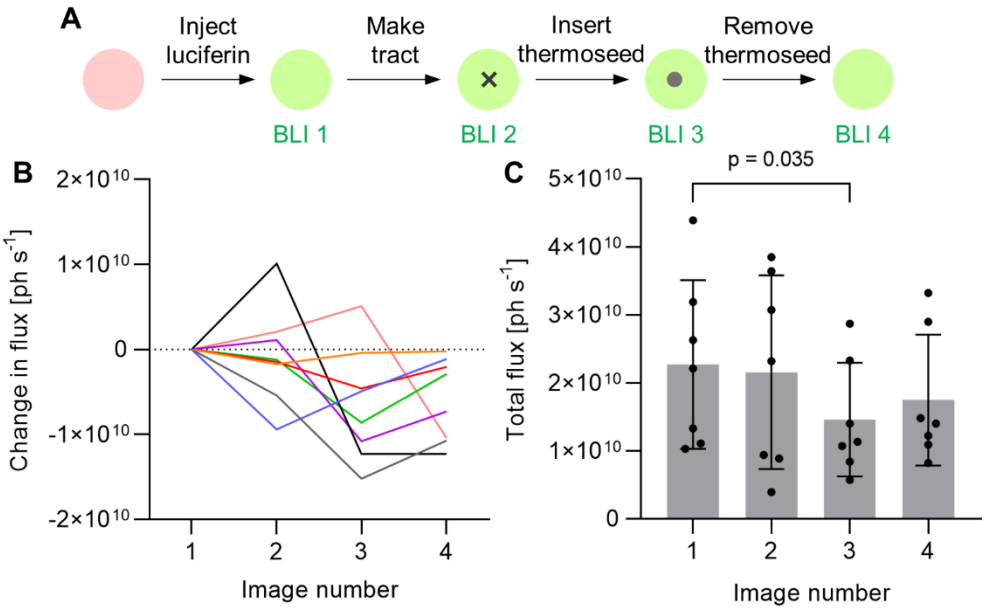

Figure 7.5 Bioluminescence imaging data for control thermal ablation experiments in subcutaneous tumours. A Schematic outlining the thermal ablation procedure. A 1.5 mm thermoseed was used in all animals. Bioluminescence images were acquired at four stages of the procedure. **B** Absolute change in bioluminescence signal detected across the tumour at each time point. Each line represents a different animal. **C** Total bioluminescence signal detected at each time point, excluding animal indicated in pink in B (n=7).

Considering the variability observed previously, in the next study images were only taken at two stages of the procedure, before and after heating, with the thermoseed positioned in the tumour in both cases, thus removing any effect arising from the insertion and removal of the thermoseed (Figure 7.6A). Additionally, one animal was treated for 1 minute and another for 3 minutes, to see if a longer heating duration could induce a larger ablation volume, which may improve the ability to detect an effect using BLI. As observed in the initial experiment performed with a 2 mm thermoseed (Figure 7.3C), the signal increased by 92 and 233 % following 1 minute and 3 minutes of heating respectively. Since the BLI signal is generated by metabolising cells, an increase in signal would ordinarily be interpreted as a greater number of viable cells, the opposite effect to what I was expecting. This signal increase did, however, begin to reduce across the 9 minutes following heating (Figure 7.6B).

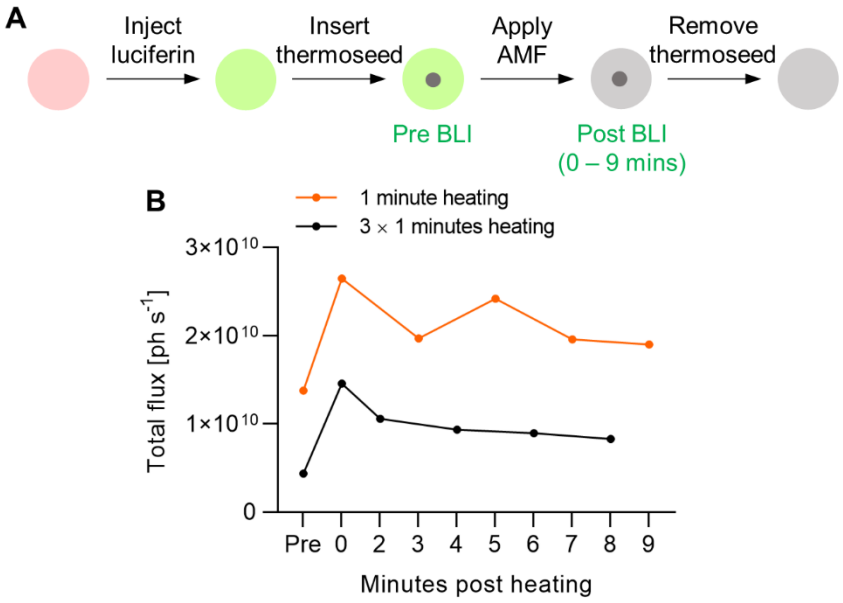

Figure 7.6 Further preliminary experiments. A Schematic outlining the thermal ablation procedure. Ablation was performed with a 2 mm thermoseed, and the alternating magnetic field (8 kA m^{-1}, 710 kHz) was applied for 1 or 3 × 1 minutes. Bioluminescence images were acquired at two stages of the procedure. **B** Total bioluminescence signal detected across the tumour pre heating, and up to 9 minutes post heating.

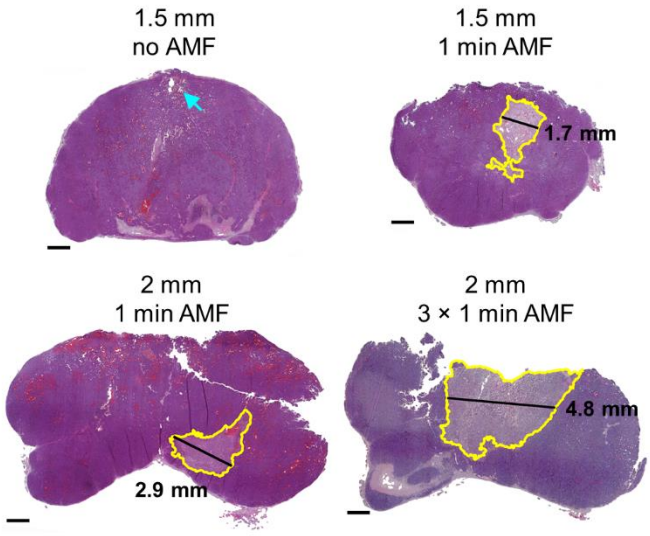

Figure 7.7 Histology of subcutaneous tumours post heating. H&E staining of sections of subcutaneous tumours ablated with a 1.5 or 2 mm thermoseed for 1 minute or 3 × 1 minutes show clear regions of necrosis (yellow ROI). The control sample has no distinct area of necrosis but does show the needle insertion tract (blue arrow). Scale bar = 1 mm.

Since the BLI had not provided any evidence of cell death following thermal ablation, histology was conducted on a select sample of subcutaneous tumours from the previously described experiments (Figure 7.7). Representative sections stained with haematoxylin and eosin (H&E) show clear regions of necrosis with approximate diameters of 1.7 mm and 2.9 mmm following 1 minute of heating with 1.5 and 2 mm thermoseeds respectively. In the control sample (1.5 mm thermoseed, no AMF) the needle tract through which the thermoseed was inserted is visible, but there is no distinct region of necrosis. Furthermore, when a 2 mm thermoseed was heated for a total of 3 minutes, a larger necrotic region, spanning 4.8 mm, was observed.

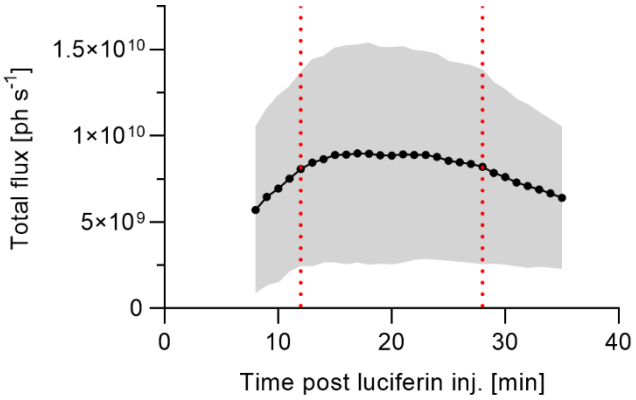

Figure 7.8 Time course of bioluminescence signal following luciferin injection. Data summarised from all animals in treated and control groups at 3 and 7 days prior to heating (n = 30, grey area indicates ± SD). Red lines indicate timing of pre and post images acquired during the heating procedure.

7.3.3 Subcutaneous tumour model: final study

With insight gained from the preliminary experiments, adjustments were made to the experimental protocol for the final study. This included inserting the thermoseed before the luciferin injection, maintaining the animals body temperature throughout the procedure and increasing the heating duration to a total of 5 minutes. BLI was once again performed at two stages in the procedure, with the thermoseed in place (Figure 7.9A), in addition to images acquired longitudinally, without the thermoseed, to track the growth of the tumours before and after treatment. For the longitudinal data, a time course of the BLI signal following luciferin injection was acquired; the maximum value in the time course was used at each time point. On the day of heating, the pre-image was

consistently acquired 12 minutes post luciferin injection, and the post-image was acquired within 28 minutes, as indicated on the time course plot in Figure 7.8.

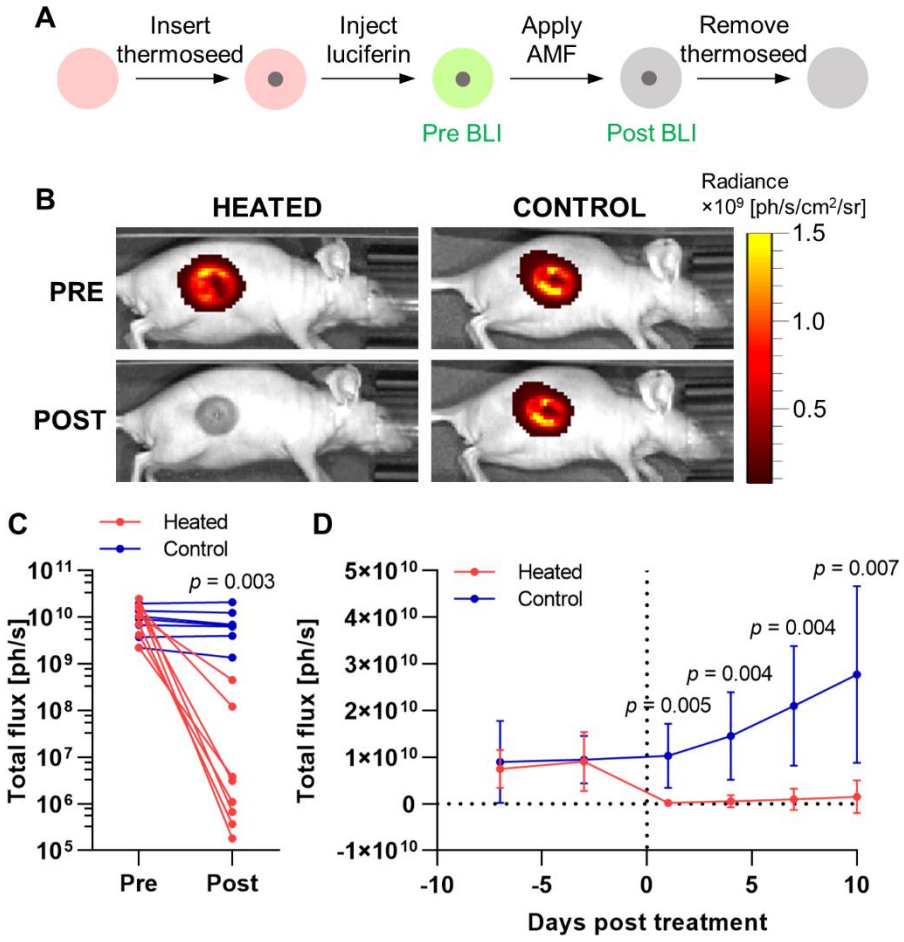

Figure 7.9 Final subcutaneous tumour thermal ablation study. A Schematic outlining the thermal ablation procedure. The thermoseed was inserted prior to the luciferin injection. Ablation was performed with a 2 mm thermoseed, and the alternating magnetic field (8 kA m^{-1}, 710 kHz) was applied for 5 × 1 minutes. Bioluminesence images were acquired at two stages of the procedure. **B** Bioluminescence images of a representative tumour acquired immediately prior to and following heating and a non-heated control tumour, with a thermoseed in place. **C** BLI signal integrated over the whole tumour for all animals, acquired pre and post heating. (Heated, n = 8; control, n = 7) **D** BLI signal measured longitudinally for treated and control animals, acquired with the thermoseed removed. (Heated, n = 6; Control, n = 7).

In the treated animals, a marked decrease in signal intensity was observed across the tumour immediately following heating, from 1.2 × 10^{10} ph s^{-1} to 7.2 × 10^{7} (Figure 7.9B, C). In contrast, no change in signal was recorded in the control group. Over the 10 days following treatment, the BLI signal detected in the heated group increased marginally, remaining at less than 17 % of its pre-treatment value (Figure 7.9D). In addition, tumour volume decreased continuously (Figure 7.10A).

Both BLI signal and tumour volume continued to rise steadily in the control animals, creating a clear difference between the two groups. Some treated animals were followed until 33 days after treatment and showed complete ablation of the tumour bulk (Figure 7.10B). Throughout the experiments animals in both the treatment and control groups maintained a healthy weight (Figure 7.10C). Collectively these data are consistent with my hypothesis, that thermoseed heating can deliver effective thermal ablation and induce cell death in vivo.

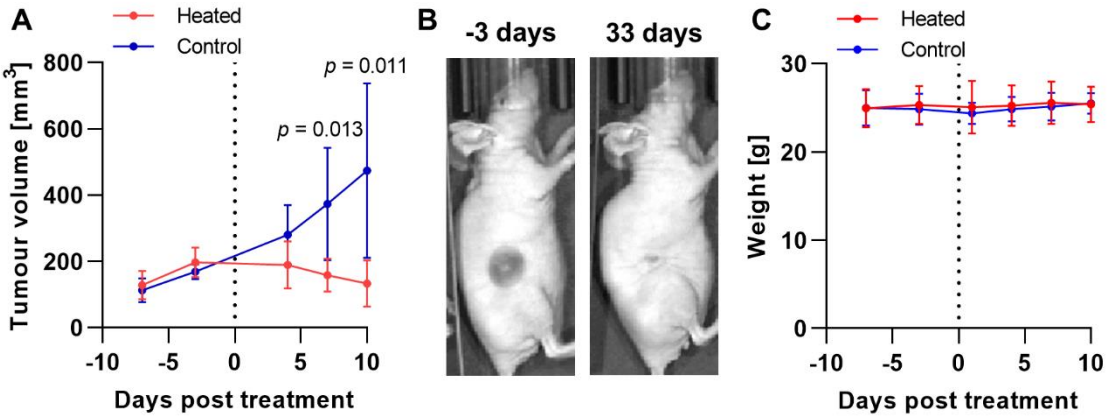

Figure 7.10 Tumour volume data from final subcutaneous tumour heating study. A Tumour volume measurement recorded over the course of the experiment. (Heated, n = 6; control, n = 7). **B** Photographs of a treated tumour 3 days prior to and 33 days post treatment show complete ablation of the tumour bulk. **C** Animal weights remained constant throughout the study.

7.4 Discussion

In this study, spherical, ferromagnetic thermoseeds were heated in vivo using a bespoke, MR-compatible heating coil, to successfully induce cell death in diseased and healthy tissue. Initial experiments conducted in the rat brain showed how distinct regions of cell death were induced following 1 minute of heating under physiological conditions. In addition, distant tissue, in the hemisphere opposite to the thermoseed, was unaffected. Thermal ablation in a subcutaneous tumour model in mice was effective using 1.5 and 2 mm thermoseeds heated for 1 – 5 minutes. When heated for less than 5 minutes, clearly defined regions of cell death were visible in histologically processed tumour sections. With 5 minutes of heating, the entire tumour was ablated. These data demonstrate how thermoseed heating can be performed efficiently in vivo, with the ablation volume controlled by varying thermoseed size or heating

duration, and that thermal ablation performed in this manner was effective as a cancer therapy the animal model used.

Bioluminescence imaging was used throughout the study to monitor tumour growth and access cell viability following treatment. In preliminary experiments, the BLI signal was extremely variable, which made it difficult to isolate and identify any changes in signal specifically caused by thermoseed heating. Subsequently, imaging was only performed at two stages of the treatment process, rather than four, before and after heating with the thermoseed in place. When a 1.5 mm thermoseed was heated for 1 minute, a slight decrease in signal was observed following heating, which can be explained by the small ablation volume observed upon histological examination. On the contrary, when the protocol was adapted to ease thermoseed insertion, allowing 2 mm thermoseeds to be used, the BLI signal repeatably increased following heating. This was unexpected, as a 2 mm thermoseed should induce a larger volume of cell death, as confirmed with histology, which would lead to a decrease in the BLI signal. This result is most likely due to mild hyperthermia in the tissue surrounding the ablated volume. A small increase in temperature may lead to processes that would increase the BLI signal, including vasodilation, which would increase delivery of luciferin; increased metabolism (Clarke and Fraser, 2004; Gillooly *et al.*, 2001); and a shift in the emission spectrum of the luciferase (Zhao *et al.*, 2005). For the final study, changes were made to the experimental protocol to help manage these possible causes. First, the animal was anaesthetised and the thermoseed inserted prior to luciferin injection; this allowed the animal's temperature to be controlled at all stages of the experiment, by keeping the animal on a heat mat or in the temperature-controlled imaging chamber. In addition, the heating duration was increased to 5 minutes, with the aim of increasing the ablation volume to cover the entire tumour. The changes made following each of the preliminary experiments lead to a final protocol that could effectively measure the immediate cell death caused by thermoseed heating.

To date, AMF-based thermal ablation studies have focused on the use of rod-shaped thermoseeds positioned in arrays; this work, alternatively, uses a single spherical ferromagnetic thermoseed. Since MINIMA aims to navigate the thermoseed through tissue to deliver thermal ablation at distinct separate

locations, a spherical thermoseed is advantageous, as it can be easily steered in any direction. An elongated thermoseed would align with the magnetic field of the MRI scanner, thus inhibiting motion in the plane orthogonal to the B_0 axis. Similarly, when using rod-shaped thermoseeds, their orientation with respect to the AMF can affect their heating ability, with larger temperature increases observed with thermoseeds parallel with the AMF (Tompkins *et al.*, 1992). A spherical thermoseed once again eliminates this restriction. Despite using a single thermoseed, the effect observed in this study was profound compared to other preclinical examples. Heating for 5 minutes in total, the entirety of the tumour was ablated, as confirmed visually (since no tumour bulk remained 33 days post treatment) and using BLI. In comparison, when two 0.9 mm diameter, 1.04 cm rod-shaped thermoseeds were heated in subcutaneous tumours for 20 minutes, the tumour size stabilised for just 1 week post treatment, before continuing to increase (Xia *et al.*, 2011).

This work shows how heating ferromagnetic thermoseeds using an MR-compatible heating coil is effective as a cancer therapy, however, further work is necessary to combine the heating component with the imaging and navigation, including development of the MACH system. Although the coil used in this study is MR-compatible, as it does not contain any ferromagnetic components, it would need to be adapted to be able to image the sample or animal within it e.g., by separating the windings to create an imaging window at the centre or adapting the design to allow RF to pass through without affecting the imaging quality. Another limitation of this study is the tumour model used. Although this data does show that thermoseed heating can deliver effective thermal ablation in vivo, a subcutaneous tumour model was used with a single cancer cell line. Repeating experiments with different cancer cell lines and using an orthotopic tumours, which are typically more perfused compared with subcutaneous tumours (Zhang *et al.*, 2019), may provide additional insight into the efficacy of MINIMA as a cancer therapy. Further work may also include optimisation of the thermoseed, by changing the thermoseed material or adding a surface coating that may improve heating performance.

Overall, thermoseed heating in vivo was effective in delivering focal thermal ablation. Using spherical chrome steel thermoseeds, in combination with a

bespoke MR-compatible heating coil, thermal ablation was delivered efficiently and was demonstrated to be effective as a cancer therapy. This study constitutes the final of the three core components of MINIMA, and alongside the imaging and navigation experiments presented in chapters 4 and 5, it demonstrates the potential to elevate an MRI scanner from a diagnostic to a theranostic tool.

8 Final discussion

This thesis introduces MINIMA, a minimally invasive cancer therapy that uses an MRI scanner to navigate a ferromagnetic thermoseed through the body, before delivering localised thermal ablation. Through a series of proof-of-concept studies, the key project components, imaging, navigation, and heating, have been investigated to assess the efficacy of the MINIMA concept. In chapter 4, the preclinical 9.4 T MRI scanner in CABI was setup to facilitate imaging and navigation of thermoseeds. Also, a pulse sequence designed for thermoseed tracking was implemented and validated and subsequently adapted to incorporate propulsion gradient pulses. Chapter 5 demonstrated the use of this pulse sequence, with thermoseed navigation performed in a viscous medium and ex vivo liver tissue. Finally, chapters 6 and 7 focused on the therapeutic component of MINIMA, thermal ablation of tissue via remote thermoseed heating. Initially, thermoseed heating was characterised in vitro, before the therapeutic effect was assessed in vivo, using a murine cancer model.

One of the initial challenges with the MINIMA concept is imaging a ferromagnetic thermoseed using MRI. Due to the magnetic properties of the thermoseed, large artefacts appear in images acquired with typical MRI sequences, which manifest as large areas of signal loss and severe distortion. Despite these challenges, MS-SET, a technique developed to track ferromagnetic spheres by Martel's group (Felfoul *et al.*, 2008; Felfoul *et al.*, 2009), has been shown to be highly accurate. This method was, therefore, implemented and validated on the preclinical MRI scanner in CABI, with the thermoseed's location determined with an accuracy of 0.3 mm, which is comparable to validation results reported in the literature. Looking ahead, this method would form just one part of the imaging pipeline required for MINIMA, which would need pre-acquired images to be registered with intraoperative images, to allow the thermoseed's location to be accurately overlaid onto the anatomy. This process would add additional error to the entire procedure, and therefore, further experiments should be performed to assess the accuracy of the entire imaging pipeline collectively.

Also discussed in chapter 4 was the issue of safe insertion of the thermoseed into the patient and the scanner bore. As explained in section 4.1, the fringe field of

the main MRI magnet will exert a force on the thermoseed as it passes through into the centre of the scanner, which may cause it to move unexpectedly. To overcome this, the thermoseed may be physically held in place once inserted into the patient, using a catheter for example, or by inserting and removing the thermoseed once the patient is already in position within the bore. Although both feasible, these options still carry some risk if the thermoseed cannot be navigated back to the same location for retrieval. A possible solution, which is assessed using a phantom in section 4.3.4, is to switch off the main magnetic field of the MRI scanner. This would make insertion and removal of the thermoseed easier, as well as enabling quicker and easier access to the patient should a problem arise during the procedure. Although MRI scanners that can ramp from zero field up to 9.4 T are available preclinically, this technology is not standard for clinical systems. However, we have been informed, in a personal communication with engineers at Tesla Engineering Ltd., that current technology would allow a clinical MRI scanner to be ramped from 0 to 1.5 T within 45 minutes. This is time-consuming and would be too long to incorporate into a surgical procedure, but if there was a need for such scanners in the future, it is likely that this time could be reduced. Furthermore, the preclinical, rampable scanners designed by MR Solutions Ltd. are cryogen-free, and since Helium is a limited resource, this provides clear motivation to translate this technology into the clinic.

In chapter 5, thermoseed navigation was investigated in a series of experiments, which turned out to be the most challenging aspect of the project. In the studies performed by our group to date, the data show that it is possible to navigate a ferromagnetic thermoseed through brain tissue using a gradient strength of 300 mT m^{-1}. Since magnetic field gradients of this strength are already achievable using clinical gradient coils such as the Connectome, this is a promising result for the technique. However, when attempting navigation in stiffer tissues, such as the liver, thermoseed movement is limited. Therefore, for MINIMA to be a therapy applicable to multiple organs, gradient coils specially designed for propulsion would need to be developed. It may also be preferable to have two separate gradient coils for imaging and propulsion since they would require different specifications. For example, imaging gradient coils require fast switching, whereas a propulsion gradient could be ramped up over several seconds, rather than microseconds. Finally, tissue penetration maybe also be improved through

optimisation of the thermoseed, specifically its material and shape. The development of the thermoseed for this application would be of great value in the next stages of the MINIMA project.

The final component of MINIMA is the heating, which was presented in chapters 6 and 7. Collectively the data demonstrate the ability to rapidly heat a ferromagnetic thermoseed to temperatures > 70 °C using an MR-compatible heating coil, which was shown to be effective as a cancer therapy in a murine subcutaneous tumour model. For the experiments presented in this thesis, the heating coil was developed by collaborator Paul Southern from Resonant Circuits limited, and although the coil could be run within the MRI scanner bore safely, the design prohibited the ability to image, navigate and heat within the same session, primarily due to the limited space within the preclinical scanner. Going forward, in continued collaboration with Paul, a modified coil will be developed that could be used on a clinical MRI scanner. This would provide more space to work in and allow image quality to be assessed with the heating coil in place. Furthermore, with this modified set up the three components of the project may be brought together and performed collectively, thus demonstrating the entire MINIMA concept in a single experiment, which would be essential for the next stages of development.

Although the use of a preclinical MRI scanner was appealing at the start of this project, primarily due to the large gradient strengths that can be achieved in comparison to a clinical system, the set up was not without its limitations. While positive results were obtained for navigation through brain tissue, the gradients were still insufficient when navigating through denser tissues, with very limited movement observed in ex vivo liver tissue. In addition, and perhaps the most limiting aspect, is the small bore of the scanner, which affected the project in multiple ways. First, the combination of the small imaging volume and the large artefact induced by the thermoseed meant that thermoseeds > 3 mm in diameter could not be used at all, as most of the image would experience complete loss of signal. For the navigation experiments, tissue samples were limited to small sections contained within a box, which may have affected the tissue properties. With a larger volume to work in, larger sections or whole organs may have been used. Finally, heating experiments were unable to be performed in the scanner

at the same time as imaging and navigation, as the RF and heating coils would not fit in the bore at the same time. With these considerations, any future work should be moved to a system designed for larger animals or humans, which would allow these additional experiments to be performed with greater ease. Specific experiments that should be performed include accuracy assessment of the full imaging pipeline, including registration between pre and intraoperative images and the thermoseed location; navigation in a larger variety of tissues, across greater distances in brain tissue and in vivo; and bringing all three project components together in a single experiment.

Taken together, the work presented throughout the chapters of this thesis show potential for MINIMA as a minimally invasive cancer therapy. However, it cannot be denied that engineering challenges need to be overcome in multiple aspects of the project, possibly including a rampable magnet, gradient coils, and a clinical MR-compatible heating coil. Consequently, it would not be as simple as implementing a new therapy using the existing infrastructure provided by an MRI scanner; this would make translation into the clinic challenging and would require collaboration from a range of disciplines, as well as input from industry partners. Furthermore, if alterations do need to be made to a typical clinical MRI scanner, perhaps alternative modalities would provide a better platform to start from. For example, a CT scanner wouldn't pose the same problems in terms of imaging as the MRI scanner, since the artefact from the thermoseed is much smaller and has less impact across the entire image. And although CT soft tissue contrast is poor, CT – MRI registration is an area of ongoing research (Roy *et al.*, 2014; Fu *et al.*, 2020), with methods regularly used for radiotherapy planning (Rosenman *et al.*, 1998). Using alternative imaging modalities isn't without its own challenges, for example the thermoseed wouldn't be magnetised, thus requiring a permanent magnet to be used, but alternative imaging options would be important to consider when going forward with this project.

Considering the developments and challenges discussed, a large investment in both time and money would be required for a novel technique such as MINIMA to be translated into the clinic. And when considering the cost/benefit ratio, its greatest chance of success would depend on a clear clinical need for the technology. As brain cancer is a common cancer, with a 5 year survival rate of

just 12 % in the UK (Cancer Research UK, 2022), there is a continuous drive for new treatments, and the work presented in this thesis demonstrates the potential of MINIMA to deliver on this need.

To conclude, in this thesis preliminary experiments have been performed to assess the efficacy of a novel cancer therapy, MINIMA. Having completed these experiments, it is clear that the project faces many challenges if it is to be successful, primarily in the development of hardware such as gradient and heating coils. Nonetheless, the presented data does show potential for a minimally invasive, image-guided ablation therapy, that may be delivered with precision using an MRI scanner.

9 References

boussouan, E. and Martel, S. 'High-precision absolute positioning of medical instruments in MRI systems'. *International Conference of the IEEE Engineering in Medicine and Biology Society*, New York City, USA, 30 August - 3 September 2006, 743-746.

Alkins, R. D. and Mainprize, T. G. (2018) 'High-Intensity Focused Ultrasound Ablation Therapy of Gliomas', in Chernov, M.F., Muragaki, Y., Kesari, S. and McCutcheon, I.E. (eds.) *Intracranial Gliomas Part III - Innovative Treatment Modalities*. Basel: Karger, pp. 39-47.

Atkinson, W. J., Brezovich, I. A. and Chakraborty, D. P. (1984) 'Usable frequencies in hyperthermia with thermal seeds', *IEEE Transactions on Biomedical Engineering,* 31(1), pp. 70-75.

Azizi, A., Tremblay, C. C., Gagne, K. and Martel, S. (2019) 'Using the fringe field of a clinical MRI scanner enables robotic navigation of tethered instruments in deeper vascular regions', *Science Robotics,* 4(36), pp. eaax7342.

Baker, R. R., Payne, C., Yu, Y., Mohseni, M., Connell, J. J., Lin, F., Harrison, I. F., Southern, P., Rudrapatna, U. S., Stuckey, D. J., Kalber, T. L., Siow, B., Thorne, L., Punwani, S., Jones, D. K., Emberton, M., Pankhurst, Q. A. and Lythgoe, M. F. (2022) 'Image-guided Magnetic Thermoseed Navigation and Tumor Ablation Using an MRI System', *Advanced Science,* 9, pp. 2105333.

Becker, A. T., Felfoul, O. and Dupont, P. E. 'Toward Tissue Penetration by MRI-powered Millirobots Using a Self-Assembled Gauss Gun'. *IEEE International Conference on Robotics and Automation (ICRA)*. *IEEE International Conference on Robotics and Automation*, Seattle, Washington, USA, 26-30 May, 1184-1189.

Bernstein, M. A., King, K. F. and Zhou, X. J. (2004) *Handbook of MRI pulse sequences.* Boston: Academic Press.

Bloch, F. (1946) 'Nuclear induction', *Physical Review,* 70(7-8), pp. 460-474.

Brezovich, I. A., Atkinson, W. J. and Chakraborty, D. P. (1984) 'Temperature distributions in tumor models heated by self-regulating nickel–copper alloy thermoseeds', *Medical Physics,* 11(2), pp. 145-152.

Brown, R. W. (2014) *Magnetic Resonance Imaging: Physical Principles and Sequence Design.* 2nd ed.. edn.: Newark, NJ: Wiley.

Bruker (2021) *BioSpec 70/20 and 94/20*. Available at: https://www.bruker.com/en/products-and-solutions/preclinical-imaging/mri/biospec/biospec-70-20-and-94-20.html (Accessed: 10 November 2021).

Bulte, J. W. M. and Kraitchman, D. L. (2004) 'Iron oxide MR contrast agents for molecular and cellular imaging', *Nmr in Biomedicine,* 17(7), pp. 484-499.

Burton, C., Hill, M. and Walker, A. E. (1971) 'The RF Thermoseed-A Thermally Self-Regulating Implant for the Production of Brain Lesions', *IEEE Transactions on Biomedical Engineering,* 18(2), pp. 104-109.

Cancer Research UK (2022) *Brain, other CNS and intracranial tumours survival statistics*. Available at: https://www.cancerresearchuk.org/health-professional/cancer-statistics/statistics-by-cancer-type/brain-other-cns-and-intracranial-tumours/survival#heading-Zero (Accessed: 12 January 2022).

Carpi, F. and Pappone, C. (2009) 'Stereotaxis Niobe (R) magnetic navigation system for endocardial catheter ablation and gastrointestinal capsule endoscopy', *Expert Review of Medical Devices,* 6(5), pp. 487-498.

Cetas, T. C., Gross, E. J. and Contractor, Y. (1998) 'A ferrite core metallic sheath thermoseed for interstitial thermal therapies', *IEEE Transactions on Biomedical Engineering,* 45(1), pp. 68-77.

Chanu, A., Felfoul, O., Beaudoin, G. and Martell, S. (2008) 'Adapting the clinical MRI software environment for real-time navigation of an endovascular untethered ferromagnetic bead for future endovascular interventions', *Magnetic Resonance in Medicine,* 59(6), pp. 1287-1297.

Chanu, A. and Martel, S. 'Real-time software platform design for in-vivo navigation of a small ferromagnetic device in a swine carotid artery using a magnetic resonance imaging system'. *International Conference of the IEEE Engineering in Medicine and Biology Society*, Lyon, France, 23 - 26 August, 6584 - 6587.

Cho, Z. H., Kim, D. J. and Kim, Y. K. (1988) 'Total inhomogeneity correction including chemical shifts and susceptibility by view angle tilting', *Medical Physics,* 15(1), pp. 7-11.

Chu, K. F. and Dupuy, D. E. (2014) 'Thermal ablation of tumours: biological mechanisms and advances in therapy', *Nature Reviews Cancer,* 14(3), pp. 199-208.

Clarke, A. and Fraser, K. P. P. (2004) 'Why does metabolism scale with temperature?', *Functional Ecology,* 18(2), pp. 243-251.

Coey, J. M. D. (2009) *Magnetism and magnetic materials.* Cambridge: Cambridge University Press.

Daniels, E. W., Cole, D., Jacobs, B. and Phillips, S. F. (2018) 'Existing Evidence on Ultrasound-Guided Injections in Sports Medicine', *Orthopaedic Journal of Sports Medicine,* 6(2), pp. 2325967118756576.

Deger, S., Boehmer, D., Turk, I., Roigas, J., Budach, V. and Leoning, S. A. (2002) 'Interstitial hyperthermia using self-regulating thermoseeds combined with conformal radiation therapy', *European Urology,* 42(2), pp. 147-153.

Deger, S., Taymoorian, K., Boehmer, D., Schink, T., Roigas, J., Wille, A. H., Budach, V., Wernecke, K. D. and Loening, S. A. (2004) 'Thermoradiotherapy using interstitial self-regulating thermoseeds: An intermediate analysis of a phase II trial', *European Urology,* 45(5), pp. 574-580.

Deroulers, C., Ameisen, D., Badoual, M., Gerin, C., Granier, A. and Lartaud, M. (2013) 'Analyzing huge pathology images with open source software', *Diagnostic Pathology,* 8(1), pp. 92.

Diana, M., Schiraldi, L., Liu, Y. Y., Memeo, R., Mutter, D., Pessaux, P. and Marescaux, J. (2016) 'High intensity focused ultrasound (HIFU) applied to hepato-biliopancreatic and the digestive system - current state of the art and future perspectives', *Hepatobiliary Surgery and Nutrition,* 5(4), pp. 329-344.

Drake, J. M., Gabriel, C. L. and Henry, M. D. (2005) 'Assessing tumor growth and distribution in a model of prostate cancer metastasis using bioluminescence imaging', *Clinical & Experimental Metastasis,* 22(8), pp. 674-684.

Enochs, W. S., Harsh, G., Hochberg, F. and Weissleder, R. (1999) 'Improved delineation of human brain tumors on MR images using a long-circulating, superparamagnetic iron oxide agent', *Jmri-Journal of Magnetic Resonance Imaging,* 9(2), pp. 228-232.

Estelrich, J., Sanchez-Martin, M. J. and Busquets, M. A. (2015) 'Nanoparticles in magnetic resonance imaging: from simple to dual contrast agents', *International Journal of Nanomedicine,* 10, pp. 1727-1741.

Eustace, S., Goldberg, R., Williamson, D., Melhem, E. R., Oladipo, O., Yucel, E. K. and Jara, H. (1997) 'MR imaging of soft tissues adjacent to orthopaedic hardware: Techniques to minimize susceptibility artefact', *Clinical Radiology,* 52(8), pp. 589-594.

Felfoul, O., Aboussouan, E., Chanu, A. and Martel, S. 'Real-time positioning and tracking technique for endovascular untethered microrobots propelled by MRI gradients'. *IEEE International Conference on Robotics and Automation ICRA*. *IEEE International Conference on Robotics and Automation*, Kobe, Japan, 12-17 May, 2693-2698.

Felfoul, O., Mathieu, J. B., Beaudoin, G. and Martel, S. (2008) 'In vivo MR-tracking based on magnetic signature selective excitation', *IEEE Transactions on Medical Imaging,* 27(1), pp. 28-35.

Folio, D. and Ferreira, A. (2017) 'Two-Dimensional Robust Magnetic Resonance Navigation of a Ferromagnetic Microrobot Using Pareto Optimality', *Ieee Transactions on Robotics,* 33(3), pp. 583-593.

Fu, Y. B., Lei, Y., Zhou, J., Wang, T. H., Yu, D. S., Beitler, J. J., Curran, W. J., Liu, T. and Yang, X. F. (2021) 'Synthetic CT-aided MRI-CT Image Registration for Head and neck Radiotherapy'. *Progress in Biomedical Optics and Imaging*. *SPIE Medical Imaging Conference*, Houston, TX, Feb 15-20.

Geng, Y. C., Wang, X. X., Ma, Y., Hu, Y. and Zhang, R. L. (1998) 'Orientated thermotherapy of ferromagnetic thermoseed in hepatic tumors', *World Journal of Gastroenterology,* 4(4), pp. 326-328.

Gillooly, J. F., Brown, J. H., West, G. B., Savage, V. M. and Charnov, E. L. (2001) 'Effects of size and temperature on metabolic rate', *Science,* 293(5538), pp. 2248-2251.

Gosselin, F. P., Lalande, V. and Martel, S. (2011) 'Characterization of the deflections of a catheter steered using a magnetic resonance imaging system', *Medical Physics,* 38(9), pp. 4994-5002.

Grady, M. S., Howard, M. A., Broaddus, W. C., Molloy, J. A., Ritter, R. C., Quate, E. G. and Gillies, G. T. (1990) 'Magnetic stereotaxis - A technique to deliver stereotaxic hyperthermia', *Neurosurgery,* 27(6), pp. 1010-1016.

Griffiths, D. J. (2017) *Introduction to Electrodynamics.* 4 edn. Cambridge: Cambridge University Press.

Hargreaves, B. A., Taviani, V., Litwiller, D. V. and Yoon, D. (2018) '2D multi-spectral imaging for fast MRI near metal', *Magnetic Resonance in Medicine,* 79(2), pp. 968-973.

Hasgall, P. A., Di Gennaro, F., Baumgartner, C., Neufeld, E., Lloyd, B., Gosselin, M. C., Payne, D., Klingenböck, A. and Kuster, N. IT’IS Database for thermal and electromagnetic parameters of biological tissues. 15 May 2018 ed.

Hergt, R. and Dutz, S. (2007) 'Magnetic particle hyperthermia-biophysical limitations of a visionary tumour therapy', *Journal of Magnetism and Magnetic Materials,* 311(1), pp. 187-192.

Hilger, I. (2013) 'In vivo applications of magnetic nanoparticle hyperthermia', *International Journal of Hyperthermia,* 29(8), pp. 828-834.

Hong, K. and Georgiades, C. (2010) 'Radiofrequency Ablation: Mechanism of Action and Devices', *Journal of Vascular and Interventional Radiology,* 21(8), pp. S179-S186.

Iddan, G., Meron, G., Glukhovsky, A. and Swain, P. (2000) 'Wireless capsule endoscopy', *Nature,* 405(6785), pp. 417-417.

Illing, R. and Emberton, M. (2006) 'Sonablate (R)-500: transrectal high-intensity focused ultrasound for the treatment of prostate cancer', *Expert Review of Medical Devices,* 3(6), pp. 717-729.

Kalinyak, J. E., Schilling, K., Berg, W. A., Narayanan, D., Mayberry, J. P., Rai, R., DuPree, E. B., Shusterman, D. K., Gittleman, M. A., Luo, W. D. and Matthews, C. G. (2011) 'PET-Guided Breast Biopsy', *Breast Journal,* 17(2), pp. 143-151.

Korchinski, D. J., Taha, M., Yang, R. Z., Nathoo, N. and Dunn, J. F. (2015) 'Iron Oxide as an MRI Contrast Agent for Cell Tracking', *Magnetic Resonance Insights,* 8(S1), pp. 15-29.

Krieger, A., Song, S. E., Cho, N. B., Iordachita, II, Guion, P., Fichtinger, G. and Whitcomb, L. L. (2013) 'Development and Evaluation of an Actuated MRI-Compatible Robotic System for MRI-Guided Prostate Intervention', *IEEE-ASME Transactions on Mechatronics,* 18(1), pp. 273-284.

Lalande, V., Gosselin, F. P., Vonthron, M., Conan, B., Tremblay, C., Beaudoin, G., Soulez, G. and Martel, S. (2015) 'In vivo demonstration of magnetic guidewire steerability in a MRI system with additional gradient coils', *Medical Physics,* 42(2), pp. 969-976.

Latulippe, M. and Martel, S. (2015) 'Dipole Field Navigation: Theory and Proof of Concept', *IEEE Transactions on Robotics,* 31(6), pp. 1353-1363.

Latulippe, M. and Martel, S. (2018) 'Evaluation of the Potential of Dipole Field Navigation for the Targeted Delivery of Therapeutic Agents in a Human Vascular Network', *IEEE Transactions on Magnetics,* 54(2), pp. 5600112.

Leclerc, J., Ramakrishnan, A., Tsekos, N. V. and Becker, A. T. (2018) 'Magnetic hammer actuation for tissue penetration using a millirobot', *IEEE Robotics and Automation Letters,* 3(1), pp. 403-410.

Lecornet, E., Moore, C., Ahmed, H. U. and Emberton, M. (2010) 'Focal therapy for prostate cancer: Fact or fiction?', *Urologic Oncology,* 28(5), pp. 550-556.

Lee, N., Kim, H., Choi, S. H., Park, M., Kim, D., Kim, H. C., Choi, Y., Lin, S., Kim, B. H., Jung, H. S., Kim, H., Park, K. S., Moon, W. K. and Hyeon, T. (2011) 'Magnetosome-like ferrimagnetic iron oxide nanocubes for highly sensitive MRI of single cells and transplanted pancreatic islets', *Proceedings of the National Academy of Sciences of the United States of America,* 108(7), pp. 2662-2667.

Levitt, M. H. (2001) *Spin dynamics : basics of nuclear magnetic resonance.* Chichester: John Wiley & Sons.

Lim, P. C. Y., Toh, J. J. H., Loh, J., Lee, E. C. Y., Chong, D. T. T., Tan, B. Y., Ho, K. L., Ching, C. K. and Teo, W. S. (2017) 'Remote magnetic catheter navigation versus conventional ablation in atrial fibrillation ablation: Fluoroscopy reduction', *Journal of Arrhythmia,* 33(3), pp. 167-171.

Maier-Hauff, K., Rothe, R., Scholz, R., Gneveckow, U., Wust, P., Thiesen, B., Feussner, A., von Deimling, A., Waldoefner, N., Felix, R. and Jordan, A. (2007) 'Intracranial thermotherapy using magnetic nanoparticles combined with external beam radiotherapy: Results of a feasibility study on patients with glioblastoma multiforme', *Journal of Neuro-Oncology,* 81(1), pp. 53-60.

Martel, S. (2013) 'Combining Pulsed and DC Gradients in a Clinical MRI-Based Microrobotic Platform to Guide Therapeutic Magnetic Agents in the Vascular Network', *International Journal of Advanced Robotic Systems,* 10(30).

Martel, S., Felfoul, O., Mathieu, J. B., Chanu, A., Tamaz, S., Mohammadi, M., Mankiewicz, M. and Tabatabaei, N. (2009) 'MRI-based Medical Nanorobotic Platform for the Control of Magnetic Nanoparticles and Flagellated Bacteria for Target Interventions in Human Capillaries', *International Journal of Robotics Research,* 28(9), pp. 1169-1182.

Martel, S., Mathieu, J. B., Felfoul, O. and Beaudoin, G. (2015) *MR-tracking based on magnetic signature selective excitation*. [Online].

Martel, S., Mathieu, J. B., Felfoul, O., Chanu, A., Aboussouan, E., Tamaz, S. and Pouponneau, P. (2007) 'Automatic navigation of an untethered device in the artery of a living animal using a conventional clinical magnetic resonance imaging system', *Applied Physics Letters,* 90(11), pp. 114105.

Martinez-Fernandez, R., Rodriguez-Rojas, R., del Alamo, M., Hernandez-Fernandez, F., Pineda-Pardo, J. A., Dileone, M., Alonso-Frech, F., Foffani, G., Obeso, I., Gasca-Salas, C., de Luis-Pastor, E., Vela, L. and Obeso, J. A. (2018) 'Focused ultrasound subthalamotomy in patients with asymmetric Parkinson's disease: a pilot study', *Lancet Neurology,* 17(1), pp. 54-63.

Masamune, K., Kobayashi, E., Masutani, Y., Suzuki, M., Dohi, T., Iseki, H. and Takakura, K. (1995) 'Development of an MRI-compatible needle insertion manipulator for stereotactic neurosurgery', *Journal of Image Guided Surgery,* 1(4), pp. 242-248.

Mathieu, J. B., Beaudoin, G. and Martel, S. (2006) 'Method of propulsion of a ferromagnetic core in the cardiovascular system through magnetic gradients generated by an MRI system', *IEEE Transactions on Biomedical Engineering,* 53(2), pp. 292-299.

Mathieu, J. B. and Martel, S. (2007) 'Magnetic microparticle steering within the constraints of an MRI system: proof of concept of a novel targeting approach', *Biomedical Microdevices,* 9(6), pp. 801-808.

Mathieu, J. B., Martel, S., Yahia, L., Soulez, G. and Beaudoin, G. (2005) 'Preliminary investigation of the feasibility of magnetic propulsion for future

microdevices in blood vessels', *Bio-Medical Materials and Engineering,* 15(5), pp. 367-374.

Mathieu, J. B., Martel, S., Yahia, L. H., Soulez, G., Beaudoin, G. and Ieee 'MRI systems as a mean of propulsion for a microdevice in blood vessels', *Proceedings of the 25th Annual International Conference of the Ieee Engineering in Medicine and Biology Society, Vols 1-4: A New Beginning for Human Health*, 3419-3422.

McGahan, J. P. and Dodd, G. D. (2001) 'Radiofrequency ablation of the liver: Current status', *American Journal of Roentgenology,* 176(1), pp. 3-16.

McRobbie, D. W., Moore, E. A., Graves, M. J. and Prince, M. R. (2006) *MRI from Picture to Proton.* 3rd edn.: Cambridge University Press.

Meijerink, M. R., van den Tol, P., van Tilborg, A., van Waesberghe, J., Meijer, S. and van Kuijk, C. (2011) 'Radiofrequency ablation of large size liver tumours using novel plan-parallel expandable bipolar electrodes: Initial clinical experience', *European Journal of Radiology,* 77(1), pp. 167-171.

Molloy, J. A., Ritter, R. C., Grady, M. S., Howard, M. A., Quate, E. G. and Gillies, G. T. (1990) 'Experimental determination of the force required for insertion of a thermoseed into deep brain tissues', *Annals of Biomedical Engineering,* 18(3), pp. 299-313.

Mouratidis, P. X. E., Rivens, I. and ter Haar, G. (2015) 'A study of thermal dose-induced autophagy, apoptosis and necroptosis in colon cancer cells', *International Journal of Hyperthermia,* 31(5), pp. 476-488.

MR Solutions (2021) *MRS*DRYMAG: 3T-4.7T-7T-9.4T*. Available at: https://www.mrsolutions.com/mr-imaging/mr-imaging/mr-dry-magnet-cryogen-free/ (Accessed: 9 November 2021).

Muthana, M., Kennerley, A. J., Hughes, R., Fagnano, E., Richardson, J., Paul, M., Murdoch, C., Wright, F., Payne, C., Lythgoe, M. F., Farrow, N., Dobson, J., Conner, J., Wild, J. M. and Lewis, C. (2015) 'Directing cell therapy to anatomic

target sites in vivo with magnetic resonance targeting', *Nature Communications,* 6, pp. 8009.

Nikfarjam, M., Muralidharan, V. and Christophi, C. (2005) 'Mechanisms of focal heat destruction of liver tumors', *Journal of Surgical Research,* 127(2), pp. 208-223.

Ouyang, W. W., Gao, F. P., Wang, L. F., Xie, X. X., Lei, F. L., Zhou, J. M., Liao, Y. P., Zhong, M. Z. and Tang, J. T. (2010) 'Thermoseed hyperthermia treatment of mammary orthotopic transplantation tumors in rats and impact on immune function', *Oncology Reports,* 24(4), pp. 973-979.

Pane, S., Puigmarti-Luis, J., Bergeles, C., Chen, X. Z., Pellicer, E., Sort, J., Pocepcova, V., Ferreira, A. and Nelson, B. J. (2019) 'Imaging Technologies for Biomedical Micro- and Nanoswimmers', *Advanced Materials Technologies,* 4(4).

Pankhurst, Q. A., Connolly, J., Jones, S. K. and Dobson, J. (2003) 'Applications of magnetic nanoparticles in biomedicine', *Journal of Physics D: Applied Physics,* 36(13), pp. R167-R181.

Pankhurst, Q. A., Thanh, N. T. K., Jones, S. K. and Dobson, J. (2009) 'Progress in applications of magnetic nanoparticles in biomedicine', *Journal of Physics D: Applied Physics,* 42, pp. 224001.

Patel, B. and Kim, A. H. (2020) 'Laser Interstitial Thermal Therapy', *Missouri medicine,* 117(1), pp. 50-55.

Patel, N. A., Nycz, C. J., Carvalho, P. A., Gandomi, K. Y., Gondokaryono, R., Li, G., Heffter, T., Burdette, E. C., Pilitsis, J. G. and Fischer, G. S. (2020) 'An Integrated Robotic System for MRI-Guided Neuroablation: Preclinical Evaluation', *IEEE Transactions on Biomedical Engineering,* 67(10), pp. 2990-2999.

Pollert, E. and Zaveta, K. (2012) 'Nanocrystalline oxides in magnetic fluid hyperthermia', in Thanh, N.T.K. (ed.) *Magnetic nanoparticles: from fabrication to*

clinical applications : theory to therapy, chemistry to clinic, bench to bedside: CRC Press.

Port, J. D. and Pomper, M. G. (2000) 'Quantification and minimization of magnetic susceptibility artifacts on GRE images', *Journal of Computer Assisted Tomography,* 24(6), pp. 958-964.

Pouponneau, P., Leroux, J. C. and Martel, S. (2009) 'Magnetic nanoparticles encapsulated into biodegradable microparticles steered with an upgraded magnetic resonance imaging system for tumor chemoembolization', *Biomaterials,* 30(31), pp. 6327-6332.

Pouponneau, P., Leroux, J. C., Soulez, G., Gaboury, L. and Martel, S. (2011) 'Co-encapsulation of magnetic nanoparticles and doxorubicin into biodegradable microcarriers for deep tissue targeting by vascular MRI navigation', *Biomaterials,* 32(13), pp. 3481-3486.

Prendiville, T. W., Ma, Q., Lin, Z. Q., Zhou, P. Z., He, A. B. and Pu, W. T. (2014) 'Ultrasound-guided Transthoracic Intramyocardial Injection in Mice', *Journal of Visualized Experiments,* (90), pp. 51566.

Prince, E., Hakimian, S., Ko, A. L., Ojemann, J. G., Kim, M. S. and Miller, J. W. (2017) 'Laser Interstitial Thermal Therapy for Epilepsy', *Current Neurology and Neuroscience Reports,* 17(9), pp. 63.

Purcell, E. M., Torrey, H. C. and Pound, R. V. (1946) 'Resonance absorption by nuclear magnetic moments in a solid', *Physical Review,* 69(1-2), pp. 37-38.

Quigg, M. and Harden, C. (2014) 'Minimally invasive techniques for epilepsy surgery: stereotactic radiosurgery and other technologies', *Journal of Neurosurgery,* 121(Suppl 2), pp. 232-240.

Reichert, T., Bittner, G., Heinzelmann, K. G., Soldner, L. and Vetter, J. (1988) 'Siemens Helicon: a novel 2 tesla superconducting whole-body MR magnet', *IEEE Transactions on Magnetics,* 24(2), pp. 1272-1275.

Riegler, J., Allain, B., Cook, R. J., Lythgoe, M. F. and Pankhurst, Q. A. (2011) 'Magnetically assisted delivery of cells using a magnetic resonance imaging system', *Journal of Physics D-Applied Physics,* 44(5), pp. 10.

Riegler, J., Wells, J. A., Kyrtatos, P. G., Price, A. N., Pankhurst, Q. A. and Lythgoe, M. F. (2010) 'Targeted magnetic delivery and tracking of cells using a magnetic resonance imaging system', *Biomaterials,* 31(20), pp. 5366-5371.

Rigla, J. P., Bodker, F., Anari, A., Pallás, E., Grau, D., Puchalt, G., González, J. M., Corberán, M., Díaz, E., Algarín, J. M., Ríos, A., Benlloch, J. M. and Alonso, J. (2020) 'Low-Field Rampable Magnet for a High-Resolution MRI System', *IEEE Transactions on Magnetics,* 56(2), pp. 1-7.

Rosenman, J. G., Miller, E. P., Tracton, G. and Cullip, T. J. (1998) 'Image registration: An essential part of radiation therapy treatment planning', *International Journal of Radiation Oncology Biology Physics,* 40(1), pp. 197-205.

Roy, S., Carass, A., Jog, A., Prince, J. L. and Lee, J. (2014) 'MR to CT Registration of Brains using Image Synthesis'. *Proceedings of SPIE*. *Conference on Medical Imaging - Image Processing*, San Diego, CA, Feb 16-18.

Rueden, C. T., Schindelin, J., Hiner, M. C., DeZonia, B. E., Walter, A. E., Arena, E. T. and Eliceiri, K. W. (2017) 'ImageJ2: ImageJ for the next generation of scientific image data', *Bmc Bioinformatics,* 18, pp. 529.

Sadikot, R. T. and Blackwell, T. S. (2005) 'Bioluminescence imaging', *Proceedings of the American Thoracic Society,* 2(6), pp. 537-512.

Schepkin, V. D., Brey, W. W., Gor'kov, P. L. and Grant, S. C. (2010) 'Initial in vivo rodent sodium and proton MR imaging at 21.1 T', *Magnetic Resonance Imaging,* 28(3), pp. 400-407.

Semelka, R. C. and Helmberger, T. K. G. (2001) 'Contrast agents for MR imaging of the liver', *Radiology,* 218(1), pp. 27-38.

Shi, Y. L., Li, N., Tremblay, C. C. and Martel, S. (2021) 'A Piezoelectric Robotic System for MRI Targeting Assessments of Therapeutics During Dipole Field Navigation', *Ieee-Asme Transactions on Mechatronics,* 26(1), pp. 214-225.

Siemens Medical Solutions USA (2021) *MAGNETOM Prisma*. Available at: https://www.siemens-healthineers.com/en-us/magnetic-resonance-imaging/3t-mri-scanner/magnetom-prisma (Accessed: 10 November 2021).

Soto, F., Wang, J., Ahmed, R. and Demirci, U. (2020) 'Medical Micro/Nanorobots in Precision Medicine', *Advanced Science,* 7(21), pp. 2002203.

Stauffer, P. R., Cetas, T. C. and Jones, R. C. (1984) 'Magnetic induction heating of ferromagnetic implants for inducing localized hyperthermia in deep-seated tumors', *IEEE Transactions on Biomedical Engineering,* 31(2), pp. 235-251.

Takahashi, H. and Berber, E. (2020) 'Role of thermal ablation in the management of colorectal liver metastasis', *Hepatobiliary Surgery and Nutrition,* 9(1), pp. 49-58.

Tamaz, S., Gourdeau, R., Chanu, A., Mathieu, J. B. and Martel, S. (2008) 'Real-time MRI-based control of a ferromagnetic core for endovascular navigation', *IEEE Transactions on Biomedical Engineering,* 55(7), pp. 1854-1863.

Tansi, F. L., Maduabuchi, W. O., Hirsch, M., Southern, P., Hattersley, S., Quaas, R., Teichgraber, U., Pankhurst, Q. A. and Hilger, I. (2021) 'Deep-tissue localization of magnetic field hyperthermia using pulse sequencing', *International Journal of Hyperthermia,* 38(1), pp. 743-754.

Thiesen, B. and Jordan, A. (2008) 'Clinical applications of magnetic nanoparticles for hyperthermia', *International Journal of Hyperthermia,* 24(6), pp. 467-474.

Thin, M. Z., Allan, H., Bofinger, R., Kostelec, T. D., Guillaume, S., Connell, J. J., Patrick, P. S., Hailes, H. C., Tabor, A. B., Lythgoe, M. F., Stuckey, D. J. and Kalber, T. L. (2020) 'Multi-modal imaging probe for assessing the efficiency of stem cell delivery to orthotopic breast tumours', *Nanoscale,* 12(31), pp. 16570-16585.

Tompkins, D. T., Partington, B. P., Steeves, R. A., Bartholow, S. D. and Paliwal, B. R. (1992) 'Effect of implant variables on temperatures achieved during ferromagnetic hyperthermia', *International Journal of Hyperthermia,* 8(2), pp. 241-251.

Tovar-Spinoza, Z., Carter, D., Ferrone, D., Eksioglu, Y. and Huckins, S. (2013) 'The use of MRI-guided laser-induced thermal ablation for epilepsy', *Childs Nervous System,* 29(11), pp. 2089-2094.

Tremblay, C., Conan, B., Loghin, D., Bigot, A. and Martel, S. 'Fringe Field Navigation for Catheterization'. *European Conference of the International Federation for Medical and Biological Engineering*, Dubrovnik, Croatia, 7 - 11 September.

Tucker, R. D., Huidobro, C. and Larson, T. (2005) 'Ablation of stage T-1/T-2 prostate cancer with permanent interstitial temperature self-regulating rods', *Journal of Endourology,* 19(7), pp. 865-867.

Tucker, R. D., Huidobro, C., Larson, T. and Platz, C. E. (2000) 'Use of permanent interstitial temperature self-regulating rods for ablation of prostate cancer', *Journal of Endourology,* 14(6), pp. 511-517.

Valerio, M., Emberton, M., Barret, E., Eberli, D., Eggener, S. E., Ehdaie, B., Jichlinski, P., Ward, J. F. and Ahmed, H. U. (2014) 'Health technology assessment in evolution - focal therapy in localised prostate cancer', *Expert Review of Anticancer Therapy,* 14(11), pp. 1359-1367.

van der Poel, H. G., van den Bergh, R. C. N., Briers, E., Cornford, P., Govorov, A., Henry, A. M., Lam, T. B., Mason, M. D., Rouviere, O., De Santis, M., Willemse, P. M., van Poppel, H. and Mottet, N. (2018) 'Focal Therapy in Primary Localised Prostate Cancer: The European Association of Urology Position in 2018', *Eur Urol,* 74(1), pp. 84-91.

van Rhoon, G. C. (2016) 'Is CEM43 still a relevant thermal dose parameter for hyperthermia treatment monitoring?', *International Journal of Hyperthermia,* 32(1), pp. 50-62.

Xia, Q. S., Liu, X. A., Xu, B., Zhao, T. D., Li, H. Y., Chen, Z. H., Xiang, Q., Geng, C. Y., Pan, L., Hu, R. L., Qi, Y. J., Sun, G. F. and Tang, J. T. (2011) 'Feasibility study of high-temperature thermoseed inductive hyperthermia in melanoma treatment', *Oncology Reports,* 25(4), pp. 953-962.

Zhang, K., Krafft, A. J., Umathum, R., Maier, F., Semmler, W. and Bock, M. (2010) 'Real-time MR navigation and localization of an intravascular catheter with ferromagnetic components', *Magnetic Resonance Materials in Physics Biology and Medicine,* 23(3), pp. 153-163.

Zhang, W., Fan, W., Rachagani, S., Zhou, Z., Lele, S. M., Batra, S. K. and Garrison, J. C. (2019) 'Comparative Study of Subcutaneous and Orthotopic Mouse Models of Prostate Cancer: Vascular Perfusion, Vasculature Density, Hypoxic Burden and BB2r-Targeting Efficacy', *Scientific Reports,* 9.

Zhao, D., Richer, E., Antich, P. P. and Mason, R. P. (2008) 'Antivascular effects of combretastatin A4 phosphate in breast cancer xenograft assessed using dynamic bioluminescence imaging and confirmed by MRI', *The FASEB Journal,* 22(7), pp. 2445-2451.

Zhao, H., Doyle, T. C., Coquoz, O., Kalish, F., Rice, B. W. and Contag, C. H. (2005) 'Emission spectra of bioluminescent reporters and interaction with mammalian tissue determine the sensitivity of detection in vivo', *Journal of Biomedical Optics,* 10(4), pp. 9.

Zhou, Y. F. (2011) 'High intensity focused ultrasound in clinical tumor ablation', *World J Clin Oncol,* 2(1), pp. 8-27.